nature cancer

Article

https://doi.org/10.1038/s43018-025-00994-3

Innate immunity and the NF-κB pathway control prostate stem cell plasticity, reprogramming and tumor initiation

Received: 16 April 2025

Accepted: 5 May 2025

Check for updates

Chen Jiang[1,6], Yura Song[1,6], Sandrine Rorive[2], Justine Allard[3], Elisavet Tika[1], Zahra Zahedi[1], Christine Dubois[1], Isabelle Salmon[2], Alejandro Sifrim[4,7] & Cédric Blanpain[1,5,7]

Prostate epithelium develops from multipotent stem cells, which are replaced in adult life by different lineage-restricted basal and luminal unipotent stem cells. Deletion of *Pten* re-induces multipotency in basal cells (BCs); however, the molecular mechanisms regulating BC plasticity and tumor initiation are poorly understood. Here we showed that *Pten* deletion in BCs led to distinct cell fate reprogramming and tumor initiation in a regionalized manner. Single-cell RNA sequencing, ATAC-seq and in situ characterization revealed that following *Pten* deletion in anterior and dorsolateral prostates, BCs were highly plastic and reprogrammed into a hillock-like state, progressing into a proximal-like luminal state before giving rise to invasive tumors. This BC reprogramming was associated with the activation of innate immunity. Pharmacological targeting of interleukin-1, JAK–STAT and NF-κB as well as genetic deletion of *Nfkb* inhibit *Pten*-induced cell plasticity and reprogramming in a cellular autonomous manner, opening new opportunities for prevention and treatment of prostate cancer.

The prostate epithelium is composed of basal cells (BCs), luminal cells (LCs) and rare neuroendocrine cells[1]. It develops from multipotent basal stem cells (SCs), which are largely replaced in adult life by distinct pools of unipotent basal and luminal stem cells[2–6]. Adult unipotent basal SCs can reactivate multipotency in response to prostate inflammation, LC ablation and oncogenic mutations[4–8]. The mouse prostate epithelium is composed by three lobes: the anterior prostate (AP), the dorsolateral prostate (DLP) and the ventral prostate (VP). These different prostate regions expressed different transcriptional program and are maintained by their own pool of progenitors[9–12]. The proximal prostate at the junction with the urethra is sustained by *Trop2/Krt4* expressing LCs whereas the distal prostate is sustained by LC expressing *Nkx3.1* (ref. 9–13).

Prostate cancer is one of the most frequent cancers and the second-highest cause of death in men[14,15]. Most prostate tumors are acinar adenocarcinoma-expressing androgen receptor (AR)[14]. The most frequently mutated genes in prostate cancer consist of different gene fusions activating ETS transcription factors and deletion of the tumor suppressor gene *Pten*[14,15]. *Pten* deletion in mouse prostate leads to similar tumors as found in human and that progress from prostate intraepithelial neoplasia lesions (PINs) into invasive adenocarcinoma[4–6,13–17]. Genetic lineage tracing and transplantation experiments have demonstrated that both BCs and LCs can serve as the cell of origin of prostate cancer[4–6,13,18–21]. Conflicting findings have been reported as to whether BCs or LCs lead to the most aggressive prostate tumors[4–6]; however, how the spatially distinct prostate SC

[1]Laboratory of Stem Cells and Cancer, Université Libre de Bruxelles (ULB), Brussels, Belgium. [2]Centre Universitaire Inter Regional d'Expertise en Anatomie Pathologique Hospitalière, CurePath (CHIREC - CHU TIVOLI -Université Libre de Bruxelles), Charleroi, Belgium. [3]DIAPath, Center for microscopy and molecular Imaging, Université Libre de Bruxelles, Gosselies, Belgium. [4]Department of Human Genetics, University of Leuven, KU Leuven, Leuven, Belgium. [5]WEL Research Institute, Université Libre de Bruxelles (ULB), Brussels, Belgium. [6]These authors contributed equally: Chen Jiang, Yura Song. [7]These authors jointly supervised this work: Alejandro Sifrim, Cédric Blanpain. e-mail: Cedric.Blanpain@ulb.be

states identified by single-cell RNA sequencing (scRNA-seq) contribute to prostate tumor initiation is currently unknown. Transplantation experiments have shown the greater potential of BCs over LCs to serve as the cells of origin of prostate cancer[18–20]. *Pten* deletion in BCs give rise to LCs before progressing into prostate cancer[4–6]. The mechanisms by which *Pten* deletion activates cell plasticity in BCs and consequently lead to tumor initiation is not well understood.

In this study, we combined mouse genetic lineage tracing, single-cell transcriptional, chromatin profiling and functional experiments in mice in vivo and in organoids in vitro to investigate the importance of the cells of origin in controlling tumor heterogeneity and the mechanisms regulating oncogene-induced SC plasticity and transcriptional reprogramming during prostate tumor initiation.

Results

Region-dependent BC plasticity and tumor progression

To define the mechanisms regulating basal to luminal transition upon *Pten* deletion in BCs, we first assessed the temporal kinetics of LC appearance, by monitoring with flow cytometry (FACS), the proportion of yellow fluorescent protein (YFP)$^+$ BCs (CD49f^{High}EpCAM$^+$) and LCs (CD49f^{Low}EpCAM$^+$)[22] following tamoxifen (TAM) administration to K5CreER/Pten$^{fl/fl}$/RosaYFP mice (Fig. 1a) in the different prostate lobes. At 1 week following TAM administration, only BCs were YFP$^+$, demonstrating the specific targeting of BCs by the K5CreER. The first YFP$^+$ LCs appeared between 4–6 weeks and gradually increased over time. This cell fate switch occurred more rapidly in the AP and DLP compared to VP (Fig. 1a–d and Extended Data Fig. 1a–e). Immunofluorescence of prostate with basal (K14) and luminal (K8) markers demonstrated the presence of large patches of YFP$^+$ LCs and the existence of basal/luminal hybrid cells coexpressing basal and luminal markers within the same cells, supporting the notion that basal to luminal transition passes through a hybrid state (Fig. 1e,f). 5-ethynyl-2′-deoxyuridine (EdU) pulse–chase experiments following *Pten* deletion in BCs showed that symmetric BC division (BC–BC EdU doublets) and asymmetric BC division (BC–LC EdU doublets) occurred with the same frequency, suggesting that BCs balance self-renewal and LC differentiation upon *Pten* deletion (Extended Data Fig. 1f,g). Histological characterization of tumor initiation showed that the first signs of high-grade PINs (HGPINs) occurred concomitantly to the hybrid state and basal to luminal transition and the first signs of invasive adenocarcinoma (ADC) transition were visible at 12 weeks following *Pten* deletion in AP and DLP (Fig. 1g,h). In contrast, at the same time point, only atypical intraductal cribriform proliferations of the prostate (AIP) and focal intraductal carcinoma of prostate (IDC-P) with no invasive ADC were observed in the VP, suggesting that tumor progression occurs more slowly in VP compared to DLP and AP upon *Pten* deletion in BC (Fig. 1g,h). At 6 months, invasive ADC showed a more homogeneous pattern in AP and DLP, whereas in VP foci of invasive ADC alternate with HGPIN, AIP and IDC-P lesions (Fig. 1g,h), further showing the delay in tumor progression in BC-derived tumorigenic lesions in the VP compared to the DLP and AP.

RNA-seq of FACS-isolated LCs of different lobes at 6 months following *Pten* deletion in BC showed a strong upregulation of collagen, extracellular matrix (ECM), metalloprotease and innate immunity/inflammatory signaling pathways including many chemokines and cytokines in the AP/DLP compared to the VP in BC-derived LC tumors (Fig. 1i,j). In situ characterization of the tumors showed a major difference in the stromal composition across the different lobes with a much stronger inflammatory/immune and fibroblastic/desmoplastic infiltration as well as collagen (Col1a1) deposition in the AP/DLP compared to the VP (Fig. 1k–n).

Of note, deletion of *Pten* in LC using K8CreER/Pten$^{fl/fl}$/RosaYFP mice did not promote luminal SC plasticity and multipotency (Fig. 2a–d and Extended Data Fig. 1h,i). In AP and DLP, tumor progression was slower in LCs derived tumors compared to BC-derived tumors as shown by the absence of high-grade lesions in K8CreER/Pten mice at 6–8 weeks and the paucity of florid IDC-P at 12 weeks. In contrast, tumors progressed faster following *Pten* deletion in LCs compared to BCs in the VP (Fig. 2e,f).

To understand the reasons for the difference in tumor progression in BC- and LC-derived tumors in AP/DLP, we performed RNA-seq of FACS-isolated LCs at 6 months following *Pten* deletion in BCs or in LCs (Fig. 2g). Of note, we observed a strong decrease in collagen, ECM, cell cycle and innate immunity/inflammatory signaling pathways in AP/DLP tumors originating from LCs as compared to BCs (Fig. 2h,i). The difference in gene expression between BC- and LC-derived tumors in AP/DLP was associated with a decrease in stromal infiltration, collagen deposition and Ly6G$^+$ myeloid cell recruitment with decrease in tumor cell proliferation (Fig. 2j–o).

Altogether these data indicate that the cells of origin of prostate tumors control SC plasticity and tumor progression upon *Pten* deletion.

Combined oncogenic hits increase BC plasticity

Activating mutations in *PIK3CA* have been found in human prostate cancers and *Pten* deletion together with oncogenic *Pik3ca* expression accelerate prostate cancer formation in mice[23]. To assess whether increasing the strength of PI3K signaling accelerates basal to luminal transition, we generated a double-mutant mouse expressing Pik3ca^{H1047R} together with *Pten* deletion (K5CreER/Pten$^{fl/fl}$/Pik3ca^{H1047R}/RosaYFP) (Fig. 3a). We found that basal to luminal transition was dramatically accelerated in these double-mutant mice (Fig. 3b–d). Immunostaining analysis revealed the presence of large patches of YFP$^+$ LCs and hybrid BC/LCs at 3 weeks following TAM administration in AP and DLP (Fig. 3e,f). This major acceleration in basal to luminal transition was accompanied by a dramatic acceleration of tumorigenesis in DLP and AP (Fig. 3g,h).

Deletion of *Trp53* and *Pten* is found in human prostate cancers and accelerate prostate tumorigenesis in mice[24,25]. The co-deletion of *Trp53* and *Pten* in BC and LC using Probasin-Cre led to the occurrence of

Fig. 1 | *Pten* deletion induced BC plasticity and tumor initiation in a cell of origin and region-specific manners. a, Genetic strategy to lineage trace BC following *Pten* deletion. **b**,**c**, Representative FACS plot of CD49f and EpCAM expression in YFP$^+$ prostate epithelial cells from K5CreER/Pten$^{fl/fl}$/RosaYFP mice (K5-PTEN) (**b**) and quantification of the % of YFP$^+$ LCs in total YFP$^+$ cells (**c**) at indicated time after TAM administration. $n = 3$ mice (1w, 4w, 7w, 8w and 20w), $n = 4$ mice (6w and 12w). **d**, Quantification of the % of YFP$^+$ BCs and LCs in total BCs and LCs in K5-PTEN mice. $n = 6$ mice (1w), $n = 9$ mice (6–8w). **e**,**f**, Representative images of immunostaining (**e**) and quantification of the % of YFP$^+$K14$^+$ in total K14 cells, hybrid cells in total YFP$^+$ cells, YFP$^+$K8$^+$ in total K8$^+$ cells (**f**) using indicated antibodies. Arrows indicate hybrid cells (YFP$^+$K14$^+$K8$^+$). Scale bar, 50 µm (up), 10 µm (down). $n = 3$ mice. **g**,**h**, H&E-stained histological sections (**g**) and quantification of different types of tumorigenic lesions (**h**) along prostate tumor progression in K5CreER/RosaYFP (CTL) and K5-PTEN mice at 8 weeks and at indicated time after TAM administration, respectively. Scale bar, 50 µm. Arrows indicate HGPIN, and arrowheads indicate invasive ADC. Number of mice (n) is indicated. **i**, GO analysis of genes upregulated by more than twofold in FACS-isolated YFP$^+$ LCs arising from *Pten*-deleted BCs from AP/DLP compared to VP in K5-PTEN mice 6 months following TAM administration. **j**, Relative mRNA expression from bulk RNA-seq of FACS-isolated LCs from AP/DLP versus VP ($n = 3$ for AP/DLP, $n = 2$ for VP). **k**,**l**, H&E-stained (up) and Col1a1 immunostaining (down, red) (**k**) and quantification stromal histological appearance (**l**). S, stroma region. Scale bar, 50 µm. Number of mice (n) is indicated. **m**,**n**, Representative images of immunostaining of the prostate stroma using anti-green fluorescent protein (GFP) (green), anti-CD45 (red) (**m**) and quantification of CD45-positive cells (**n**) in a 0.1-mm^2 prostate section area. Scale bar, 20 µm. $n = 5$ mice. Graphs are mean ± s.e.m. P values are derived from two-tailed modified Fisher's exact test with Benjamini–Hochberg correction (**i**), two-way (**d**) and one-way (**n**) ANOVA with Tukey's test.

https://doi.org/10.1038/s43018-025-00994-3

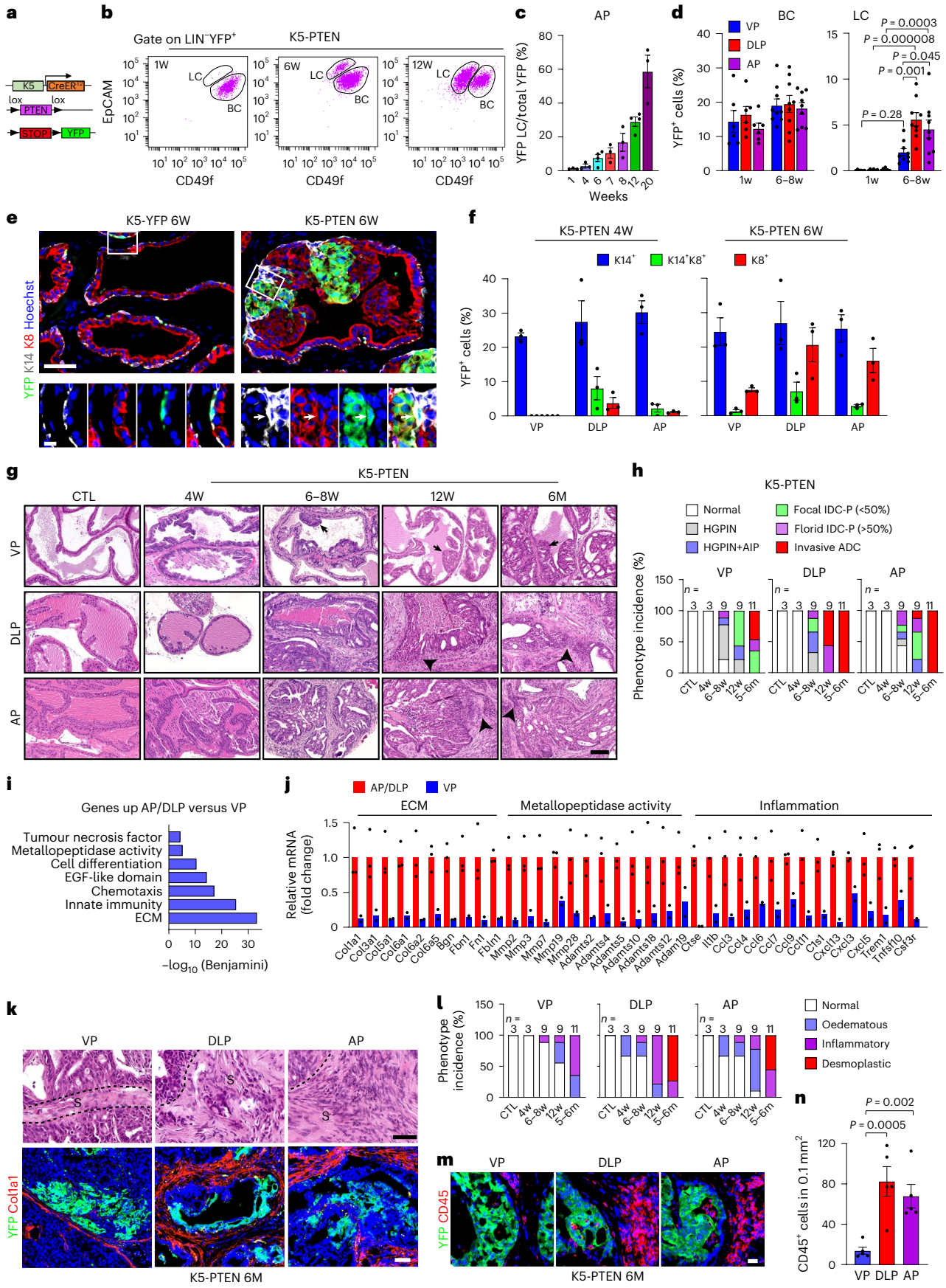

https://doi.org/10.1038/s43018-025-00994-3

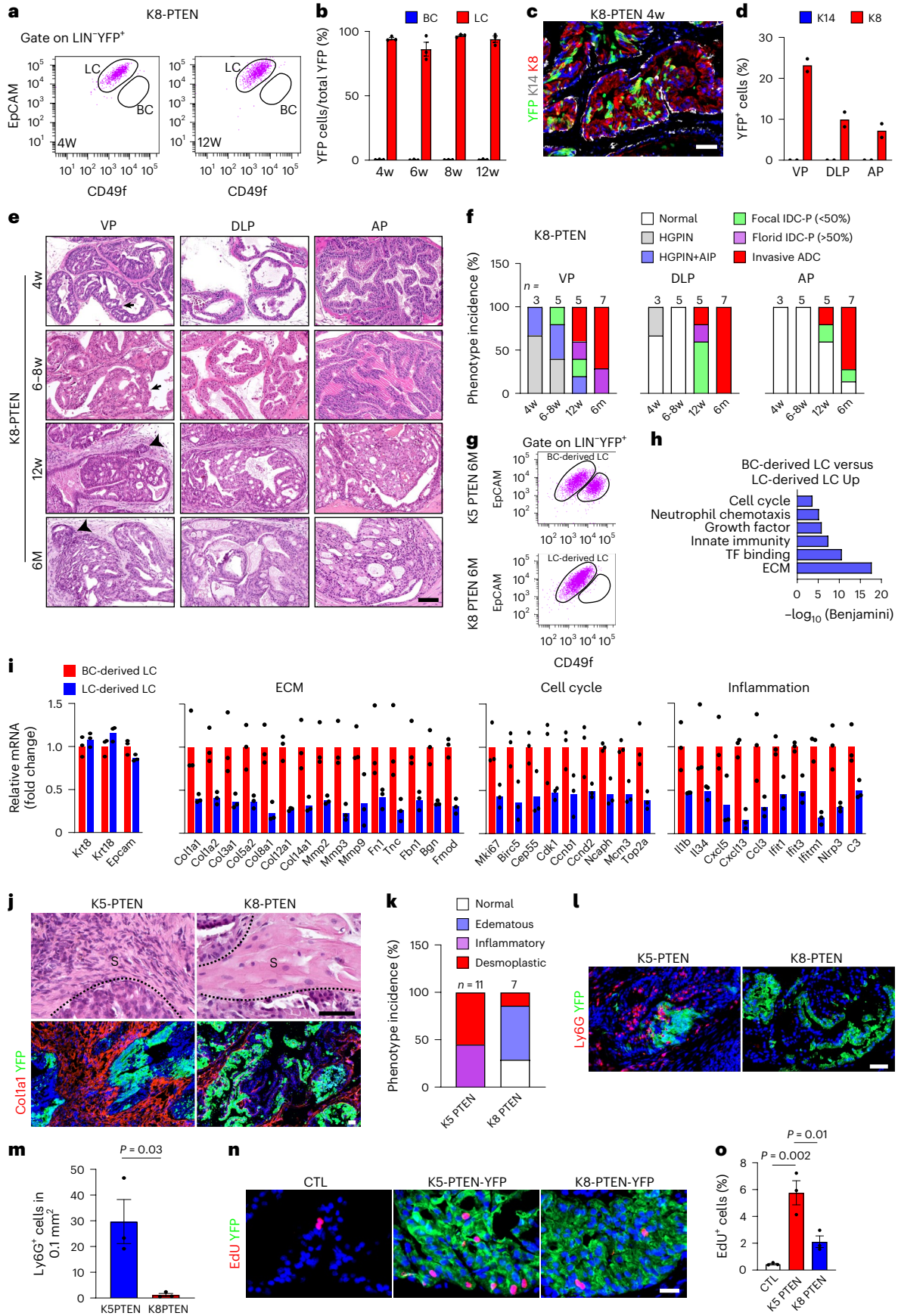

https://doi.org/10.1038/s43018-025-00994-3

Fig. 2 | *Pten* deletion in LCs does not promote multipotency and is associated with slower tumor progression in AP/DLP compared to BC-derived tumors. **a**,**b**, Representative FACS plot of CD49f and EpCAM expression in YFP$^+$ prostate epithelial cells from K8-PTEN mice (**a**) and quantification of the % of YFP$^+$ BCs and LCs in total YFP$^+$ cells (**b**) at indicated times after TAM administration. $n = 3$ mice. **c**,**d**, Representative prostate immunostaining (**c**) and quantification of the % of YFP$^+$K14$^+$ in total K14 cells, and YFP$^+$K8$^+$ in total K8$^+$ cells (**d**) from K8-PTEN mice 4 weeks after TAM administration using the indicated antibodies. Scale bar, 50 µm. $n = 2$ mice. **e**,**f**, H&E-stained histological sections (**e**) and quantification of different types of tumorigenic lesions along prostate tumor progression (**f**). Scale bar, 50 µm. Arrows indicate HGPIN, and arrowheads indicate invasive ADC. Number of mice (n) is indicated. **g**, FACS-isolated of YFP$^+$ LC tumors in AP/DLP from BC- and LC-derived tumors 6 months after TAM administration. **h**, GO term of genes upregulated more than twofold in FACS-isolated YFP$^+$ LCs arising from BC versus LC derived tumors in AP/DLP. **i**, Relative mRNA expression from bulk RNA-seq of FACS-isolated YFP$^+$ LCs arising from BC versus LC derived tumors in AP/DLP. $n = 3$ mice. **j**,**k**, H&E-stained (up) and Col1a1 immunostaining (down, red) (**j**) and quantification of stromal histological appearance from BC- and LC-derived AP tumors (**k**) 6 months after TAM administration. Scale bar, 50 µm. S, stroma region. Number of mice (n) is indicated. **l**,**m**, Representative immunostaining of the myeloid infiltration (**l**) and quantification of Ly6G-positive cells (**m**) from BC- and LC-derived AP tumors 6 months after TAM administration using anti-GFP and anti-Ly6G antibodies. Scale bar, 50 µm. $n = 3$ mice. **n**,**o**, Immunostaining of EdU and GFP (**n**) and quantification of EdU-positive cells (**o**) in YFP$^+$ cells from control, BC- and LC-derived AP/DLP tumors 3 months after TAM administration 24 h following EdU injection. Scale bar, 20 µm. $n = 3$ mice. Graphs show mean ± s.e.m. P values are derived from two-tailed modified Fisher's exact test with Benjamini–Hochberg correction (**h**), two-sided unpaired t-test (**m**) and one-way ANOVA with Tukey's test (**o**).

hybrid BCs and LCs found mainly in early PIN lesions and progression of tumors with epithelial–mesenchymal transition features[26]. *Trp53* deletion together with *Pten* deletion greatly accelerated BC plasticity and the differentiation of BC into LCs in the DLP and AP and not in the VP (Fig. 3i–l). Immunostaining analysis showed the presence of large patches of YFP+ LCs and hybrid BC/LCs at 4 weeks following TAM administration in AP and DLP (Fig. 3m,n).

These two mouse models exhibited severe hyperplastic growth in the facial skin and eyelids, leading to poor general health that required termination of the experiments 6 weeks after TAM administration, preventing studying the long-term consequence of these double-mutant mice.

To exclude that the phenotypes observed using K5CreER was not due to a noncellular mechanism related to the expression of the K5CreER in other epithelia such as the skin and the esophagus, we performed co-deletion of *Pten/Pik3ca* and *Pten/Trp53* using intraprostatic injection of adenovirus expressing Cre under the K5 promoter (AdeK5Cre) in Pten$^{fl/fl}$/Pik3ca^{H1047R}/RosaYFP and Pten$^{fl/fl}$/P53$^{fl/fl}$/RosaYFP mice. Immunostaining revealed that 1 week after intraprostatic injection of AdeK5Cre only BCs were YFP labeled, showing the specificity of the initial BC targeting by the adenovirus-Cre (Fig. 3o,p). Two months following oncogenic recombination in BCs, BCs massively differentiated into LCs with the presence of basal/luminal hybrid cells in both mouse models (Fig. 3q–t), demonstrating that prostate SC plasticity is not mediated by inflammation induced in other organs targeted by the K5CreER.

Altogether, these results demonstrate that BC plasticity and the generation of hybrid cells following oncogenic hits in prostate BCs is associated with tumorigenesis in a region-specific and oncogenic dosage-dependent manner.

mTOR inhibition blocks BC plasticity and tumor initiation

Pten deletion and oncogenic *Pik3ca* have been shown to activate Akt, which in turn activates mTOR signaling[27]. Inhibition of Akt and mTOR signaling has been used in combination with anti-androgen therapy to treat castration-resistant prostate cancer in preclinical models[27–29]; however, the role of mTOR signaling in the regulation of cell plasticity and the activation of BC multipotency and prostate tumor initiation is currently unknown. To assess whether mTOR signaling can regulate BC multipotency and the early step of prostate tumor initiation, we treated K5CreER/Pten$^{fl/fl}$/RosaYFP mice with rapamycin, the first developed mTOR inhibitor[30], after oncogenic recombination and assessed basal to luminal transition 6 weeks after TAM administration. Rapamycin administration dramatically decreased the proportion of YFP$^+$ LCs arising from the differentiation of BCs following *Pten* deletion (Extended Data Fig. 2a–c). Rapamycin treatment also strongly inhibited BC multipotency, basal–luminal hybrid state and the differentiation of BCs into LCs following combined *Pten* deletion and *Pik3ca* activation (Extended Data Fig. 2d–f).

Notably, the strong inhibition of BC multipotency following *Pten* deletion was accompanied by a major reduction in tumorigenesis (Extended Data Fig. 2g,h). Altogether, these results show that mTOR signaling is critical for the activation of BC multipotency following oncogenic hits and inhibition of mTOR signaling by rapamycin blocks the early step of prostate tumor initiation.

Regionalization of BC reprogramming upon Pten deletion

To decipher the molecular mechanisms associated with the basal to luminal transition that accompanies prostate tumorigenesis, we performed scRNA-seq of FACS-isolated epithelial cells 6 weeks following *Pten* deletion in K5CreER/Pten$^{fl/fl}$/RosaYFP. Unsupervised clustering of wild-type (WT) prostate epithelial cells showed the presence of well separated BC and LC clusters (Fig. 4a), corresponding to the different prostate lobes (dorsal, lateral and ventral) and different regions within the prostate (proximal and distal), the anterior and dorsal distal lobes give rise to one cluster called anterodorsal (AD), whereas the proximal, lateral and ventral lobes give rise to three additional clusters as previously reported (Extended Data Fig. 3a–g)[9–11]. In contrast, upon *Pten* deletion, we found a continuum of cells between the BC

Fig. 3 | *Pten* Deletion together with oncogenic *Pik3ca* expression or *p53* deletion accelerate BC plasticity. **a**, Genetic strategy to lineage trace BC with *Pten* deletion and oncogenic *Pik3ca* expression. **b**–**d**, Representative FACS plot of CD49f and EpCAM expression in YFP$^+$ prostate epithelial cells (**b**) and quantification of the % of YFP$^+$ BCs (**c**) in total BCs and YFP$^+$ LCs (**d**) in total LCs in K5-PTEN ($n = 3$) and K5-PTEN-PIK mice ($n = 5$) 3 weeks after TAM administration. **e**,**f**, Representative prostate immunostainings of K5-PTEN-PIK 3W mice (**e**) and quantification of the % of hybrid cells in total YFP$^+$ cells, YFP$^+$K8$^+$ in total K8$^+$ cells (**f**) using indicated antibodies. Arrows indicate hybrid cells (YFP$^+$K14$^+$K8$^+$). Scale bar, 50 µm (up), 20 µm (down). $n = 3$ mice. **g**,**h**, H&E-stained histological sections (**g**) and quantification of different types of tumorigenic lesions (**h**) along prostate tumor progression. Scale bar, 50 µm. $n = 5$ mice. **i**, Genetic strategy to lineage trace BC with *Pten* and *p53* deletion. **j**–**l**, Representative FACS plot of CD49f and EpCAM expression in YFP$^+$ prostate epithelial cells (**j**) and quantification of the % of YFP$^+$ BCs in total BCs (**k**) and YFP$^+$ LCs (**l**) in total LCs in K5-PTEN ($n = 3$) and K5-PTEN-P53 mice ($n = 5$) 4 weeks after TAM administration. **m**,**n**, Representative prostate immunostainings of K5-PTEN-P53 4w mice (**m**) and quantification of the % of hybrid cells in total YFP$^+$ cells and YFP$^+$K8$^+$ cells in total K8$^+$ cells (**n**) using indicated antibodies. Arrows indicate hybrid cells. Scale bar, 20 µm. $n = 3$ mice. **o**,**p**, Representative immunostaining 1 week after AdeK5Cre injection in AP (**o**) and quantification of YFP$^+$K14$^+$ and YFP$^+$K8$^+$ (**p**) in total YFP$^+$ cells using anti-GFP, anti-K8 and anti-K14 antibodies. Scale bar, 20 µm. $n = 3$ mice. **q**–**t**, Representative immunostaining of Pten$^{fl/fl}$/Pik3ca^{H1047R}/RosaYFP (**q**) and Pten$^{fl/fl}$/P53$^{fl/fl}$/RosaYFP mice (**s**) 2 months after AdeK5Cre injection. Scale bar, 50 µm. Quantification of the % of hybrid and YFP$^+$K8$^+$ cells in total YFP$^+$ cells in Pten/Pik ($n = 3$) (**r**) and Pten/P53 mice (**t**) ($n = 2$). Graphs show mean ± s.e.m. P values are derived from two-way (**d**,**l**) and one-way (**f**,**n**) ANOVA with Tukey's test.

https://doi.org/10.1038/s43018-025-00994-3

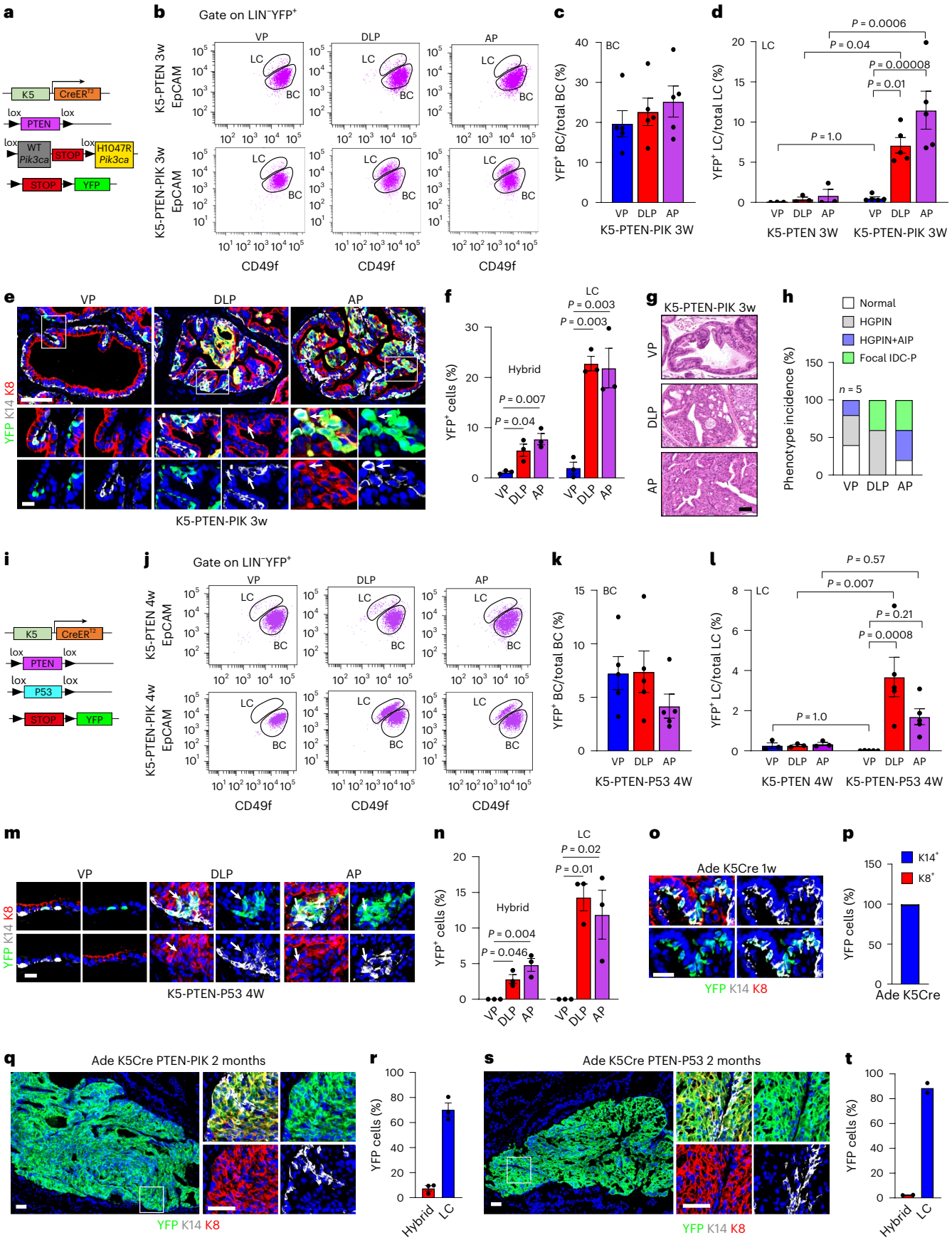

https://doi.org/10.1038/s43018-025-00994-3

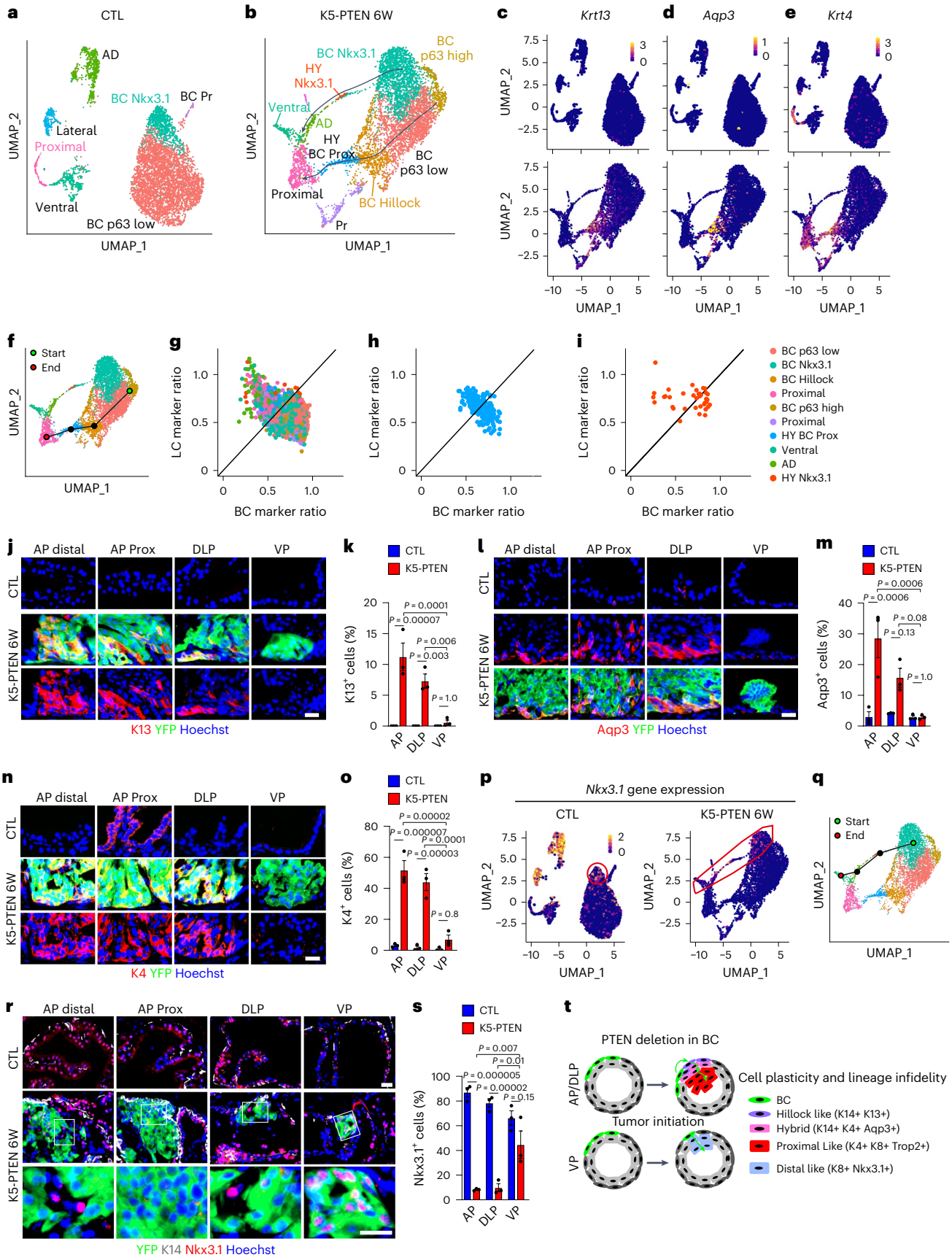

https://doi.org/10.1038/s43018-025-00994-3

Fig. 4 | Region-dependent BC reprograming following *Pten* deletion. **a**,**b**, UMAP dimensionality reduction of scRNA-seq data shows unsupervised clustering of FACS-isolated prostate epithelial cells from WT (CTL) (**a**) and YFP$^+$ (**b**) epithelial cells from K5-PTEN 6w mice. Black arrows indicate two possible trajectories of basal-to-luminal cell reprogramming. **c**–**e**, Expression of *Krt13* (**c**), *Aqp3* (**d**) and *Krt4* (**e**) in CTL and K5-PTEN 6w. Color bar indicates gene expression level. **f**, Slingshot pseudotime trajectory analysis illustrating the lineage trajectory from BCs to proximal-like LCs. **g**–**i**, Quantitative assessment of LC and BC marker gene expression for all clusters (**g**), hybrid BC proximal-like (HY BC Prox) (**h**) and HY Nkx3.1 (**i**) in K5-PTEN 6w. Scatter-plot with the *x* axis representing the adjusted proportion of BC-specific marker genes and the *y* axis representing the adjusted proportion of LC-specific markers. **j**–**o**, Representative immunostaining of the VP, DLP, AP proximal (AP prox) and AP distal of CTL and K5-PTEN 6w using anti-GFP, anti-K13 (**j**), anti-Aqp3 (**l**) and anti-K4 (**n**) antibodies. Scale bar, 50 µm. Quantification of the % of K13$^+$ cells (**k**), Aqp3$^+$ cells (**m**) and K4$^+$ cells (**o**) in total YFP$^+$ cells in CTL and K5-PTEN 6w mice. $n = 3$ mice. **p**, UMAP plots colored by normalized gene expression values for Nkx3.1 gene expression in CTL and K5-PTEN 6w. Red outlines show BC expressing Nkx3.1 in CTL, whereas it highlights BCs expressing Nkx3.1 that pass through a hybrid cluster and end in ventral LCs in K5-PTEN 6w. **q**, Slingshot pseudotime trajectory analysis for the trajectory from BCs to ventral LCs. **r**, Representative immunostaining of GFP, Nkx3.1 and K14 in VP, DLP, AP prox and AP distal of CTL and K5-PTEN prostate 6w after Pten deletion. Scale bar, 20 µm. **s**, Quantification of the % of Nkx3.1$^+$ cells in total YFP$^+$ cells in CTL and K5-PTEN 6w mice. $n = 3$ mice. **t**, Cell plasticity, lineage infidelity and tumor progression following *Pten* deletion in BC occurs in a region-specific manner during the early stage of prostate cancer initiation. Graphs show mean ± s.e.m. *P* values are derived from a two-way ANOVA with Tukey's test.

clusters and LC clusters with a major expansion of the proliferative BC cluster and the proximal prostate cluster (Fig. 4b and Extended Data Fig. 3h–o). Lineage trajectory analysis using Slingshot revealed that upon *Pten* deletion, there was a stepwise reprogramming of BCs into hillock-like cells characterized by the expression of *Krt13*, previously described in the human healthy prostate and in human prostate cancers[9,31–34], then hybrid BCs and proximal LCs (*Ly6d* and *Krt6a*) that finally gave rise to proximal LCs (*Krt4*, *Psca*, *Clu*, *Wfdc2*, *Pigr* and *Ltf*) (Fig. 4c–f and Extended Data Fig. 3h–k). Analysis of the proportion of expressed basal and luminal marker genes during the lineage trajectory showed a progressive decrease of BC genes and a progressive increase of LC genes along the differentiation pathway (Extended Data Fig. 4a–d). By analyzing the proportion of BC and LC marker expression across the different cluster cell populations[8,35], we found that the hybrid cell cluster coexpressed a high proportion of basal and luminal genes within the same cells, confirming their hybrid state (Fig. 4g–i). To visualize the spatial localization of the hillock, hybrid and proximal-like LC that appears following *Pten* deletion, *Pten/p53* deletion and Pten/Pik3ca^{H1047R}, we performed co-immunofluorescence using representative markers of these three states: hillock (Krt14, Krt13 and Aqp3), hybrid (Krt14, Krt4 and Aqp3) and LC proximal state (Krt8, Krt4 and Trop2) (Extended Data Fig. 4e–h). Of note, this first cellular reprogramming into hillock and proximal-like states first occurred in the AP and DLP and not in the VP and the spatial localization of the different cell states identified by in situ characterization was consistent with the pseudotime ordering predicted by the computational lineage trajectory analysis (Fig. 4j–o).

We found a second continuum of cells spanning from BCs expressing high levels of *Nkx3.1* toward ventral LCs expressing *Spink1*, *Sbp* or *Sbpl* passing through a hybrid state, coexpressing both basal and luminal markers (Fig. 4i,p and Extended Data Fig. 3m). Slingshot lineage trajectory inferred a second differentiation trajectory from BC expressing *Nkx3.1* toward VP LCs (Fig. 4q and Extended Data Fig. 5a–d). In situ characterization of this second lineage trajectory showed that this cellular reprogramming and differentiation into Nkx3.1 LCs occurred in the VP (Fig. 4r,s). As these lesions progressed into adenocarcinoma, Nkx3.1 was progressively lost (Extended Data Fig. 5e). Like the cancers arising from VP BCs, LCs did not give rise to hillock-like cells and less Krt4 expressing proximal states following *Pten* deletion in LCs (Extended Data Fig. 5f).

To gain further insights into the molecular mechanisms that promote BC reprogramming into the hillock-like/hybrid/proximal-like LC differentiation path or BC Nkx3.1 toward the ventral LC differentiation path, we performed differential gene expression analysis between the hybrid cells and the BCs or their respective LC population. Compared to BCs, the hybrid basal/luminal proximal population expressed higher levels of *Krt4*, *Psca*, *Wfdc2* or *Clu* (Extended Data Fig. 5g), in concordance with the high expression of these genes within the proximal prostate cluster[9–11,16]. When compared to the proximal LCs, this hybrid cluster presented an increased expression of many genes of the BC identity such as *Krt5*, *Krt14*, *Krt15*, *Krt17* or *Col17a1* (Extended Data Fig. 5h). The overlapping upregulated genes, including *Aqp3*, *Ly6d* and *Krt6a*, exhibit a distinct hybrid gene signature (Extended Data Figs. 3k and 5g,h). In the other trajectory, when comparing the gene expression of the hybrid Nkx3.1 with BCs, we found a higher level of expression of *C1rb*, *Nkx3.1*, *Fgl1* and *Tgm4* (Extended Data Fig. 5i). Conversely, when compared to ventral LCs, this second hybrid population expressed higher level of basal genes such as *Krt14* or *Krt5* (Extended Data Fig. 5j). Altogether, these data show that the two different BC populations targeted by *Pten* deletion will undergo distinct reprogramming, giving rise to two distinct lineage differentiation trajectories toward different LC lineages in a region-specific manner (Fig. 4t).

BC plasticity is associated with innate immunity activation

To gain further insights into the gene regulatory networks controlling the two differentiation paths, we performed regulatory network analysis using SCENIC[36], which infers the transcription factors (TFs) and their downstream target genes (regulons) that are active in the

Fig. 5 | BC plasticity following *Pten* deletion is associated with the activation of interferon and TNF pathways in epithelial cells. **a**, Regulatory network analysis using SCENIC. UMAP plots representing regulon activity (top) and corresponding transcription factor expression (bottom) in K5-PTEN 6w mice. Color scales represent SCENIC AUC scores for regulon activity and normalized gene expression levels of each transcription factor. Exp, expression. **b**, GO analysis of genes upregulated more than twofold on bulk RNA-seq of FACS-isolated YFP$^+$ BCs from K5-PTEN mice 5 weeks after TAM administration compared (BC PTEN) to WT BCs (BC CTL). **c**, GO analysis of genes upregulated more than twofold in FACS-isolated YFP$^+$ LCs arising from *Pten*-deleted BCs from K5-PTEN mice 5 weeks after TAM injection (LC PTEN) compared to WT LCs (LC CTL). **d**,**e**, Relative mRNA expression (bulk RNA-seq) of BC CTL, LC CTL, BC PTEN and LC PTEN (data for genes regulating inflammation, and reprogramming and cell proliferation are shown in **d** and **e**, respectively) ($n = 2$ samples). **f**, Representative examples of ATAC-seq peaks of inflammatory-related genes from FACS-isolated BC CTL, LC CTL and BC PTEN from K5-PTEN mice 6 weeks after TAM administration. The 100,000 cells pooled from at least three mice. Scale for visualization, *Il1r1* (0–21), *Cd52* (0–13), *Cd55* (0–24), *Cd83* (0–13), *Ifit1* (0–13) and *Cxcl5* (0–18). **g**, TF motif enrichment analysis of peaks upregulated in BC PTEN compared to BC CTL. *P* values were calculated using a binomial test. **h**, Western blot of FACS-isolated LIN$^-$ epithelial cells from CD1 mice (CTL epi) and Lin$^-$YFP$^+$ epithelial cells of K5-PTEN mice 6 weeks after TAM injection (PTEN YFP$^+$) using the indicated antibodies. $n = 3$ mice. **i**,**j**, Representative immunostaining of myeloid cells in the prostate (**i**) and quantification of Ly6G-positive cells (**j**) from K5CreER/RosaYFP ($n = 3$ mice) and K5CreER/Pten$^{fl/fl}$/RosaYFP mice ($n = 4$ mice) 6 weeks after TAM administration using anti-GFP and anti-Ly6G antibodies. Scale bar, 20 µm. Graphs are mean ± s.e.m. *P* values are derived from two-sided unpaired *t*-test. *P* values were derived from two-tailed modified Fisher's exact test with Benjamini–Hochberg correction (**b**,**c**).

https://doi.org/10.1038/s43018-025-00994-3

different cell clusters corresponding to the different differentiation paths. In the first differentiation path, we found that many TFs relaying inflammation and innate immunity pathways such as *Irf6*, *Irf7*, *Stat1*, *Stat2*, *Nfkb2* or *Relb* were active in the hillock and hybrid cells (Fig. 5a). In addition, we found that lineage determinant TFs such as *Elf3*, *Creb5* or *Grhl3* were more active in these two cell lineages as well as in the proximal LCs (Extended Data Fig. 5k–m).

To investigate further the molecular mechanisms that lead to the cell fate changes upon *Pten* deletion in BCs, we performed bulk RNA-seq of FACS-isolated BCs and LCs in WT mice and 5 weeks following

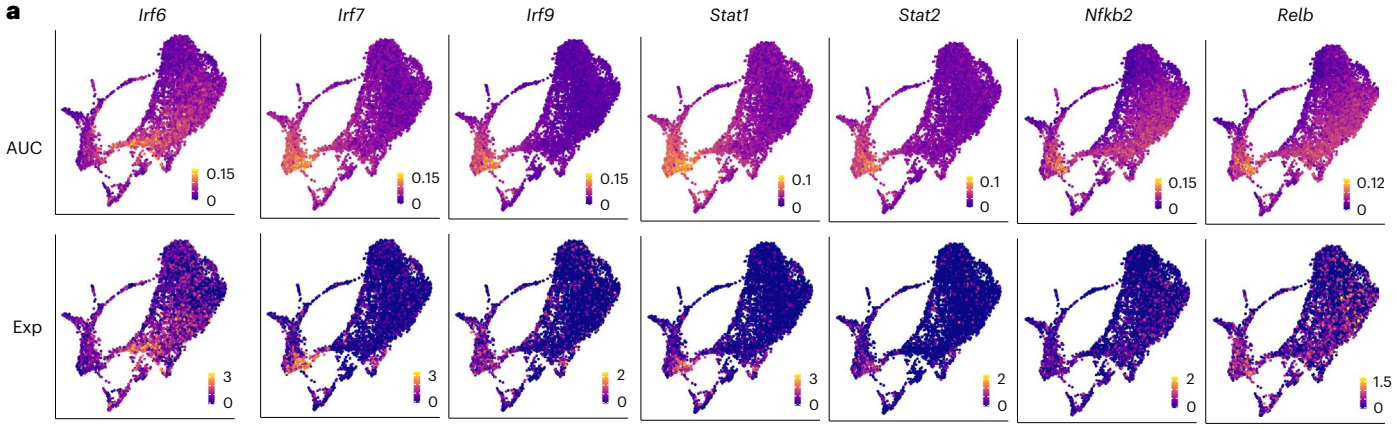

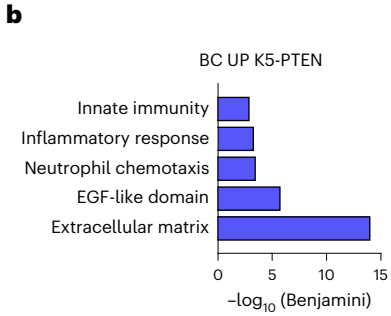

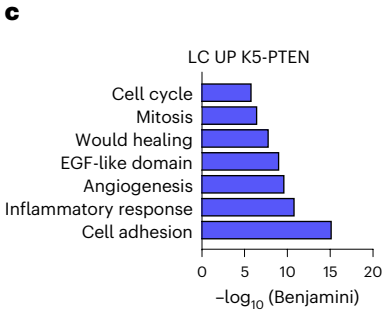

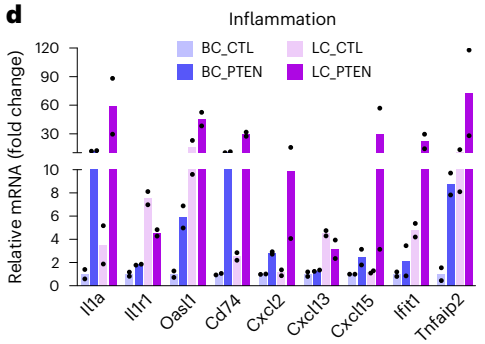

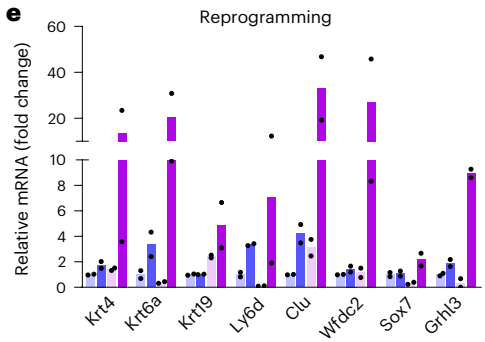

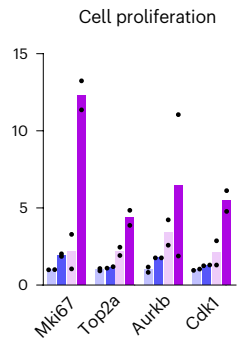

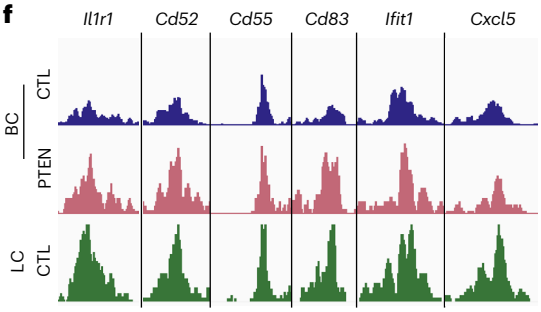

g

Motif	Name	Pval	%Target	%Back
	Fos	1.0×10^{-134}	52.38	26.18
	Junb	1.0×10^{-129}	50.25	24.77
	AP-1	1.0×10^{-129}	56.13	29.78
	p63	1.0×10^{-14}	26.04	18.78
	NF-κB-p65	1.0×10^{-4}	16.46	13.5

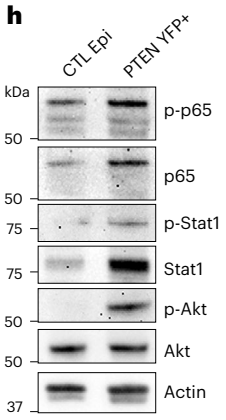

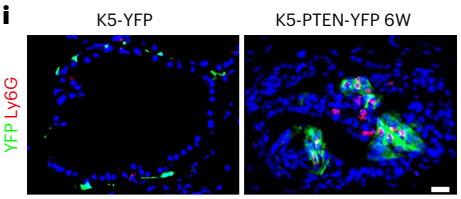

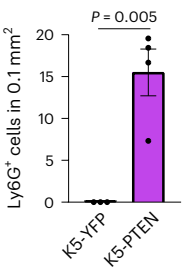

https://doi.org/10.1038/s43018-025-00994-3

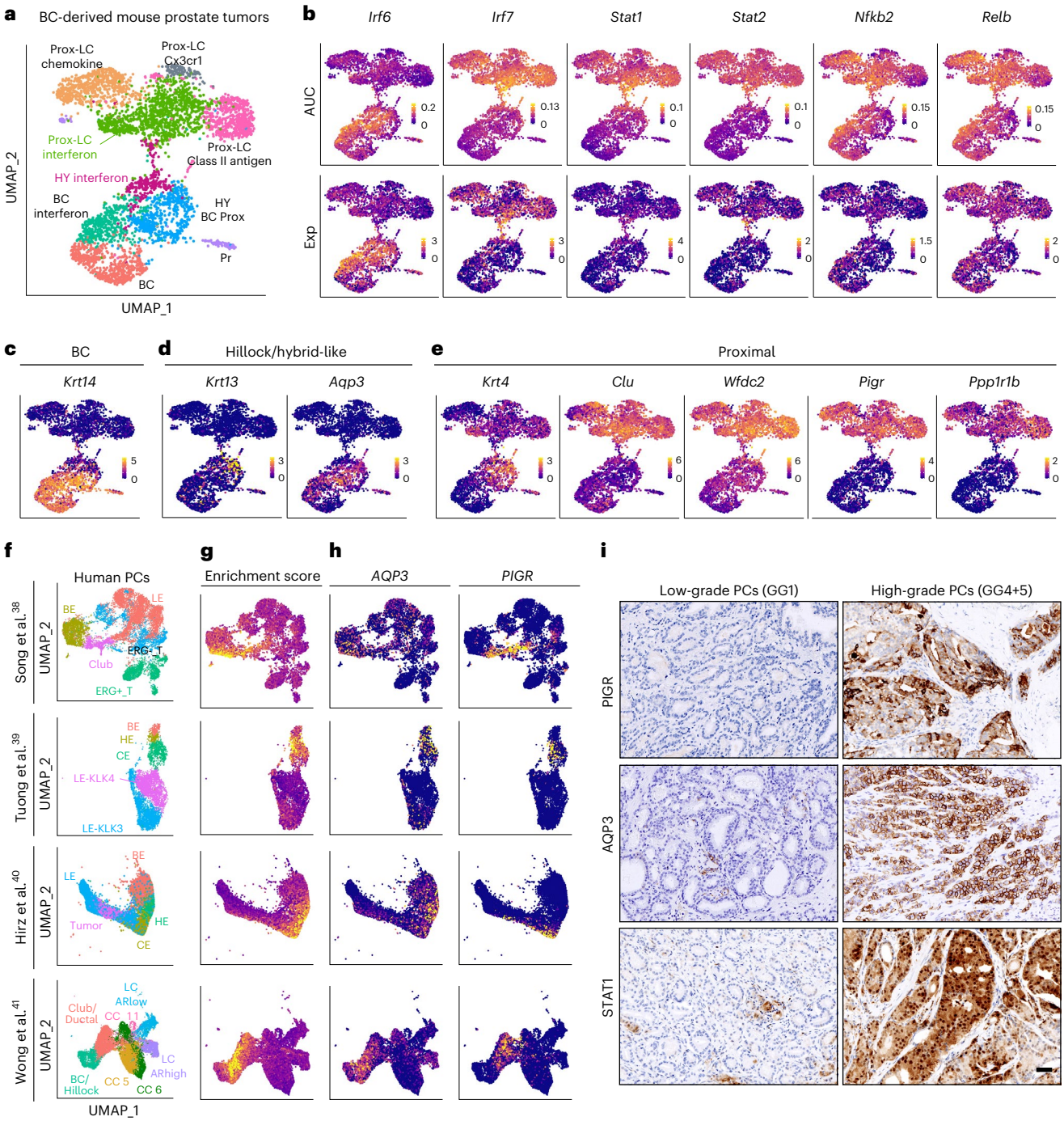

https://doi.org/10.1038/s43018-025-00994-3

Fig. 6 | Regional reprogramming and activation of innate immunity persist in mouse prostate tumors and human prostate cancers. a, Cell populations identified by scRNA-seq of FACS-isolated LIN$^-$YFP$^+$ epithelial cells from K5-PTEN mice 10 months after TAM administration: UMAP plots with different colors representing unsupervised clustering. **b**, Regulatory network analysis using SCENIC. UMAP dimensionality reduction plots with color scaling representing the SCENIC AUC values for transcription factor activation (top) and normalized gene expression (bottom). **c**–**e**, UMAP plots colored by normalized gene expression values of canonical cell markers of BC (*Krt14*) (**c**), hillock and hybrid-like (*Krt13* and *Aqp3*) (**d**) and proximal LCs (*Krt4*, *Clu*, *Wfdc2*, *Pigr* and *Ppp1r1b*) (**e**). **f**, Cell populations on ERG-driven human prostate cancer cells[38]: basal epithelial cells (BEs), nonmalignant luminal epithelial cells (LEs), ERG-positive tumor cells (ERG$^+$ T) and ERG-negative tumor cells (ERG$^-$ T); human prostate cancer atlas[39]: BEs, hillock epithelial cells (HEs), club epithelial cells (CEs); KLK3-high LEs (LE-KLK3) and KLK4-high luminal epithelial cells (LE-KLK4); treatment-naive prostate adenocarcinoma[40]: BEs, HEs, CEs and LEs; invasive cribriform carcinoma and intraductal carcinoma data[41]: basal and hillock cells (BC/hillock), club cells and ductal cells (club/ductal), nonmalignant luminal epithelial with low expression of AR (LC_ARlow) and nonmalignant luminal epithelial with high expression of AR (LC_ARhigh). **g**, UMAP dimensionality reduction plots with color scaling representing enrichment score for the reprogramming markers. **h**, UMAP dimensionality reduction plots for *AQP3* and *PIGR* with color scaling representing the level of gene expression. **i**–**l**, IHC of PIGR, AQP3 and STAT1 (**i**) and IHC score of PIGR (**j**), AQP3 (**k**) and STAT1 (**l**) in PC with different GGs. Scale bar, 50 µm. Number of patients (*n*) is indicated. *P* values are derived from two-sided Fisher's exact test. Pos, positive; Neg, negative.

Pten deletion in BC. Bulk RNA-seq is more sensitive than scRNA-seq to detect low-abundant RNA and changes in gene expression. We found that 1,067 genes were upregulated more than twofold between WT and *Pten*-deleted BCs and 2,844 genes were upregulated in LCs following *Pten* deletion. Gene set enrichment analysis revealed the enrichment of genes regulating ECM, EGF-like domain, neutrophil chemotaxis, inflammatory response and innate immunity in BCs, as well as angiogenesis, mitosis and cell cycle in LCs upon *Pten* deletion (Fig. 5b,c). Genes regulating inflammation such as *Il1a*, *Il1r1*, *Oasl1* and *Cd74*, interferon-responsive genes such as *Ifit1* and *Tnfaip2*, chemokines such as *Cxcl2*, *Cxcl13* and *Cxcl15* as well as genes associated with the cell fate change such as *Krt4*, *Krt6a*, *Grhl3*, *Ly6d*, *Wfdc2* and *Clu* were upregulated in BCs and even further in LCs upon *Pten* deletion (Fig. 5d,e). Proliferation genes were moderately upregulated in BCs but more strongly in LCs upon *Pten* deletion (Fig. 5e). To investigate the onset of innate immune gene activation, we FACS-isolated BCs at different time points after *Pten* deletion in BCs and performed quantitative reverse transcription PCR (qRT–PCR) analysis of inflammatory genes. Our results showed that *Il1a* and *Cxcl2* started to be upregulated 4 weeks after *Pten* deletion at the same time that basal–luminal transition began to be observed (Extended Data Fig. 6a).

To unravel the chromatin remodeling and gene regulatory networks associated with oncogenic hit-induced BC multipotency in the prostate, we performed bulk ATAC-seq of FACS-isolated BCs and LCs from WT mice and BCs 6 weeks following *Pten* deletion in BCs. We found that 1,974 peaks were more accessible and 1,942 peaks were less accessible in BCs upon Pten deletion (Fig. 5f). Motif discovery analysis of the peaks upregulated in BCs following *Pten* deletion revealed the increase of AP-1 TF motif, P63 and Nfkb/p65/Rel motif (Fig. 5g), in good accordance with the SCENIC analysis and the activation of Nfkb/innate inflammation transcription program found by bulk and scRNA-seq. The expression and the active phosphorylation of Stat1 and p65 protein were increased after *Pten* deletion in BCs (Fig. 5h).

To assess whether the lack of expression of hillock-like state following *Pten* deletion in BCs from VP is the consequence of a decrease of chromatin accessibility of the regulatory regions of the genes associated with hillock-like state, we performed ATAC-seq on YFP$^+$ FACS-isolated *Pten*-deleted BCs specifically from the VP, DLP and AP lobes. Our data show that BCs from VP presented a decrease in the chromatin accessibility at the enhancers remodeled following *Pten* deletion of hillock associated genes such as *Krt13* and *Aqp3* compared to BCs of AP/DLP (Extended Data Fig. 6b,c), supporting the notion that hillock associated genes are epigenetically primed to get upregulated following *Pten* deletion in AP/DLP compared to VP. Motif discovery of these different upregulated peaks in AP and DLP versus VP showed enrichment in AP-1, KLF and ETS family of TFs (Extended Data Fig. 6d).

It has been shown that ETS transcription factor ERG (ERG) acts as a master regulator of luminal differentiation in *Pten*-deleted tumors[37]. The ETS motif was enriched in ATAC-seq peaks upregulated in BCs following *Pten* deletion in AP/DLP versus VP. ERG messenger RNA expression was upregulated in BCs and even more strongly in LCs arising from BCs from AP/DLP versus VP following *Pten* deletion (Extended Data Fig. 6e,f), supporting the notion that ERG can promote LC fate differentiation from BCs following *Pten* deletion in AP and DLP.

As rapamycin treatment strongly inhibits the activation of BC multipotency and the initiation of prostate tumorigenesis, we performed bulk -RNA-seq in BCs 3 weeks following *Pten* deletion and *Pik3ca* activation. The deletion of *Pten* and expression of oncogenic *Pik3ca* induced the upregulation of 1,594 genes in BCs (Extended Data Fig. 7a). Gene set enrichment analysis of these upregulated genes revealed the strong upregulation of genes regulating DNA replication and cell cycle progression as well as genes involved in innate immunity and inflammation (Extended Data Fig. 7b). Rapamycin administration inhibited the upregulation of about 50% of the genes upregulated by *Pten* deletion and expression of oncogenic *Pik3ca* and prevented the upregulation of many genes regulating cell proliferation, cell reprogramming and innate immunity (Extended Data Fig. 7a–d). The secretion of leukocyte chemoattractant such as *Cxcl2*, *Cxcl13* and *Cxcl15* following *Pten* deletion in BCs was accompanied by the recruitment of neutrophils and

Fig. 7 | Pharmacological inhibition of Nfkb, JAK/STAT and Il1 inhibits SC plasticity induced by *Pten* deletion. a, Experimental design. **b**, Representative FACS plot of CD49f and EpCAM expression in YFP$^+$ prostate epithelial cells from dimethylsulfoxide- (DMSO), JSH-23- and ruxolitinib-treated K5-PTEN 6w and K5-PTEN-PIK 3w mice. **c**, Quantification of % of YFP$^+$ LCs in total YFP$^+$ cells of whole prostate in DMSO-, JSH-23- and ruxolitinib-treated K5-PTEN 6w mice, *n* = 14 mice (DMSO), *n* = 12 mice (JSH-23), *n* = 13 mice (ruxolitinib) and K5-PTEN-PIK 3w mice, *n* = 8 mice (DMSO), *n* = 7 mice (JSH-23), *n* = 7 mice (ruxolitinib). **d**, Representative FACS plot of CD49f and EpCAM expression in YFP$^+$ prostate epithelial cells from saline- (i.p.) and anakinra- (i.p., 10 mg kg^{-1}, three injections per week) treated K5-PTEN 6w mice and K5-PTEN-PIK 3w mice. **e**, Quantification of % of Lin$^-$YFP$^+$ LCs in total YFP$^+$ cells of whole prostate in K5-PTEN 6w, *n* = 5 mice (saline), *n* = 6 mice (anakinra) and K5-PTEN-PIK 3w mice, *n* = 4 mice (saline), *n* = 6 mice (anakinra). **f**, Representative immunostainings of AP of DMSO-, JSH-23- and ruxolitinib-treated K5-PTEN-PIK 3w mice using anti-GFP (green), anti-K8 (red), anti-K13 (red) and anti-K4 (red) antibodies. Scale bar, 50 µm. *n* = 3 mice. **g**,**h**, Quantification of the % of YFP$^+$K8$^+$ in total K8$^+$ cells, YFP$^+$K13$^+$ and YFP$^+$K4$^+$ in total YFP$^+$ cells of DLP/AP in DMSO-, JSH-23- and ruxolitinib-treated K5-PTEN 6w mice (**g**) and K5-PTEN-PIK 3w mice (**h**). *n* = 3 mice. **i**,**j**, Quantification of YFP$^+$K8$^+$ in total K8$^+$ cells, YFP$^+$K13$^+$ and YFP$^+$K4$^+$ in total YFP$^+$ cells of DLP/AP in saline- and anakinra-treated K5-PTEN 6w mice (**i**) andK5-PTEN-PIK 3w mice (**j**). *n* = 3 mice. **k**, Representative immunostainings of myeloid cell infiltration of AP in DMSO-, JSH-23- and ruxolitinib-treated K5-PTEN-PIK 3w mice using anti-GFP (green), anti-Ly6G and anti-K14 antibodies. Scale bar, 50 µm. *n* = 3 mice. **l**,**m**, Quantification of Ly6G-positive cells in the DLP/AP from DMSO-, JSH-23- and ruxolitinib-treated (**l**) and saline- and anakinra-treated (**m**) K5-PTEN-PIK 3w mice. *n* = 3 mice. Graphs show mean ± s.e.m. *P* values are derived from two-sided unpaired *t*-test (**e**,**i**,**j**,**m**) and one-way ANOVA with Dunnett test (**c**,**g**,**h**,**l**). Ruxo, ruxolitinib; Sal, saline; Ana, anakinra.

https://doi.org/10.1038/s43018-025-00994-3

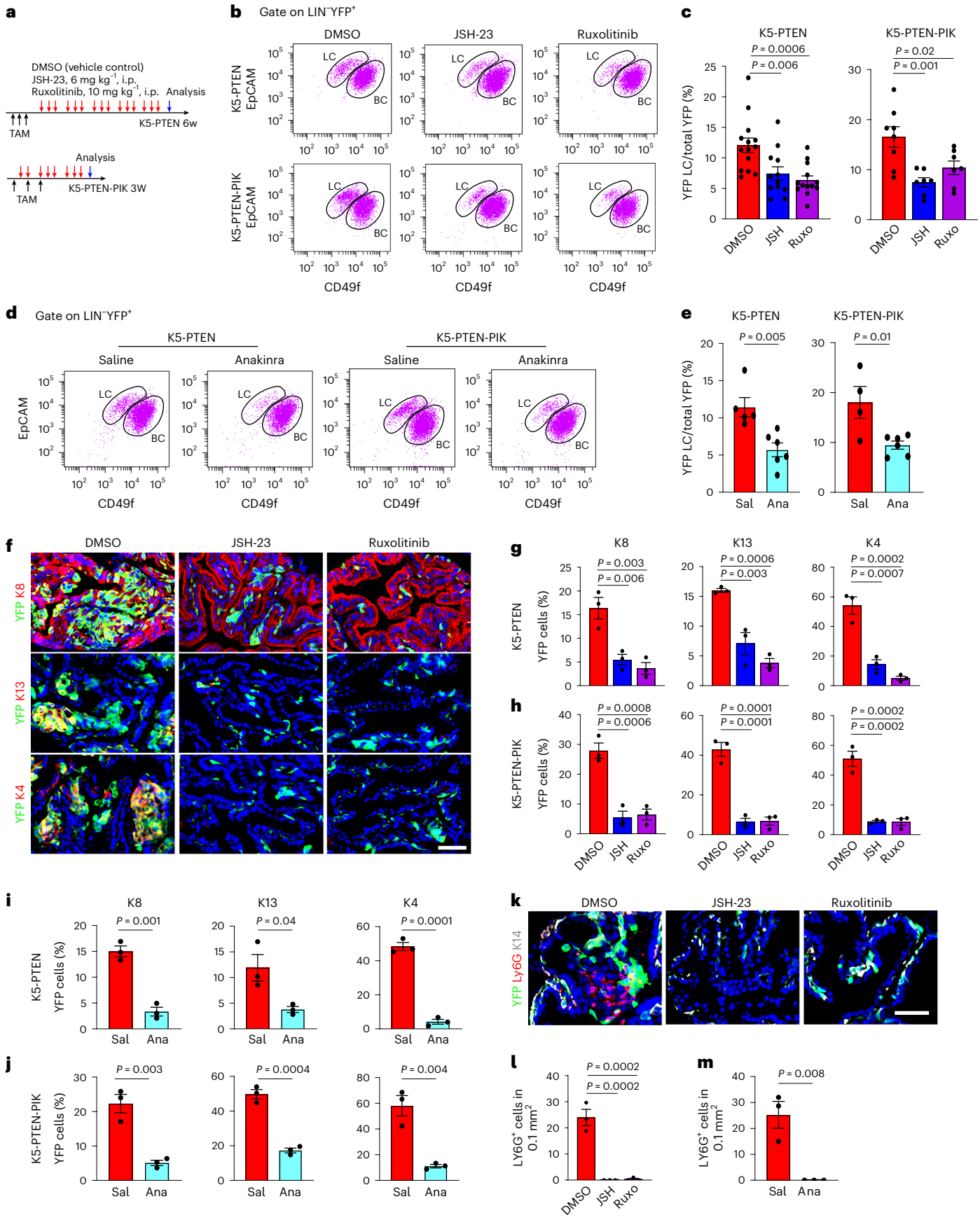

myeloid-derived suppressor cells surrounding the BCs and LCs arising from the multipotent BCs, which was prevented by rapamycin administration (Fig. 5i,j and Extended Data Fig. 7e,f). Altogether, these data show that *Pten* deletion in BCs activates the innate immune pathway in an mTOR dependent manner.

Regional reprogramming in mouse prostate cancers

To assess whether the regional reprogramming and the activation of the innate immunity pathway observed during the early stages of tumor initiation persist in more advanced prostate tumor, we performed scRNA-seq 10 months following *Pten* deletion in BC when almost the whole prostate presents signs of tumorigenesis. Unsupervised clustering analysis revealed the presence of different basal, hybrid and LC clusters (Fig. 6a and Extended Data Fig. 8a–e), reminiscent of the different clusters found 6 weeks following *Pten* deletion. Strong activation of innate immunity was observed in some BC, hybrid and LC clusters with the upregulation of *Irf6*, *Irf7*, *Irf9*, *Stat1* and *Rela* expression and regulon activity (Fig. 6b and Extended Data Fig. 8f–h). Markers of hillock/hybrid-like cells (*Krt13* and *Aqp3*) and proximal LC differentiation such as *Krt4*, *Clu*, *Wfdc2*, *Pigr* and *Ppp1r1b*, were expressed in hybrid and LCs at 10 months following *Pten* deletion (Fig. 6c–e). Immunostaining of Krt13, Aqp3 and Krt4 revealed that these markers were still expressed in more advanced tumors in AP and DLP and much less in VP (Extended Data Fig. 8i–o). Similarly, adenovirus mediated Pten/Pik3ca or Pten/P53 recombination in BCs presented increased expression of Krt13, Aqp3 and Krt4 and myeloid cell infiltration in prostate tumors (Extended Data Fig. 8p–r). Altogether, these data indicate that the region-specific differentiation into hillock and LC proximal-like states as well as the activation of the innate immunity pathway persist at the later stages of mouse prostate tumorigenesis.

Regional reprogramming in human prostate cancers

To investigate whether similar reprogramming also occurs in human prostate cancers, we assessed the expression of markers defining hillock, hybrid and proximal-like states identified from scRNA-seq data from K5-PTEN mice, 6 weeks after TAM administration (K5-PTEN 6w) across four different types of human prostate cancer scRNA-seq data[38–41] (Fig. 6f).

Using these four human prostate cancer single-cell datasets, we quantitatively assessed the enrichment of mouse reprogramming gene signatures in human samples. In the ERG-driven prostate cancer dataset[38], we observed a progressive enrichment of the reprograming signature, increasing from basal epithelial cells to club cells, followed by a decrease in signature gene expression toward luminal epithelial cells. In the Prostate Cell Atlas dataset[39], the reprogramming signature genes showed the highest enrichment in hillock and club epithelial cells. A similar pattern was observed in a dataset derived from treatment-naive patients with prostate adenocarcinoma[40], where hillock and club epithelial cells also showed the highest enrichment score. Finally, in a dataset composed of invasive cribriform carcinoma and intraductal carcinoma samples[41], reprogramming signature enrichment was observed in both BC/hillock and club/ductal cell populations (Fig. 6g). Furthermore, the levels of the markers associated with the different cell states during BC reprograming, including *AQP3*, *PIGR*, *KRT13* and *WFDC2*, were higher in hillock and club epithelial cells compared to other cell types across all the different human prostate cancer scRNA-seq datasets, as found for the combined signature (Fig. 6h and Extended Data Fig. 9a–f). Pseudotime lineage trajectory in human prostate cancer datasets showed that BCs differentiated into hillock or club-like cells before differentiating into luminal tumor cells (Extended Data Fig. 9g–i). These results show that the expression of the gene signature associated with the reprogramming of BCs into LCs following Pten deletion in mouse prostate tumor initiation is also found in human prostate cancers.

To further strengthen our analysis on human prostate cancer scRNA-seq datasets, we performed immunohistochemistry (IHC) staining of the selected reprogramming markers on 136 human prostate cancer specimens across various Gleason groups (GGs), including low-grade (GG1), intermediate-grade (GG2–3) and high-grade (GG4–5) prostate cancers. The hillock/hybrid marker AQP3, the proximal marker PIGR and the inflammatory marker STAT1 were expressed at higher level and in more tumor cells in patients with high-grade prostate cancers (Fig. 6i–l and Extended Data Fig. 9j). Altogether, these findings support the notion that cell fate reprogramming occurs in a subset of human prostate cancers with the most invasive features and that lineage reprogramming could serve as a predictive marker for aggressive disease.

Targeting innate immunity inhibits BC plasticity

To assess the functional consequences of the activation of innate immunity occurring following Pten deletion on SC plasticity, we pharmacologically inhibited these pathways and assessed the impact of their inhibition on basal to luminal transition (Fig. 7a). Administration of JSH-23, a small molecule inhibitor of NF-κB and ruxolitinib, a Janus kinase (JAK1 and JAK2) inhibitor 6 weeks following *Pten* deletion in BCs and 3 weeks after targeting *Pten-Pik3ca* in BCs decreased the differentiation of BCs into LCs (Fig. 7b,c). To assess whether the increased expression of *Il1* following *Pten* deletion in BC promotes the activation of innate immunity and cell plasticity in prostate epithelial cells, we treated the mice with anakinra, an IL-1R inhibitor[42]. Targeting IL-1 decreased *Pten*-induced cell plasticity and basal–luminal cell transition (Fig. 7d,e). In addition, these treatments also prevented the reprogramming of BCs into hillock and proximal-like states in AP and DLP (Fig. 7f–j). Notably, targeting IL-1, NF-κB and JAK–STAT signaling also decreased myeloid cell infiltration following *Pten* deletion and *Pik3ca* activation (Fig. 7k–m). These data demonstrate that targeting innate immunity inhibits the BC plasticity and reprogramming that occur following *Pten* deletion.

Fig. 8 | Cellular autonomous activation of Nfkb mediates BC plasticity and regional reprogramming following *Pten* deletion. a,**b**, Representative images and H&E staining of prostate organoids (**a**) and quantification of hyperplastic organoids after 5 days with or without TAM administration (**b**). Organoids are established from indicated mice. Scale bar, 50 µm. $n = 4$ independent experiments. **c**,**d**, Representative images of immunostaining of indicated prostate organoids (**c**) and quantification of % of YFP^+K8^+ (**d**) in total YFP^+ cells after TAM 5 days administration using indicated antibodies. Scale bar, 50 µm (up), 20 µm (down). $n = 3$ independent experiments. **e**–**g**, Representative images and immunostaining of DMSO-, JSH-23- (1 µM) and ruxolitinib-treated (10 µM) prostate organoids from K5-PTEN mice 5 days following TAM administration (**e**) and quantification of hyperplastic organoids (**f**) and YFP^+K8^+ (**g**) in total YFP^+ cells using indicated antibodies. Scale bar, 500 µm (up), 50 µm (down). $n = 3$ independent experiments. **h**,**i**, Representative FACS plot of CD49f and EpCAM expression in YFP^+ prostate epithelial cells (**h**) and quantification of the % of YFP^+ LCs (**i**) in total LCs in K5-PTEN and K5-PTEN-P65 mice 6 weeks after TAM administration. $n = 7$ mice. **j**, Representative prostate immunostainings of K5-PTEN 6w and K5-PTEN-P65 6w mice using indicated antibodies. Scale bar, 50 µm. $n = 3$ mice. **k**, Quantification of the % of YFP^+K8^+ in total $K8^+$ cells, YFP^+K13^+, YFP^+Aqp3^+ and YFP^+K4^+ in total YFP^+ cells ($n = 3$) and $Ly6G^+$ cells ($n = 4$) in DLP/AP. **l**, GO analysis of genes downregulated more than twofold in RNA-seq from FACS-isolated YFP^+ BCs from K5-PTEN-P65 6w mice compared to BCs from K5-PTEN 6w mice. **m**,**n**, Relative mRNA expression from bulk RNA-seq of FACS-isolated YFP^+ BCs from K5-PTEN 6w and K5-PTEN-P65 6w mice (data for genes regulating reprogramming, and cytokine/chemokine, interferon and NF-κB/TNF signaling pathways are shown in **m** and **n**, respectively). $n = 2$. **o**,**p**, H&E-stained histological sections of DLP (**o**) and quantification of the different histological lesions of prostate tumorigenesis (**p**) from K5-PTEN 6w and K5-PTEN-P65 6w mice. Scale bar, 50 µm. Number of mice (n) is indicated. Graphs show mean ± s.e.m. P values are derived from two-way (**b**) ANOVA with Tukey's test, one-way ANOVA with Dunnett test (**d**,**f**,**g**), two-sided unpaired t-test (**i**,**k**) and two-tailed modified Fisher's exact test with Benjamini–Hochberg correction (**l**).

https://doi.org/10.1038/s43018-025-00994-3

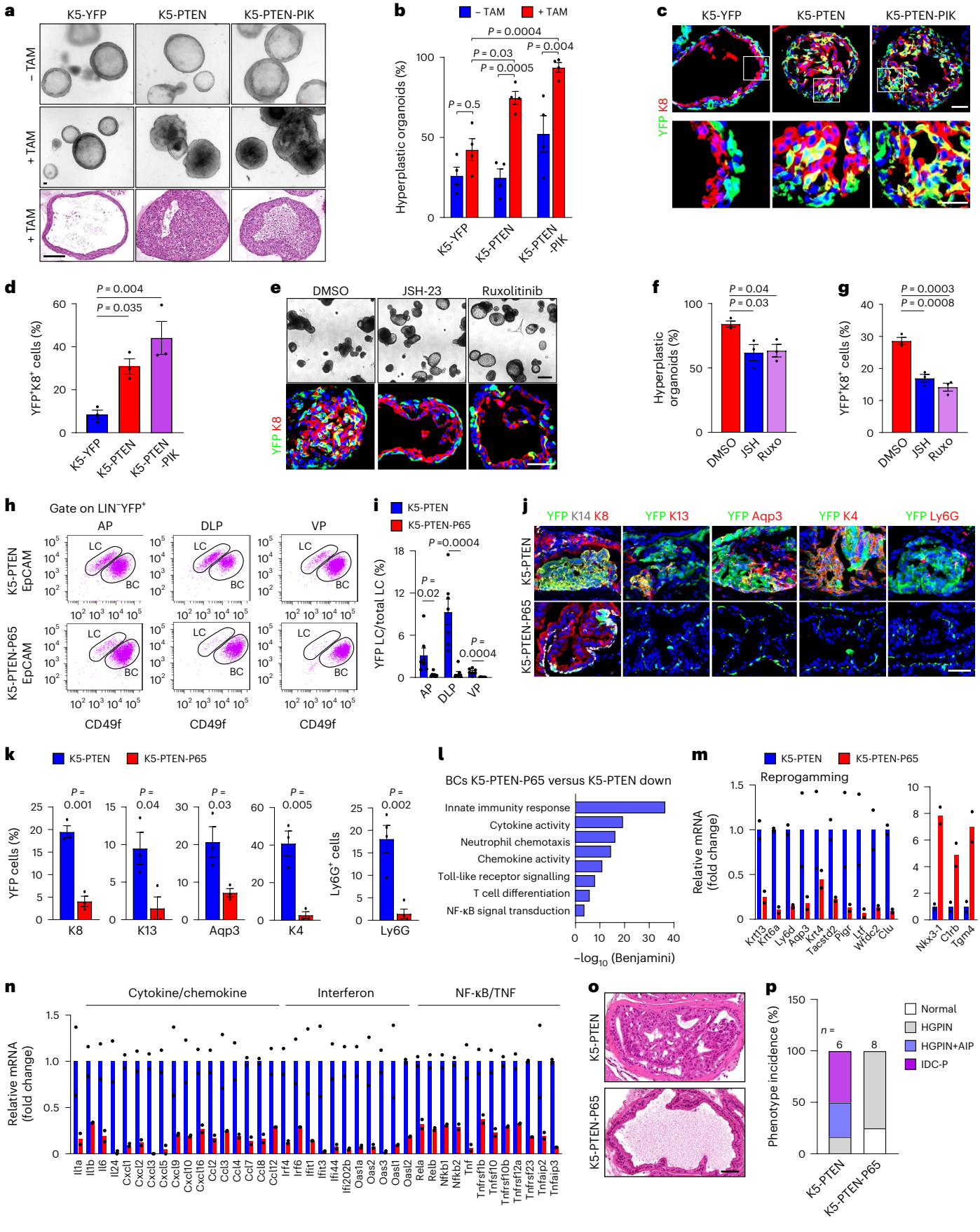

Cell autonomous role of innate immunity in BC plasticity

As *Pten* deletion and *Pten/Pik3ca* oncogenic hits promote the activation of innate immunity in prostate epithelial cells and the recruitment of innate immune cells in the prostate during prostate tumor initiation, we assessed whether these oncogenic stimuli promote cell plasticity and oncogenic induced reprogramming in vitro in the absence of stromal cells. To this end, we generated epithelial prostate organoids and assessed the impact of *Pten* or *Pten/Pik3ca* recombination on prostate epithelial cell states in vitro. Whereas in the absence of oncogenic hits, prostate organoids were composed of crowned of basal and luminal layers surrounding a lumen (hollow organoid), following *Pten* deletion and even faster following *Pten/Pik3ca* recombination in BCs, these organoids became hyperplastic with their lumens filled of cells (opaque organoid) (Fig. 8a,b). Immunostaining for YFP and K8 revealed that the hyperplastic organoids observed following *Pten* and *Pten/Pik3ca* recombination were filled with LCs coexpressing YFP and K8 (Fig. 8c,d). Treatment of these organoids with JSH-23 and ruxolitinib decreased the proportion of hyperplastic organoids and basal to luminal transition in vitro (Fig. 8e–g). These data demonstrate that BC SC plasticity following *Pten* deletion occurs in prostate organoid in vitro in the absence of stromal and immune cells and can be blocked by pharmacological inhibition of NF-κB and JAK–STAT pathways.

To assess that the cellular reprogramming of BCs into hillock cells and proximal-like LCs following *Pten* deletion in vivo is mediated by the activation of NF-κB in a cellular autonomous manner as suggested by the RNA-seq and ATAC-seq in vivo and by the organoid in vitro data, we performed the co-deletion of Rela/p65 subunit of the NF-κB complex together with *Pten* in BC (K5CreER/PTEN$^{fl/fl}$/P65$^{fl/fl}$/RosaYFP) and assess its impact on the BC plasticity and cellular reprogramming. The deletion of P65 in BCs together with *Pten* deletion strongly inhibited BC plasticity and the differentiation of BCs into LCs, the reprogramming of BCs into hillock and proximal LC-like states, as well as the recruitment of myeloid cells (Fig. 8h–k).

To define the role of p65 in *Pten* deletion mediated BC plasticity, we performed bulk RNA-seq of FACS-isolated BCs after *Pten* or *Pten/p65* deletion in BCs. Gene set enrichment analysis revealed the enrichment of genes regulating innate immunity, cytokine, chemokine, interferon and TNF/NF-κB signaling pathways in genes downregulated following *Pten/p65* deletion as well as genes associated with the hillock/hybrid/proximal-like reprogramming such as *Krt13*, *Aqp3*, *Krt4*, *Krt6a*, *Ly6d*, *Wfdc2*, *Pigr* and *Clu* (Fig. 8l–n). Of note, genes of the distal luminal like state such as *Nkx3.1*, *C1rb* and *Tgm4* were upregulated upon *Pten/p65* deletion (Fig. 8m,n). Of note, the strong inhibition of BC reprogramming and activation of inflammation/innate immunity following p65 deletion was accompanied by a major reduction in prostate tumorigenesis (Fig. 8o,p).

Altogether these data demonstrate that the *Pten*-induced BC plasticity is mediated by the activation of innate immunity and the NF-κB signaling pathway in prostate epithelial cells in a cellular autonomous manner.

Discussion

In this study, we uncovered the importance of the cells of origin and regionalization in regulating prostate tumor heterogeneity and the molecular mechanisms controlling SC plasticity and lineage infidelity following oncogenic hits during the early stage of prostate tumorigenesis (Extended Data Fig. 10).

Our results reconcile conflicting findings regarding the differential tumor phenotypes arising from BCs and LCs[4–6]. We demonstrate that BCs from the AP and DLP give rise to more invasive tumors compared to BCs from the VPs and LCs; however, tumorigenesis is more rapid when initiated in VP-derived LCs. The observation that BC-derived tumors are more aggressive in AP and DLP aligns with the findings of Lu et al.[4]. Our findings emphasize that tumor progression is strongly influenced by the prostate lobe from which the tumor originates, an aspect often overlooked in previous studies potentially explaining the discrepancies between the different studies[5,6]. Notably, this variation in tumor phenotype correlates with different patterns of cellular reprogramming following *Pten* deletion.

We identify a previously unexplored reprogramming trajectory in BCs from AP and DLP upon *Pten* deletion, which undergoes a stepwise transition through hillock cells and a hybrid basal–luminal state before differentiating into proximal-like LCs. Hillock cells, marked by *Krt13* expression, have been reported in the human proximal prostate near the prostate–urethra junction[9,31–33], but their role in tumor initiation remains unexplored. These different cell states that arise following *Pten* deletion in BCs from AP and DLP persist in more advanced tumors and maintain their proximal luminal differentiation features. As proximal LCs were proposed to present increased self-renewing potential[10–12,43–46], it is possible that this proximal luminal state confers stemness and multilineage differentiation to the cells of origin of prostate cancer that boost their tumorigenic potential. In contrast, VP BCs follow a distinct differentiation pathway, transitioning directly into distal-like LCs with lower plasticity and slower tumor progression. Unlike BCs, LCs fail to reactivate multipotent programs following *Pten* deletion, and their tumors exhibit reduced immune infiltration and collagen deposition. Due to health issues linked to the expression of K5CreER in other tissues, the long-term consequences of these histological differences in prostate tumor progression, such as metastasis or animal survival, could not be assessed in our model.

Our findings have important implications for human prostate cancer. Like the mouse prostate, the human prostate consists of three distinct zones: the peripheral, transition and central zones[47,48]. Notably, approximately 70% of prostate cancers arise in the peripheral zone, where tumors exhibit more aggressive features and worse clinical outcomes compared to transition zone derived tumors[47–49]. Transcriptomic analyses indicate that the human peripheral zone resembles the mouse DLP[11,50], suggesting conserved regional influences on prostate tumorigenesis.

The difference in BC plasticity and cellular reprogramming across the different lobes are accompanied by different remodeling of the tumor microenvironment (TME). BC-hillock-hybrid-proximal reprogramming in AP/DLP is associated with extensive ECM remodeling, desmoplastic stroma formation and enhanced myeloid cell recruitment. This correlates with elevated expression of collagens, ECM components, metalloproteases and inflammatory mediators. These results indicate that the cellular origin and regional context of oncogene-driven reprogramming control the remodeling of TME, reinforcing cell plasticity and accelerating tumor progression.

At the mechanistic level, our transcriptomic and chromatin profiling show that upon oncogenic hits, BCs activate innate immunity including NF-κB, JAK–STAT and interferon. Previous studies have linked *Pten* deletion in prostatic epithelium to the activation of a senescence-associated secretory phenotype[51–53], which has been shown to recruit myeloid cells that, in turn, inhibits senescence, promotes tumor progression and the development of castration-resistant tumors[53–57]. Our data show that inhibition of JAK–STAT and NF-κB decreases SC plasticity and basal to luminal transition following *Pten* deletion in BCs. Increased JAK–STAT inflammatory signals have been observed during the development of androgen-resistant prostate cancer and the switch from prostate adenocarcinoma to neuroendocrine cancer, suggesting that the emergence of tumor plasticity at the later state of prostate cancer also depends on an increased inflammatory state[35,58]. JAK–STAT signals have recently been found to sustain Nkx3.1-expressing BCs during homeostasis[59]. *Pten* deletion induces the upregulation of *Il1a* and its receptor *Il1r1* in BCs, activating the innate immune pathway in hybrid cells. Inhibition of IL-1R decreases basal SC plasticity, supporting the notion that IL-1/IL-1R expression in BC following *Pten* deletion mediates an autocrine loop that sustains BC plasticity, and the cellular reprogramming associated with tumor initiation. *Pten* deletion in vitro in prostate organoid BCs

promotes BC plasticity and luminal differentiation and deletion of *p65/Rela* in BCs demonstrate that this activation of the immune immunity pathway in *Pten* targeted epithelial cells is mediated by a cellular autonomous mechanism. Taken together, our study demonstrates that innate immunity activation in BCs is essential for cell plasticity, inflammation and tumor initiation, revealing key molecular mechanisms linking *Pten*-driven inflammation to prostate cancer initiation and progression. These mechanisms that promote SC plasticity may also be relevant to the initiation of other cancers.

Our study establishes that reprogramming signatures and the hillock-like state identified in *Pten*-deleted mouse BCs are also present cells in human prostate cancer across four independent single-cell RNA-seq datasets[38–41]. These cells display transcriptomic profiles resembling castration-resistant prostate cancer[9,12,33,60] and are linked to inflammation and myeloid infiltration[61,62]. The presence of hillock and club-like cells in later stages of human prostate may reflect either their progressive accumulation over time during tumorigenesis as the lineage trajectory analysis suggests or indicate the activation of lineage plasticity at later stages of tumor progression. Furthermore, IHC analyses of a large human prostate cancer cohort reveal that the expression of hillock marker AQP3, club-like marker PIGR and inflammatory marker STAT1 correlates with high-grade tumors. This suggests that BC plasticity and differentiation trajectories are not uniform across all prostate cancers, and that lineage reprogramming could serve as a predictive biomarker for aggressive disease.

In conclusion, our study uncovers a fundamental link between the cells of origin, regional influences and tumor plasticity in prostate cancer initiation. We demonstrate that innate immunity activation in BCs is crucial for SC plasticity, inflammation and tumor progression. By identifying reprogramming-associated immune pathways as key drivers of tumor initiation, our findings open new avenues for therapeutic interventions targeting inflammation-induced plasticity in prostate cancer and potentially other malignancies.

Methods

Ethical statement

Mice colonies were housed in a certified animal facility in compliance with European guidelines. The room temperature was maintained between 20 and 24 °C, with relative humidity kept at 55 ± 10%. Food, water and two types of nesting material were provided in each cage. A semi-natural light 12-h light–dark cycle was implemented. All animal experiments were approved by the ethical committee (Commission d'Ethique et du Bien Être Animal; CEBEA) of the Faculty of Medicine, Université Libre de Bruxelles under protocols 673N, 854N and 914N. CEBEA follows the European Convention for the Protection of Vertebrate Animals used for Experimental and other Scientific Purposes. As prostate tumors grow intra-abdominally, humane end points based on general health and a 20% body weight loss limit, approved by CEBEA, were not exceeded in this study. Male mice were used at adult age (over 8 weeks) for the prostate analysis.

Mouse genetic lineage tracing

The generation of K5CreER and K8-CreERT2 was previously described[63]. Rosa26-YFP and Pten$^{fl/fl}$ mice were obtained from the Jackson Laboratory. Pik3caH1047R knock-in mice, in which WT exon 20 is replaced by H1047R mutant exon 20 upon Cre recombination, were described previously[64]. P53$^{fl/fl}$ mice[65] were obtained from the National Cancer Institute at Frederick. P65$^{fl/fl}$ mice[66] were imported from M. Pasparakis's laboratory. Male mice with a mixed genetic background were used in this study. Mice were induced with 15 mg of TAM (T5648; diluted in sunflower seed oil, Sigma) by i.p. injection (three injections of 5 mg every 2 days). For a long trace (over 12 weeks) of K5CreER/Pten$^{fl/fl}$/RosaYFP mice, the TAM injection was reduced to 6–10 mg. For K5CreER/Pten$^{fl/fl}$/Pik3ca^{H1047R}/RosaYFP mice and K5CreER/Pten$^{fl/fl}$/P53$^{fl/fl}$/RosaYFP mice, the TAM injection reduced to 10 mg (three injections of 3.3 mg every 4 days).

Intraprostatic adenoviral infection

Intraprostatic adenoviral infection was performed as previously described[67–69]. In brief, AdeK5Cre (Ad5-bK5-Cre) (A. Berns, Netherlands Cancer Institute) were obtained at high titer (8×10^{10} to 2×10^{10} plaque-forming units per ml) from Viral Vector Core at University of Iowa. Then, 1 µl of AdeK5Cre was mixed with 9 µl of organoid medium containing 16 µg ml^{-1} Polybrene (Millipore Sigma). A total of 10 µl of this adenoviral solution was injected into the AP of transgenic mice as described in the figure legends.

Immunostaining

Prostate tissue from adult mice was micro-dissected under a stereoscope to isolate the different prostate lobes. The dissected lobes were fixed in 4% PFA at room temperature (RT) for 2 h. Tissues were washed with PBS and then incubated overnight at 4 °C in 30% sucrose. Samples were subsequently embedded in OCT and stored at −80 °C. Prostate organoids were collected in cold basal medium, washed with cold PBS and then fixed in 4% PFA for 30 min. After washing, organoids were embedded in OCT and stored at −80 °C.

Cryosections of 5 µm were cut using an HM560 Microm cryostat (Mikron Instrument). Sections were blocked in buffer containing 1% BSA, 5% HS, 0.2% Triton X-100 in PBS for 1 h at RT. Primary antibodies, diluted in blocking buffer, were incubated overnight at 4 °C. The sections were then washed three times in PBS and incubated with secondary antibodies diluted in blocking buffer for 1 h at RT. Detailed antibody information is provided in Supplementary Table. Nuclei (blue) were stained using Hoechst solution (1:1,000 dilution), and slides were mounted with DAKO mounting medium (Sigma). Images were acquired at RT using a Zeiss Axioscan 7, an LSM780 confocal microscope fitted on an Axiovert M200 inverted microscope equipped with a C-Apochromat (×40, $A = 1.2$) water immersion objective and using a Zeiss Axio Imager M2 fluorescence microscope with a Zeiss Axiocam MR3 camera using Axiovision v.4.8 software. Brightness, contrast, picture size and analyses were performed using ZEN software and Adobe Photoshop CS6.

EdU experiments

Male mice were injected with a single i.p. injection of EdU (2.5 mg ml^{-1} in PBS) 24 h before killing. EdU staining was performed according to the manufacturer's instructions (Thermo Fisher Scientific, c10340). For co-expression with EdU, the K14 or K8 primary antibody staining was performed first, and then the EdU protocol was followed.

H&E staining and prostate tumor classification

Hematoxylin & eosin (H&E) staining was performed on paraffin-embedded sections using standard laboratory protocols. Histological assessments of mice prostate samples were performed by an expert uropathologist by assimilating the histological criteria observed in human prostate according to the 2022 WHO classification[70]. Lesions were categorized as normal, HGPIN, atypical intraductal proliferation (AIP), intraductal carcinoma of the prostate (IDC-P) and invasive adenocarcinoma (ADC). As defined in the 2022 WHO classification, HGPIN is considered to be the earliest histologically recognizable precursor of ADC (exhibiting only a tufting, micropapillary or flat pattern), whereas AIP is characterized by atypical cribriform proliferations that do not reach the threshold for IDC-P. To approach tumor formation heterogeneity across samples, IDC-P was categorized as focal or florid based on the percentage of IDC-P observed (<50% or ≥50%). The morphological appearance of the tumor stroma was characterized as normal, slightly inflammatory (edematous), highly inflammatory or desmoplastic.

Pharmacological treatments in vivo

Mice over 8 weeks old were injected with TAM as described previously. After that, rapamycin (i.p., 6 mg kg^{-1} body weight, MedChemExpress, HY-10219), JSH-23 (i.p., 6 mg kg^{-1} body weight, MedChemExpress,

HY-13982), ruxolitinib (i.p., 10 mg kg^{-1} body weight, MedChemExpress, HY-50856) and Anakinra (i.p., 10 mg kg^{-1} body weight, Sobi, Kineret) were injected into mice. Rapamycin was dissolved in ethanol to get 40 mg ml^{-1} and then diluted in buffer (10% PEG400 and 10% Tween 80) to reach 1 mg ml^{-1} rapamycin. As a control, the same amount of ethanol diluted in buffer was injected into the mice. JSH-23 and ruxolitinib were first dissolved in dimethylsulfoxide (DMSO) to get 40 mg ml^{-1} and then diluted in buffer (50% saline, 45% PEG400 and 5% Tween 80). As a control, the same amount of DMSO was diluted in buffer and then injected into the mice. Anakinra (100 mg per 0.67 ml) was diluted in saline to get 2 mg ml^{-1}. As a control, the same amount of saline was injected into the mice. For K5CreER/$Pten^{fl/fl}$/RosaYFP mice, the rapamycin, JSH-23 and ruxolitinib injection started 1 week after the TAM injection for 5 weeks continuously (three injections per week, every 2 days). Anakinra was injected 4 weeks after the TAM injection continuously for 2 weeks (three injections per week, every 2 days). For K5CreER/$Pten^{fl/fl}$/$Pik3ca^{H1047R}$/RosaYFP mice, the rapamycin, JSH-23, ruxolitinib and anakinra injection started after the first TAM injection for 3 weeks continuously (three injections per week, every 2 days).

Cell labeling, flow cytometry and sorting

The mouse prostate single cell preparation was obtained as previously described[22]. In brief, prostate tissues, including the VP, DLP and AP were isolated from indicated mouse lines at indicated time points after TAM injection. Tissues were minced in a 6-cm culture plate and digested in 5 mg ml^{-1} collagenase type II (Life Technologies, 17101-015) with 10 µM Y-27632 dihydrochloride (Abmole Bioscience, M1817) for 1.5–2 h at 37 °C on a shaking platform. Glandular structures were then washed with Advanced DMEM/F12 and centrifuged at 150*g* for 5 min at 4 °C. Structures were further digested in trypsin for 10–20 min at 37 °C and trypsin activity was quenched using 2% FBS in PBS. Cells were passed through a 40-µm cell strainer and incubated with fluorochrome-conjugated primary antibodies for 30 min on ice with shaking every 10 min. Detailed antibody information is provided in Supplementary Table. Cells were washed with 2% FBS/PBS and resuspended in 4,6-diamidino-2-phenylindole (DAPI) or Hoechst before analysis. Data analysis and cell sorting were performed on a FACSAria sorter or LSRFortessa using FACS DiVa software (BD Biosciences). Dead cells ($DAPI^+$) and Lin^+ ($CD45^+$, $CD31^+$ and $CD140a^+$) cells were excluded before analysis. Due to technical challenges in obtaining enough BC-derived LCs from adult WT mice, LCs isolated from adult CD1 mice were used to compare to LCs arising from *Pten*-deleted BCs. The following populations were analyzed and sorted: $DAPI^-LIN^-YFP^+CD49f^{high}EpCAM^+$ (for BCs) and $DAPI^-LIN^-YFP^+CD49f^{low}EpCAM^+$ (for LCs).

Western blot

Prostate epithelial cells were FACS-isolated as described in the section 'Cell labeling, flow cytometry and sorting'. To obtain sufficient protein, around 500,000 $DAPI^-LIN^-$ epithelial cells from CTL mice and $DAPI^-LIN^-YFP^+$ epithelial cells from K5CreER/$Pten^{fl/fl}$/RosaYFP mice 6 weeks after TAM administration were FACS-isolated from the whole prostate of at least three mice. Cells were lysed in cell lysis buffer (Cell Signaling, 9803) supplemented with a phosphatase inhibitor cocktail (Cell Signaling, 5870) and 1 mM phenylmethyl sulfonyl fluoride (PMSF) (Sigma, P7626) on ice for 5 min. The lysates were sonicated (5 × 10 s) and centrifuged at 14,000*g* for 10 min at 4 °C. Cell lysate mixed with loading buffer were heated at 99 °C for 5 min, then loaded in NuPage 10% Bis-Tris gel (Invitrogen, NP0315BOX) and separated by electrophoresis. Proteins were transferred to PVDF membranes, blocked in 5% milk for 1 h and incubated overnight with primary antibodies (details are in Supplementary Table). The membrane was re-probed after incubation in stripping buffer (Invitrogen, 46430) for 15 min. Anti-rabbit IgG conjugated with horseradish peroxidase (HRP) (1:5,000 dilution, Sigma-Aldrich, Gena9340) was used as the secondary antibody. Blots were developed using an iBright 1500 (Invitrogen).

Prostate organoids experiments

Prostate organoids experiments were performed as previously described[71,72]. In brief, whole prostate tissues were collected from indicated mouse lines. Tissues were minced in a 6-cm culture plate and digested in 5 mg ml^{-1} collagenase type II with 10 µM Y-27632 for 1–1.5 h at 37 °C on a shaker. Glandular structures were then washed with Advanced DMEM/F12 and centrifuged at 150*g* for 5 min at 4 °C. After that, the structures were digested in 1 ml TrypLE (Life Technologies, 12605-010) with Y-2763210 µM at 37 °C for 10 min. Structures were washed and mixed in Matrigel (Corning, 356231) at a dilution of 2:1 (Matrigel:basal medium). A 40-µl drop of this mixture was plated in the center of 24-well plate. The plate was turned upside down in a CO_2 incubator (5% CO_2, 37 °C) for 15 min to allow the Matrigel to solidify. Organoids were cultured in Advanced DMEM/F12 supplemented with B27 (Life Technologies, 17504-044), 10 mM HEPES (Life Technologies, 15630-056), GlutaMAX (Life Technologies, 35050-068), penicillin–streptomycin (Life Technologies, 15140-122), 1.25 mM *N*-acetylcysteine (Sigma-Aldrich, A9165), 100 ng ml^{-1} recombinant Noggin (Peprotech, 250-38), 100 ng ml^{-1} recombinant R-spondin1 (R&D Systems, 3474-RS-250), 50 ng ml^{-1} EGF (PeproTech, AF-100-15), 1 nM dihydrotestosterone (Sigma, A8380), 200 nM A83-01 (Tocris Bioscience, 2939) and 10 µM ROCK inhibitor Y-27632 (only for the first week). To activate Cre recombinase and trace BCs, fully established organoids (after 5–7 days) were treated with 1 µM of 4-OH-TAM for 48 h. Afterwards, the medium was refreshed every 2–3 days without TAM. DMSO (0.1%), JSH-23 (1 µM) and ruxolitinib (10 µM) were maintained in the medium before collection for analysis.

RNA sequencing

Mouse prostate BCs and LCs were FACS-isolated as described in 'Cell labeling, flow cytometry and sorting'. RNA was extracted from FACS-isolated cells using the RNeasy Micro kit (QIAGEN), following the manufacturer's instructions. Before sequencing, the quality of RNA was evaluated by Bioanalyzer 2100 (Agilent). Indexed complementary DNA libraries were prepared using the Ovation Solo RNA-seq System (NuGEN) according to the manufacturer's instructions. Multiplexed libraries were loaded onto flow cells and sequenced using the NovaSeq 6000 S2 Reagent kit (200 cycles) on a NovaSeq 6000 System (Illumina). Sequencing generated approximately 25 million paired-end reads per sample.

RNA-seq analysis

The quality of each raw dataset was assessed using FastQC (https://www.bioinformatics.babraham.ac.uk/projects/fastqc/). The adaptor sequences and low-quality regions were trimmed by TrimmomaticPE (v.0.39)[73]. Trimmed reads were aligned to the mouse reference genome (Grcm38.87) using the STAR aligner (v.2.7.5a)[74]. Genome annotations for Grcm38.87 were obtained from Ensembl (ftp.Ensembl.org). Duplicate reads were removed using the Picard (v.2.1.1; http://broadinstitute.github.io/picard/) MarkDuplicates. Following transcript assembly, gene-level counts were generated with HTSeq (v.0.11.1)[75] and normalized to a count per 20 million. The average gene expression of each gene was calculated for each cell population using at least two biological replicates and fold changes were computed between subpopulations.

For the differentially regulated genes across the conditions, genes with a fold change ≥ 2 were classified as upregulated, while those with a fold change ≤ 0.5 were classified as downregulated. Genes with fewer than ten counts in any individual sample were excluded from the differential expression analysis. Genes upregulated in each signature were tested for enrichment in each Gene Ontology (GO) class using the DAVID[76] v.2023q4 web server.

ATAC sequencing

For ATAC-seq, 100,000 BCs and LCs were FACS-isolated from pooled mouse prostate lobes (>3 mice). For lobe-specific analysis, BCs were separately FACS-isolated from the VP, DLP and AP. Sorted cells were collected in 1 ml PBS with 3% FBS on ice. Cells were centrifuged and

cell pellets were resuspended in 100 µl lysis buffer (Tris-HCl 10 mM, NaCl 10 mM, $MgCl_2$ 3 mM and Igepal 0.1%). Following centrifugation at 500*g* for 25 min at 4 °C, nuclei were resuspended in 50 µl tagmentation mix (Nextera DNA Sample Preparation kit, Illumina). The reaction was performed at 37 °C for 30 min and DNA was purified using the MiniElute purification kit (QIAGEN) following the manufacturer's protocol. DNA libraries were PCR amplified (Nextera DNA Sample Preparation kit, Illumina) and size selected from 200 to 800 bp (BluePippin, Sage Sciences), following the manufacturer's recommendations.

ATAC-seq analysis

Adaptor sequences were trimmed using TrimmomaticPE (v.0.39)[73] with the following parameters: HEADCROP:10 CROP:70 ILLUMINACLIP:adaptor_file:2:30:10 LEADING:3 TRAILING:3 SLIDINGWINDOW:4:15 MINLEN:36. ATAC-seq paired-end reads were then aligned to mouse reference genome (Grcm38) using Bowtie2 (v.2.2.6)[77] with the parameters: X 2,000 --fr --very-sensitive --no-discordant --no-unal --no-mixed --nondeterministic. Mitochondrial reads, reads mapped to unmapped or random contigs and those with a mapping quality below 20 were removed using SAMtools[78]. Duplicate reads were suppressed by the Picard (v.2.1.1) MarkDuplicates module. Peak on each individual sample were called using MACS2 (v.2.1.0.20151222)[79] with the parameters: -f BAMPE -g mm --nomodel --shift 0 -q 0.01. Peaks from the different subpopulations were merged for downstream analysis. Reads counts for each merged peak in individual samples were calculated by HTSeq-count[75] using the options '-f bam -r pos -m intersection-nonempty'. These counts were normalized to one million mapped reads in merged peaks and fold change was calculated compared to the control. Peaks were associated with genes using GREAT software (v.4.0.4)[80] with the following parameters: 5.0 kb in proximal upstream, 1.0 kb in proximal downstream and 100.0 kb in distal. For further analysis, the peaks that were not annotated to any of genes were excluded. Differential peaks are defined as peaks having at least a twofold change compared to the control and being called peak in the expanded condition.

De novo motif search was performed using findMotifsGenome.pl tool in the HOMER suite[81], searching for motifs 6–12 bp within ±250 bp from the peak center. For motif prediction, differently regulated peaks are given as targets, while nonregulated peaks from the merged peak set, identified using the intersect function of BEDTools (v.2.27.0)[82], were used as the background.

Single-cell RNA sequencing

For CD1 mice, all epithelial cells, including BCs and LCs (LIN^- and $EpCAM^+$) were FACS-isolated. For K5CreER/$Pten^{fl/fl}$/RosaYFP mice after a 6-week TAM induction, BCs ($LIN^-YFP^+CD49f^{high}EpCAM^+$), LCs ($LIN^-YFP^+CD49f^{low}EpCAM^+$) and intermediated cells were FACS-isolated. For K5CreER/$Pten^{fl/fl}$/RosaYFP mice after a 10-month TAM induction, $LIN^-YFP^+EpCAM^+$ cells were FACS-isolated.

Single cells were dissociated and loaded onto Chromium Single Cell 3′ microfluidic chips (V2-chemistry, PN-120232, 10x Genomics) and barcoded with a 10x Chromium controller according to the manufacturer's recommendations. RNA was reverse transcribed, amplified and processed for 5′ adaptor ligation and index attachment. Libraries were generated with the Chromium Single Cell 3′ Library kit (V3-chemistry, PN-120233, 10x Genomics) and sequenced on an Illumina Novaseq 6000 (paired-end, 100-bp reads).

Single-cell transcriptomic data analysis

Sequencing reads were aligned and annotated with the mm10-2020-A reference dataset as provided by 10x Genomics and demultiplexed using Cell Ranger (v.6.0.0)[83] using default parameters.

Quality control and downstream analysis were performed using the Seurat R package (v.4.2.0)[84]. For each sample, cells were retained if they expressed between 2,500 and 7,500 unique genes and had less than 15% of total unique molecular identifier counts derived from mitochondrial transcripts. Read counts were normalized with the NormalizeData() function of Seurat, with parameter 'normalization.method = logNormalize' and 'scale.factor = 10,000'. Principal-component analysis (PCA)[85] were performed for each sample was calculated using the scaled expression data of the 2,000 most variable genes, identified as outliers on a mean–variability plot via the FindVariableGenes() function. Uniform Manifold Approximation and Projection (UMAP)[86] and graph-based clustering were carried out using Seurat with default parameters, using the first 30 principal components as input.

Clusters showing high expression of stromal (*Vim*, *Zeb2* and *Fscn*), fibroblast (*Pdgfra*, *Fn1*, *Col1a1* and *Fbn1*) and macrophage markers (*Ptprc*, *Cd86*, *Cd68* and *Ccr1*) were excluded. Dimensionality reduction was recalculated after removal of these nonepithelial cell populations. The final clustering resolution was selected based on epithelial heterogeneity, including BCs (*Krt14*, *Krt5* and *Trp63*), proximal prostate (*Krt4*, *Psca*, *Wfdc2*, *Clu*, *Ppp1r1b* and *Ltf*), anterior–dorsal (*Nkx3.1*, *Tgm* and *Gsdma*), ventral (*Sbp*, *Sbpl* and *Spink1*) and lateral lobes (*Msmb* and *Cldn10*). Upon *Pten* deletion, additional cell populations composed of hillock (*Krt13*), hybrid (*Krt6a*, *Ly6d*, *C1rb* and *Ren1*), chemokine-enriched LCs (*Cxcl1*, *Cxcl2*, *Cxcl5* and *Cx3cr1*), interferon-enriched LCs (*Irf7*, *Ifit1*, *Ifitm1*, *Ifitm2*, *Ifi202b* and *Irf6*) and major histocompatibility complex class II antigen-enriched LCs (*Cd74*, *H2-Aa*, *H2-Ab1* and *H2-DMb1*) had emerged. Cell cycle phases were inferred using CellCycleScoring() in Seurat, based on S phase and G2/M gene expression.

Marker genes for each cluster were identified using the Wilcoxon rank-sum test implemented in the FindAllMarkers() function in Seurat. *P* values were adjusted using the Benjamini–Hochberg false discovery rate (FDR)[87] method in R. Genes expressed in ≥25% of cells within a cluster and with an average $\log_2$ fold change ≥ 0.25 were retained. Differentially expressed genes in the hybrid and hillock populations were identified using the FindMarkers() function in Seurat (parameters, logfc.threshold = 0.25, min.pct = 0.25, only.pos = T). Genes with FDR-adjusted $P < 0.01$ were considered significant.

BC/LC-specific markers were defined from the WT dataset as genes with an average $\log_2$ fold change > 0.5, adjusted $P < 0.01$ and expression in ≥35% of the respective population. For each cell, the proportion of expressed markers was adjusted by modeling its linear relationship with the total number of genes detected, to correct the differences in sensitivity due to the different sequencing depth per sample.

Gene regulatory network analysis was performed using pySCENIC (v.0.11.2)[36] with default parameters. To correct for stochastic variation, the pipeline was run ten times for the dataset and the average AUC (area under the curve) scores were calculated for downstream analysis. Differentially activated regulons for each cluster were identified by a Wilcoxon rank-sum test of AUC values across clusters. Regulons with an adjusted $P < 0.01$ were considered significantly activated.

Lineage trajectory inference was performed using Slingshot (v.2.0.0)[88]. To reduce pseudotime distortions from proliferative states, cells and clusters with high expression of proliferation or metabolism-related genes were excluded. Trajectory robustness was confirmed by consistent results across PCA- and UMAP-based embeddings and multiple permutations.

Quantitative RT–PCR

Total RNA of FACS-isolated BCs was extracted using the Direct-zol RNA Microprep kit (Zymo) following the manufacturer's instructions. Genomic DNA was removed by on-column DNase treatment. Complementary DNA was synthesized using the RevertAid First Strand cDNA Synthesis kit (Thermo Fisher). Quantitative reverse transcription PCR (qRT–PCR) was performed using SYBR Green Supermix (Applied Bioscience) on a Light Cycler 96 system (Roche). Relative gene expression was normalized to the housekeeping gene *Gapdh*. The following probes from Eurogentec were used: *Gapdh* forward: AGGTCGGTGTGAACGGATTTG, *Gapdh* reverse: TGTAGACCATGTAGTTGAGGTCA, *Ila1*

forward: CGAAGACTACAGTTCTGCCATT, *Il1a1* reverse: GACGTTTCAGAGGTTCTCAGAG, Cxcl2 forward: CCAACCACCAGGCTACAGG and Cxcl2 reverse: GCGTCACACTCAAGCTCTG.

Human public single-cell data analysis

Processed human prostate cancer datasets were downloaded from the GitHub repository of the author[38], the Prostate Cell Atlas[39] and the Gene Expression Omnibus (GEO) database under accession numbers GSE181294 (ref. 40) and GSE185344 (ref. 41). For datasets not originally provided as Seurat objects, data were imported and converted using the Seurat R package (v.4.2.0)[84] to enable downstream analysis.

Reprogramming gene signatures were derived from our PTEN 6w scRNA-seq dataset using a Wilcoxon rank-sum test via the FindAllMarkers() function in Seurat. *P* values were adjusted with the Benjamini–Hochberg FDR method[87] using the p.adjust() function in R. Genes expressed in BC hillock, hybrid BC proximal-like (HY BC prox), or proximal populations in ≥35% of cells, with average $\log_2$ fold change ≥ 0.85 and adjusted *P* value < 0.01 were retained. The top 16 differentially expressed genes per cluster were selected for downstream analysis. Mouse-to-human orthologs were identified using Ensembl BioMart by aligning Grcm38.87 (mouse) to GRCh38 (human).

Gene set enrichment analysis across four public human datasets was performed using AddModuleScore() in Seurat (default parameters). Module scores and marker gene expression were visualized with ggplot2 (v.3.5.1) and viridis R package (v.0.6.5).

IHC staining on human prostate cancer sections

Formalin-fixed, paraffin-embedded human prostate cancer samples representing different GGs were collected from the Centre Universitaire inter Regional d'Expertise en Anatomie Pathologique Hospitalière (CurePath), Jumet, Belgium. Histopathological diagnoses were reviewed according to the 2022 WHO Classification[70]. For each patient, one representative paraffin was used for immunohistochemical analyses. IHC for STAT1 and PIGR was performed on 4-µm formalin-fixed, paraffin-embedded sections using the Ventana Discovery ULTRA (Ventana Medical Systems) and the ChromoMap detection system according to the manufacturer's protocols. Tissue sections were deparaffinized, rehydrated and subject to antigen retrieval using Discovery Cell Conditioner 1 (Tris–EDTA, pH 7.8; Roche) for 40 min at 95 °C. Slides were incubated with peroxidase blocking solution for 16 min. Primary antibodies were diluted in Discovery Antibody Diluent and incubated with anti-PIGR at 60 °C for 60 min and anti-STAT1 at 37 °C for 60 min. Tissues were then incubated EnVision Flex-HRP (Agilent, K400311-2) at 37 °C for 2 h. AQP3 immunostaining was performed on the Autostainer Link 48 (Agilent Technologies). Tissue sections were deparaffinized, rehydrated and subject to antigen retrieval using EnVision FLEX Target Retrieval High pH Solution (EDTA, pH 9; Agilent, K800421-2), for 30 min at 97 °C on the PT Link (Agilent Technologies). Peroxidase blocking was performed for 5 min, followed by incubation with anti-AQP3 at RT for 30 min. The slides were washed and incubated with the EnVision+System-HRP labeled polymer anti-rabbit Ig antibody for 20 min (Agilent, K400311-2). The signal was developed using diaminobenzidine and hydrogen peroxidase, followed by hematoxylin staining, dehydration and mounting. Whole-slide imaging was performed using a NanoZoomer S360 (×20 magnification, 0.46 µm per pixel, Hamamatsu).

Statistical analysis and reproducibility

Statistical analyses based on biological replicates or independent experiments were performed using GraphPad Prism v.8.00, R (v.4.2.0) and Excel, with the methods and exact *P* values indicated in each figure and legend. Two-sided unpaired *t*-tests were used for two-group comparisons, while analysis of variance (ANOVA) followed by post hoc tests was used for comparisons involving more than two groups. No statistical methods were used to predetermine sample sizes, but our sample sizes are similar to those reported in previous publications[8,72]. Mice with low induction efficiency were excluded from the analysis and no other data were excluded. Individual data points were shown and were assumed to be normal, but this was not formally tested. Data collection and analysis were not performed blind to the conditions of the experiments. For the drug treatment, male mice were randomly divided into different treatment groups at the same age and genotype.

Reporting summary

Further information on research design is available in the Nature Portfolio Reporting Summary linked to this article.

Data availability

All raw sequencing datasets that support the findings of this study have been deposited in the GEO under accession number GSE270187 (scRNA-seq), GSE270189 (bulk RNA-seq, rapamycin treated), GSE270190 (bulk RNA-seq, cell fate upon PTEN deletion in BC), GSE286018 (bulk RNA-seq of P65/Pten knock BCs), GSE286019 (bulk RNA-seq of basal-derived and luminal-derived luminal tumors), GSE270191 (ATAC-seq of pooled BC/LC of WT and PTEN-deleted cells) and GSE288787 (ATAC-seq of BCs from different lobes upon PTEN deletion). Previously published human prostate cancer datasets re-analyzed in this study were available from GitHub repository of the author (https://github.com/franklinhuanglab/scRNA-seq-Analysis-of-Prostate-Cancer-Samples)[38], the Prostate Cell Atlas (https://www.prostatecellatlas.org)[39] and GEO GSE181294 (ref. 40) and GSE185344 (ref. 41). The data that support the findings of this study are available from the corresponding author upon request. Source data are provided with this paper.

Code availability

The codes used for data processing, downstream analysis and plotting for this paper are available on GitHub at https://github.com/yurasong/PTEN_codes.

References

1. Toivanen, R. & Shen, M. M. Prostate organogenesis: tissue induction, hormonal regulation and cell type specification. *Development* **144**, 1382–1398 (2017).
2. Ousset, M. et al. Multipotent and unipotent progenitors contribute to prostate postnatal development. *Nat. Cell Biol.* **14**, 1131–1138 (2012).
3. Blanpain, C. & Fuchs, E. Stem cell plasticity. Plasticity of epithelial stem cells in tissue regeneration. *Science* **344**, 1242281 (2014).
4. Lu, T. L. et al. Conditionally ablated Pten in prostate basal cells promotes basal-to-luminal differentiation and causes invasive prostate cancer in mice. *Am. J. Pathol.* **182**, 975–991 (2013).
5. Choi, N., Zhang, B., Zhang, L., Ittmann, M. & Xin, L. Adult murine prostate basal and luminal cells are self-sustained lineages that can both serve as targets for prostate cancer initiation. *Cancer Cell* **21**, 253–265 (2012).
6. Wang, Z. A. et al. Lineage analysis of basal epithelial cells reveals their unexpected plasticity and supports a cell-of-origin model for prostate cancer heterogeneity. *Nat. Cell Biol.* **15**, 274–283 (2013).
7. Kwon, O. J., Zhang, L., Ittmann, M. M. & Xin, L. Prostatic inflammation enhances basal-to-luminal differentiation and accelerates initiation of prostate cancer with a basal cell origin. *Proc. Natl Acad. Sci. USA* **111**, E592–E600 (2014).
8. Centonze, A. et al. Heterotypic cell–cell communication regulates glandular stem cell multipotency. *Nature* **584**, 608–613 (2020).
9. Karthaus, W. R. et al. Regenerative potential of prostate luminal cells revealed by single-cell analysis. *Science* **368**, 497–505 (2020).
10. Guo, W. et al. Single-cell transcriptomics identifies a distinct luminal progenitor cell type in distal prostate invagination tips. *Nat. Genet.* **52**, 908–918 (2020).

11. Crowley, L. et al. A single-cell atlas of the mouse and human prostate reveals heterogeneity and conservation of epithelial progenitors. *eLife* **9**, e59465 (2020).
12. Mevel, R. et al. RUNX1 marks a luminal castration-resistant lineage established at the onset of prostate development. *eLife* **9**, e60225 (2020).
13. Wang, X. et al. A luminal epithelial stem cell that is a cell of origin for prostate cancer. *Nature* **461**, 495–500 (2009).
14. Shen, M. M. & Abate-Shen, C. Molecular genetics of prostate cancer: new prospects for old challenges. *Genes Dev.* **24**, 1967–2000 (2010).
15. Wang, G., Zhao, D., Spring, D. J. & DePinho, R. A. Genetics and biology of prostate cancer. *Genes Dev.* **32**, 1105–1140 (2018).
16. Li, W. & Shen, M. M. Prostate cancer cell heterogeneity and plasticity: Insights from studies of genetically-engineered mouse models. *Semin. Cancer Biol.* **82**, 60–67 (2022).
17. Wang, S. et al. Prostate-specific deletion of the murine Pten tumor suppressor gene leads to metastatic prostate cancer. *Cancer Cell* **4**, 209–221 (2003).
18. Goldstein, A. S., Huang, J., Guo, C., Garraway, I. P. & Witte, O. N. Identification of a cell of origin for human prostate cancer. *Science* **329**, 568–571 (2010).
19. Stoyanova, T. et al. Prostate cancer originating in basal cells progresses to adenocarcinoma propagated by luminal-like cells. *Proc. Natl Acad. Sci. USA* **110**, 20111–20116 (2013).
20. Lawson, D. A. et al. Basal epithelial stem cells are efficient targets for prostate cancer initiation. *Proc. Natl Acad. Sci. USA* **107**, 2610–2615 (2010).
21. Wang, Z. A., Toivanen, R., Bergren, S. K., Chambon, P. & Shen, M. M. Luminal cells are favored as the cell of origin for prostate cancer. *Cell Rep.* **8**, 1339–1346 (2014).
22. Lukacs, R. U., Goldstein, A. S., Lawson, D. A., Cheng, D. & Witte, O. N. Isolation, cultivation and characterization of adult murine prostate stem cells. *Nat. Protoc.* **5**, 702–713 (2010).
23. Pearson, H. B. et al. Identification of Pik3ca mutation as a genetic driver of prostate cancer that cooperates with Pten loss to accelerate progression and castration-resistant growth. *Cancer Discov.* **8**, 764–779 (2018).
24. Chen, Z. et al. Crucial role of p53-dependent cellular senescence in suppression of Pten-deficient tumorigenesis. *Nature* **436**, 725–730 (2005).
25. Agarwal, S. et al. Identification of different classes of luminal progenitor cells within prostate tumors. *Cell Rep.* **13**, 2147–2158 (2015).
26. Martin, P. et al. Prostate epithelial Pten/TP53 loss leads to transformation of multipotential progenitors and epithelial to mesenchymal transition. *Am. J. Pathol.* **179**, 422–435 (2011).
27. Thorpe, L. M., Yuzugullu, H. & Zhao, J. J. PI3K in cancer: divergent roles of isoforms, modes of activation and therapeutic targeting. *Nat. Rev. Cancer* **15**, 7–24 (2015).
28. Carver, B. S. et al. Reciprocal feedback regulation of PI3K and androgen receptor signaling in PTEN-deficient prostate cancer. *Cancer Cell* **19**, 575–586 (2011).
29. Floc'h, N. et al. Dual targeting of the Akt/mTOR signaling pathway inhibits castration-resistant prostate cancer in a genetically engineered mouse model. *Cancer Res.* **72**, 4483–4493 (2012).
30. Lamming, D. W. Inhibition of the mechanistic target of rapamycin (mTOR)-rapamycin and beyond. *Cold Spring Harb. Perspect. Med.* **6**, a025924 (2016).
31. Henry, G. H. et al. A cellular anatomy of the normal adult human prostate and prostatic urethra. *Cell Rep.* **25**, 3530–3542. e5 (2018).
32. Joseph, D. B. et al. Urethral luminal epithelia are castration-insensitive cells of the proximal prostate. *Prostate* **80**, 872–884 (2020).
33. Baures, M. et al. Prostate luminal progenitor cells: from mouse to human, from health to disease. *Nat. Rev. Urol.* **19**, 201–218 (2022).
34. Baures, M. et al. Transcriptomic signature and growth factor regulation of castration-tolerant prostate luminal progenitor cells. *Cancers* **14**, 3775 (2022).
35. Chan, J. M. et al. Lineage plasticity in prostate cancer depends on JAK/STAT inflammatory signaling. *Science* **377**, 1180–1191 (2022).
36. Aibar, S. et al. SCENIC: single-cell regulatory network inference and clustering. *Nat. Methods* **14**, 1083–1086 (2017).
37. Li, F. et al. ERG orchestrates chromatin interactions to drive prostate cell fate reprogramming. *J. Clin. Invest.* **130**, 5924–5941 (2020).
38. Song, H. et al. Single-cell analysis of human primary prostate cancer reveals the heterogeneity of tumor-associated epithelial cell states. *Nat. Commun.* **13**, 141 (2022).
39. Tuong, Z. K. et al. Resolving the immune landscape of human prostate at a single-cell level in health and cancer. *Cell Rep.* **37**, 110132 (2021).
40. Hirz, T. et al. Dissecting the immune suppressive human prostate tumor microenvironment via integrated single-cell and spatial transcriptomic analyses. *Nat. Commun.* **14**, 663 (2023).
41. Wong, H. Y. et al. Single cell analysis of cribriform prostate cancer reveals cell intrinsic and tumor microenvironmental pathways of aggressive disease. *Nat. Commun.* **13**, 6036 (2022).
42. Mitchell, C. A. et al. Stromal niche inflammation mediated by IL-1 signalling is a targetable driver of haematopoietic ageing. *Nat. Cell Biol.* **25**, 30–41 (2023).
43. Tsujimura, A. et al. Proximal location of mouse prostate epithelial stem cells: a model of prostatic homeostasis. *J. Cell Biol.* **157**, 1257–1265 (2002).
44. Burger, P. E. et al. Sca-1 expression identifies stem cells in the proximal region of prostatic ducts with high capacity to reconstitute prostatic tissue. *Proc. Natl Acad. Sci. USA* **102**, 7180–7185 (2005).
45. Goldstein, A. S. et al. Trop2 identifies a subpopulation of murine and human prostate basal cells with stem cell characteristics. *Proc. Natl Acad. Sci. USA* **105**, 20882–20887 (2008).
46. Kwon, O.-J., Zhang, L. & Xin, L. Stem cell antigen-1 identifies a distinct androgen-independent murine prostatic luminal cell lineage with bipotent potential. *Stem Cells* **34**, 191–202 (2015).
47. Ali, A. et al. Prostate zones and cancer: lost in transition? *Nat. Rev. Urol.* **19**, 101–115 (2022).
48. McNeal, J. E., Redwine, E. A., Freiha, F. S. & Stamey, T. A. Zonal distribution of prostatic adenocarcinoma: correlation with histologic pattern and direction of spread. *Am. J. Surg. Pathol.* **12**, 897–906 (1988).
49. Lee, J. J. et al. Biologic differences between peripheral and transition zone prostate cancer. *Prostate* **75**, 183–190 (2015).
50. Berquin, I. M., Min, Y., Wu, R., Wu, H. & Chen, Y. Q. Expression signature of the mouse prostate. *J. Biol. Chem.* **280**, 36442–36451 (2005).
51. Garcia, A. J. et al. Pten null prostate epithelium promotes localized myeloid-derived suppressor cell expansion and immune suppression during tumor initiation and progression. *Mol. Cell. Biol.* **34**, 2017–2028 (2014).
52. Toso, A. et al. Enhancing chemotherapy efficacy in Pten-deficient prostate tumors by activating the senescence-associated antitumor immunity. *Cell Rep.* **9**, 75–89 (2014).
53. Di Mitri, D. et al. Tumour-infiltrating Gr-1^{+} myeloid cells antagonize senescence in cancer. *Nature* **515**, 134–137 (2014).
54. Calcinotto, A. et al. IL-23 secreted by myeloid cells drives castration-resistant prostate cancer. *Nature* **559**, 363–369 (2018).
55. Lopez-Bujanda, Z. A. et al. Castration-mediated IL-8 promotes myeloid infiltration and prostate cancer progression. *Nat. Cancer* **2**, 803–818 (2021).

56. Brina, D. et al. The Akt/mTOR and MNK/eIF4E pathways rewire the prostate cancer translatome to secrete HGF, SPP1 and BGN and recruit suppressive myeloid cells. *Nat. Cancer* **4**, 1102–1121 (2023).
57. Lu, X. et al. Effective combinatorial immunotherapy for castration-resistant prostate cancer. *Nature* **543**, 728–732 (2017).
58. Deng, S. et al. Ectopic JAK–STAT activation enables the transition to a stem-like and multilineage state conferring AR-targeted therapy resistance. *Nat. Cancer* **3**, 1071–1087 (2022).
59. Guo, W. et al. JAK/STAT signaling maintains an intermediate cell population during prostate basal cell fate determination. *Nat. Genet.* **56**, 2776–2789 (2024).
60. Pitzen, S. P. et al. Comparative transcriptomics reveals a mixed basal, club, and hillock epithelial cell identity in castration-resistant prostate cancer. *Proc. Natl Acad. Sci. USA* **122**, e2415308122 (2025).
61. Huang, F. W. et al. Club-like cells in proliferative inflammatory atrophy of the prostate. *J. Pathol.* **261**, 85–95 (2023).
62. Kiviaho, A. et al. Single cell and spatial transcriptomics highlight the interaction of club-like cells with immunosuppressive myeloid cells in prostate cancer. *Nat. Commun.* **15**, 9949 (2024).
63. Van Keymeulen, A. et al. Distinct stem cells contribute to mammary gland development and maintenance. *Nature* **479**, 189–193 (2011).
64. Tikoo, A. et al. Physiological levels of Pik3caH1047R mutation in the mouse mammary gland results in ductal hyperplasia and formation of ERα-positive tumors. *PLoS ONE* **7**, e36924 (2012).
65. Jonkers, J. et al. Synergistic tumor suppressor activity of BRCA2 and p53 in a conditional mouse model for breast cancer. *Nat. Genet.* **29**, 418–425 (2001).
66. Luedde, T. et al. IKK1 and IKK2 cooperate to maintain bile duct integrity in the liver. *Proc. Natl Acad. Sci. USA* **105**, 9733–9738 (2008).
67. Leow, C. C., Wang, X.-D. & Gao, W.-Q. Novel method of generating prostate-specific Cre–LoxP gene switching via intraductal delivery of adenovirus. *Prostate* **65**, 1–9 (2005).
68. DuPage, M., Dooley, A. L. & Jacks, T. Conditional mouse lung cancer models using adenoviral or lentiviral delivery of Cre recombinase. *Nat. Protoc.* **4**, 1064–1072 (2009).
69. Park, S. et al. Novel mouse models of bladder cancer identify a prognostic signature associated with risk of disease progression. *Cancer Res.* **81**, 5161–5175 (2021).
70. WHO Classification of Tumours Editorial Board. in *Urinary and Male Genital Tumours: WHO Classification of Tumours* 5th edn, Vol. 8, Ch. 4, 193–233 (International Agency for Research on Cancer, 2022).
71. Drost, J. et al. Organoid culture systems for prostate epithelial and cancer tissue. *Nat. Protoc.* **11**, 347–358 (2016).
72. Jiang, C. et al. Collagen signaling and matrix stiffness regulate multipotency in glandular epithelial stem cells in mice. *Nat. Commun.* **15**, 10482 (2024).
73. Bolger, A. M., Lohse, M. & Usadel, B. Trimmomatic: a flexible trimmer for Illumina sequence data. *Bioinformatics* **30**, 2114–2120 (2014).
74. Dobin, A. et al. STAR: ultrafast universal RNA-seq aligner. *Bioinformatics* **29**, 15–21 (2013).
75. Anders, S., Pyl, P. T. & Huber, W. HTSeq-a Python framework to work with high-throughput sequencing data. *Bioinformatics* **31**, 166–169 (2015).
76. Dennis, G. et al. DAVID: database for annotation, visualization, and integrated discovery. *Genome Biol.* **4**, R60 (2003).
77. Langmead, B. & Salzberg, S. L. Fast gapped-read alignment with Bowtie 2. *Nat. Methods* **9**, 357–359 (2012).
78. Li, H. et al. The Sequence Alignment/Map format and SAMtools. *Bioinformatics* **25**, 2078–2079 (2009).
79. Zhang, Y. et al. Model-based analysis of ChIP-seq (MACS). *Genome Biol.* **9**, R137 (2008).
80. McLean, C. Y. et al. GREAT improves functional interpretation of cis-regulatory regions. *Nat. Biotechnol.* **28**, 495–501 (2010).
81. Heinz, S. et al. Simple combinations of lineage-determining transcription factors prime cis-regulatory elements required for macrophage and B cell identities. *Mol. Cell* **38**, 576–589 (2010).
82. Quinlan, A. R. & Hall, I. M. BEDTools: a flexible suite of utilities for comparing genomic features. *Bioinformatics* **26**, 841–842 (2010).
83. Zheng, G. X. et al. Massively parallel digital transcriptional profiling of single cells. *Nat. Commun.* **8**, 14049 (2017).
84. Hao, Y. et al. Integrated analysis of multimodal single-cell data. *Cell* **184**, 3573–3587.e29 (2021).
85. Pearson, K. LIII. On lines and planes of closest fit to systems of points in space. *Lond. Edinb. Dubl. Phil. Mag. J. Sci.* **2**, 559–572 (1901).
86. McInnes, L., Healy, J., Saul, N. & Großberger, L. UMAP: Uniform Manifold Approximation and Projection. *J. Open Source Softw.* **3**, 861 (2018).
87. Haynes, W. in *Encyclopedia of Systems Biology* (eds Dubitzky, W. et al.) 78 (Springer, 2013).
88. Street, K. et al. Slingshot: cell lineage and pseudotime inference for single-cell transcriptomics. *BMC Genom.* **19**, 477 (2018).

Acknowledgements

We thank the ULB animal facility and ULB genomic core facility (F. Libert and A. Lefort) for help with sequencing, DIAPath–CMMI, supported by the Fonds Yvonne Boël and by the European Regional Development Fund and the Walloon region (S. Rorive and J. Allard), for helping with histology, and J.M. Vanderwinden and LiMif for helping with microscopy. We thank M. Pasparakis, University of Cologne for providing the $P65^{fl/fl}$ mice. C.J. is supported by a long-term EMBO Postdoctoral Fellowships (ALTF 982-2021) and Foundation Against Cancer (2023-041). Y.S. is supported by Télévie. C.B. is supported by the WEL Research Institute, FNRS, Télévie, Fond Erasme, Fondation Contre le Cancer, ULB Foundation, European Research Council, Fonds Yvonne Boël and the Foundation Baillet Latour. A.S. is supported by KULeuven (SymBioSys – C14/18/092) and the Fondation Contre le Cancer (2015-143). The funders had no role in study design, data collection and analysis, decision to publish or preparation of the manuscript.

Author contributions

C.J. and C.B. designed the experiments and performed data analysis. C.J. performed most of the experiments and data analysis. Y.S. and A.S. performed the bioinformatic analysis. S.R. performed prostate tumor scoring. I.S. provided human prostate cancer samples. J.A. performed the H&E staining on mouse prostate tumors and IHC staining on human prostate cancers. E.T. performed the experiments on bulk RNA-seq of *Pten* deletion at 5 weeks. Z.Z. provided technical help. C.J. and C.D. performed sorting experiments. C.B. wrote the manuscript. All authors read and approved of the final paper.

Competing interests

The authors declare no competing interests.

Additional information

Extended data is available for this paper at https://doi.org/10.1038/s43018-025-00994-3.

Supplementary information The online version contains supplementary material available at https://doi.org/10.1038/s43018-025-00994-3.

Correspondence and requests for materials should be addressed to Cédric Blanpain.

Peer review information *Nature Cancer* thanks the anonymous reviewers for their contribution to the peer review of this work.

https://doi.org/10.1038/s43018-025-00994-3

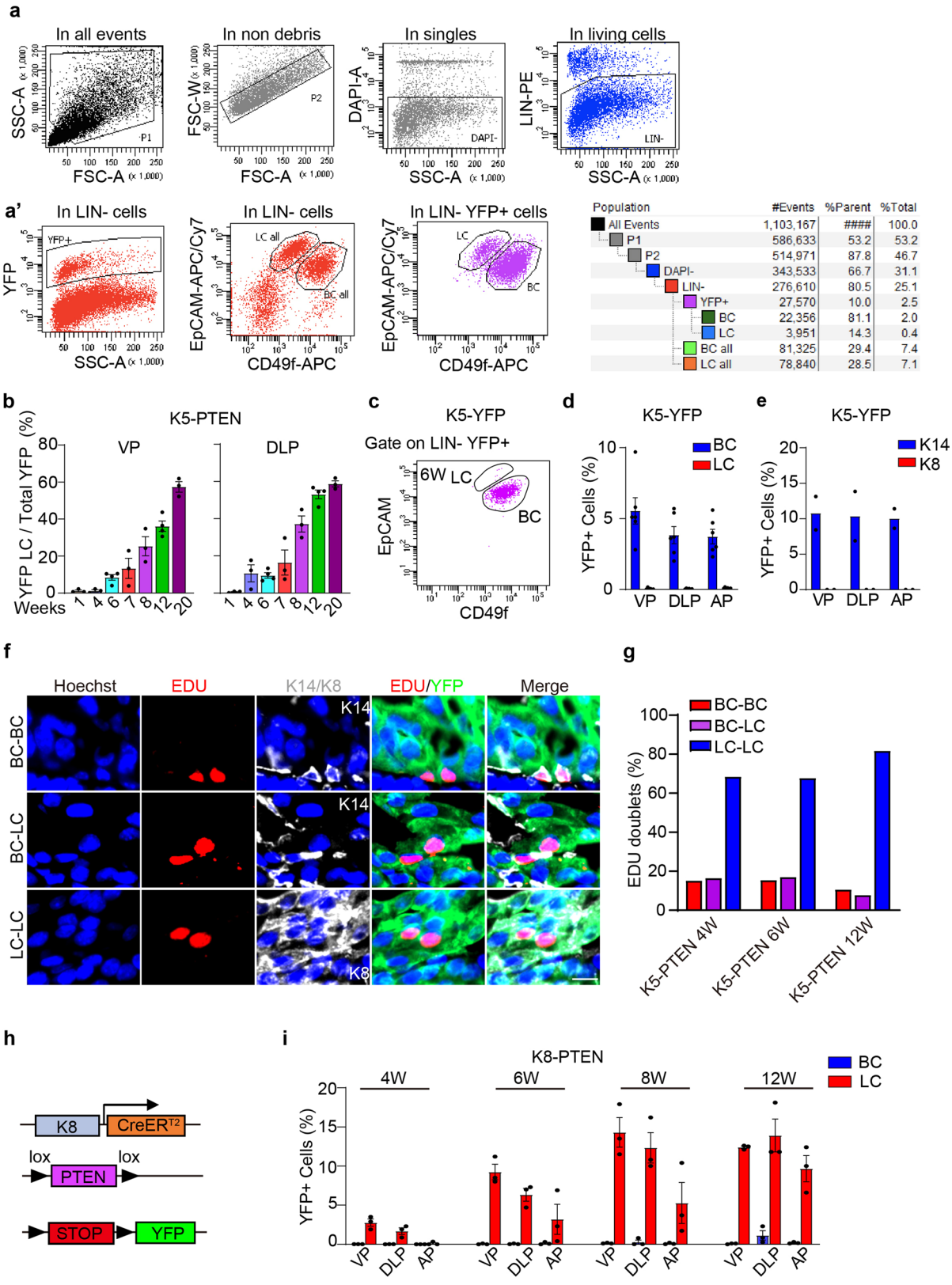

Extended Data Fig. 1 | See next page for caption.

https://doi.org/10.1038/s43018-025-00994-3

Extended Data Fig. 1 | Pten deletion induced BC plasticity and tumor initiation in a cell of origin and region-specific manners. (**a**) FACS gating strategy to analyze and isolate BCs and LCs from K5CreER/Pten$^{fl/fl}$/RosaYFP mice 6 weeks after TAM injection. Same strategy for all lineage tracing mice in this study. (**b**) Quantification of the % of Lin- YFP+ LCs in total YFP+ cells in VP and DLP at different time points after TAM injection in K5CreER/Pten$^{fl/fl}$/RosaYFP mice. n = 3 mice for 1w, 4w, 7w, 8w and 20w, n = 4 mice for 6w and 12w. (**c**) Representative FACS plot of CD49f and EpCAM expression in Lin- YFP+ prostate epithelial cells from K5CreER/RosaYFP mice 6 week after TAM administration. (**d**) Quantification of the % of Lin$^-$ YFP+ BCs and LCs in total BCs and LCs in VP, DLP and AP in in K5CreER/RosaYFP mice after 6-8 weeks TAM administration. n = 6 mice. (**e**) Quantification of the % of YFP + K14+ and YFP + K8+ in total K14+ and K8+ in VP, DLP and AP in K5CreER/RosaYFP mice after 4 weeks TAM administration. n = 2 mice. (**f**) Immunostainings of EdU (Red), GFP (Green), K14 (Grey) and K8 (Grey) in the prostate of K5CreER/Pten$^{fl/fl}$/RosaYFP at 4w, 6w and 12-week after TAM administration 24 h after EdU injection. Scale bar, 10 μm. n = 3 mice. (**g**) Quantification of percentage of EdU doublet following basal cell division giving rise BC-BC, BC-LC and LC-LC doublets. n = 152 EdU doublets (4w), n = 65 EdU doublets (6w) and n = 142 EdU (12w) doublets pooled from 3 mice. (**h**) Genetic strategy to lineage trace LC following *Pten* deletion (**i**) Quantification of Lin- YFP+ BCs and LCs in total BCs and LCs in VP, DLP and AP at different time points after TAM administration in K8CreER/Pten$^{fl/fl}$/RosaYFP mice. n = 3 mice. Graphs are mean ± s.e.m.

https://doi.org/10.1038/s43018-025-00994-3

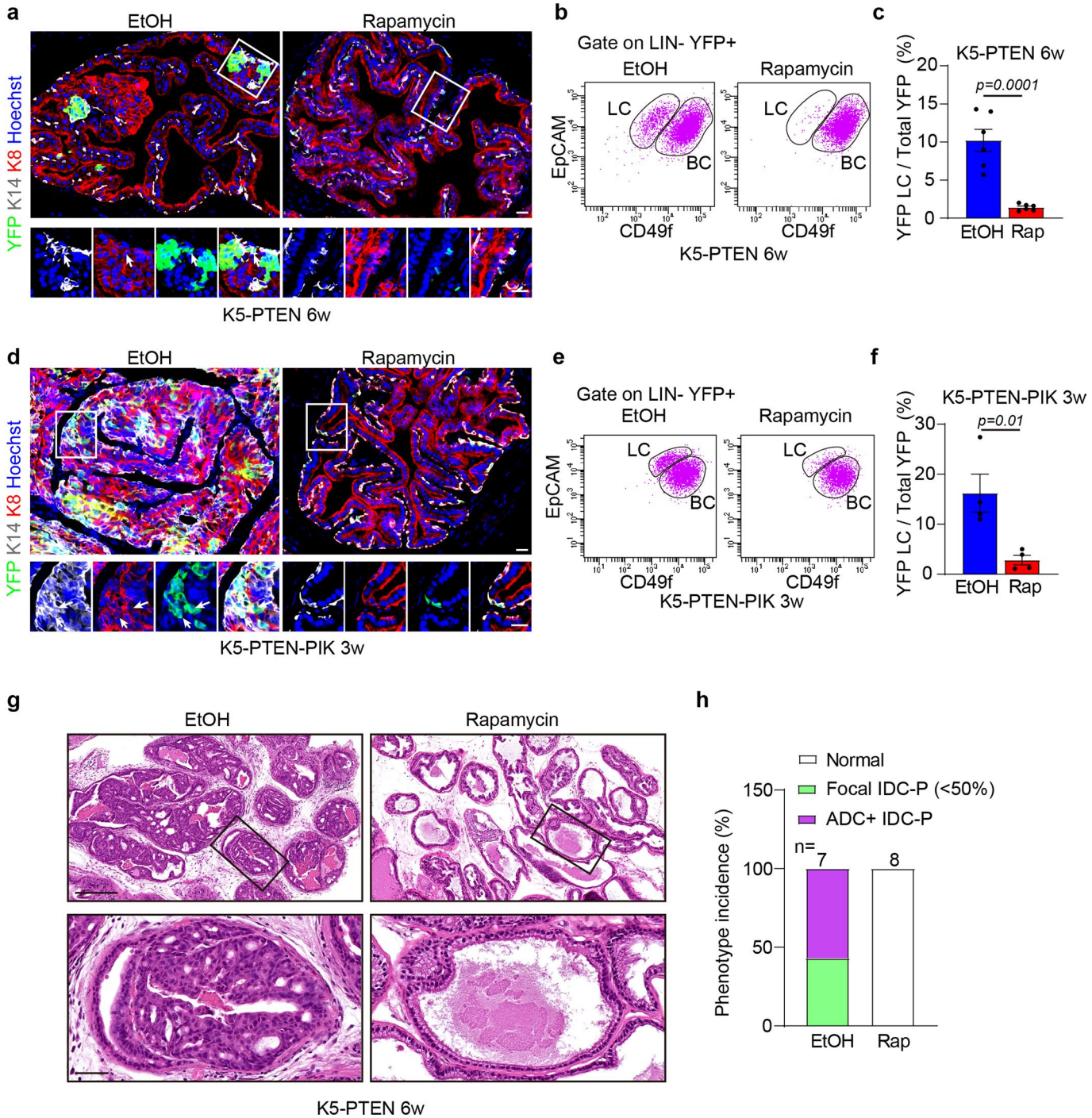

Extended Data Fig. 2 | mTOR inhibition blocks multipotency and tumor initiation. Representative immunostaining of the prostate from (**a**) K5CreER/Pten$^{fl/fl}$/RosaYFP mice 6 weeks after TAM administration (K5-PTEN 6w) and (**d**) K5CreER/Pten$^{fl/fl}$/Pik3ca^{H1047R}/RosaYFP mice 3 weeks after TAM administration (K5-PTEN-PIK 3w) treated with EtOH or Rapamycin (6 mg/kg, three injections per week) using anti-GFP (green), anti-K8 (red) and anti-K14 (grey) antibodies. Arrows indicate hybrid cells (YFP + K14 + K8 +). Scale bar, 20 µm (upper row), 10 µm (lower row). n = 3 mice. Representative FACS plot of CD49f and EpCAM expression in Lin- YFP+ prostate epithelial cells of (**b**) K5-PTEN 6w mice and (**e**) K5-PTEN-PIK 3w mice treated with EtOH or Rapamycin. Quantification of % of LIN- YFP+ LCs in total YFP+ cells in the whole prostate of (**c**) K5-PTEN 6w mice and (**f**) K5-PTEN-PIK 3w mice treated with EtOH or Rapamycin. n = 6 for K5-PTEN 6w mice, n = 4 for K5-PTEN-PIK 3w mice. (**g**) H&E-stained histological sections and (**h**) quantification of different types of tumorigenic lesions along prostate tumor progression in DLP of K5-PTEN 6w mice treated with EtOH (n = 7 mice) or Rapamycin (n = 8 mice). Scale bar, 250 µm (upper row), 50 µm (lower row). Graphs are mean ± s.e.m. p values are derived from two-sided unpaired t-test.

https://doi.org/10.1038/s43018-025-00994-3

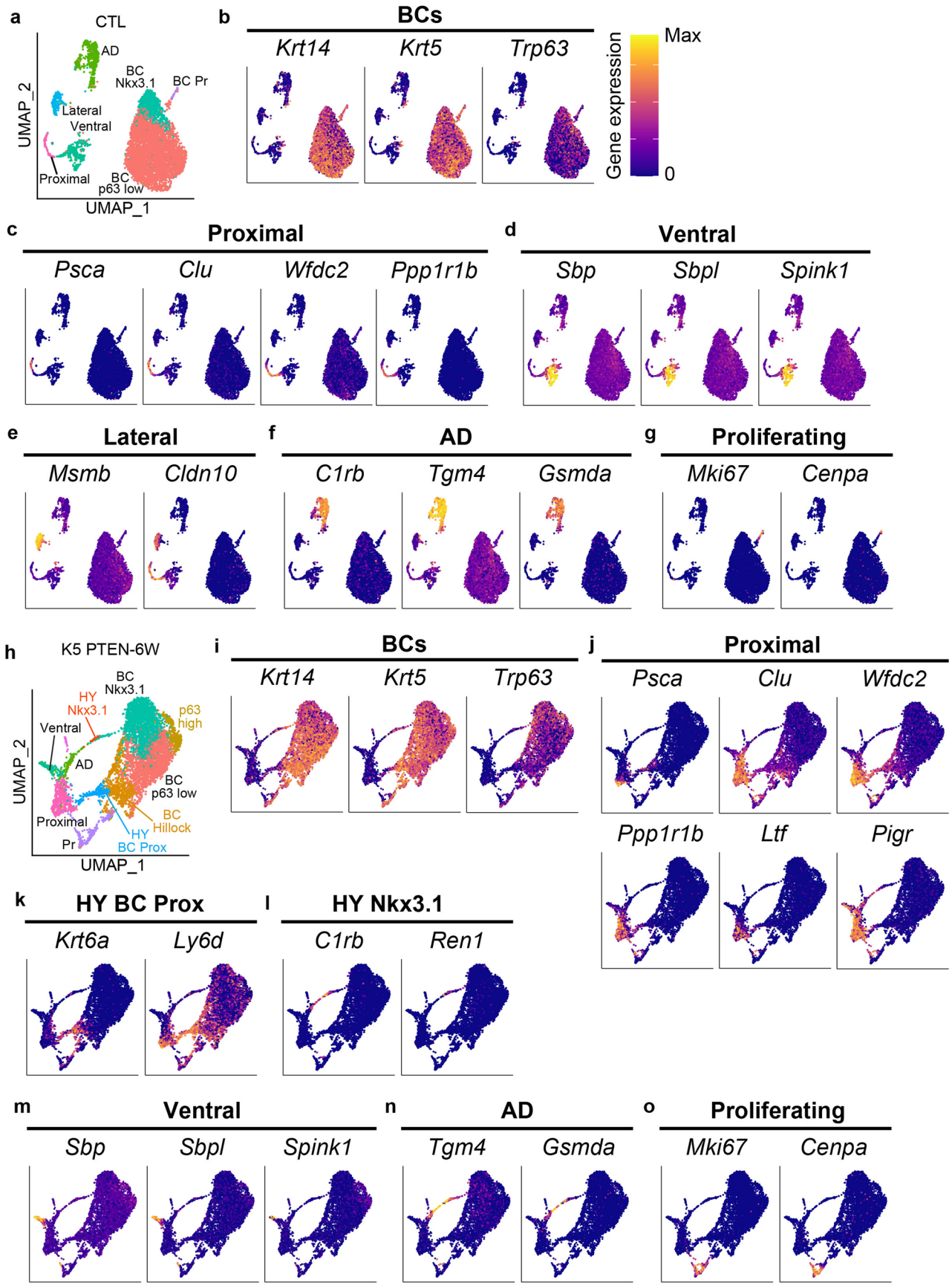

Extended Data Fig. 3 | See next page for caption.

https://doi.org/10.1038/s43018-025-00994-3

Extended Data Fig. 3 | Marker genes for each cell type in control and in K5-PTEN 6w prostate epithelial cells. Cell populations found by scRNA-seq in CTL prostate epithelial cells: **(a)** UMAP dimensionality reduction plots of CTL prostate epithelial cells with colors representing unsupervised clustering. **(b-g)** UMAP plots colored by normalized gene expression for (**b**) BC marker genes, (**c**) Proximal marker genes, (**d**) Ventral marker genes, (**e**) Lateral marker genes, (**f**) Antero-Dorsal marker genes and (**g**) Proliferative marker genes. **(h)** UMAP dimensionality reduction plots for K5-PTEN 6w using Seurat: UMAP dimensionality reduction plots with colors representing unsupervised clustering. **(i–o)** UMAP plots colored by normalized gene expression for (**i**) BC marker genes, (**j**) Proximal marker genes, (**k**) HY BC Prox marker genes, (**l**) HY Nkx3.1 marker genes, (**m**) Ventral marker genes, (**n**) Antero-Dorsal marker genes and (**o**) Proliferative marker genes.

https://doi.org/10.1038/s43018-025-00994-3

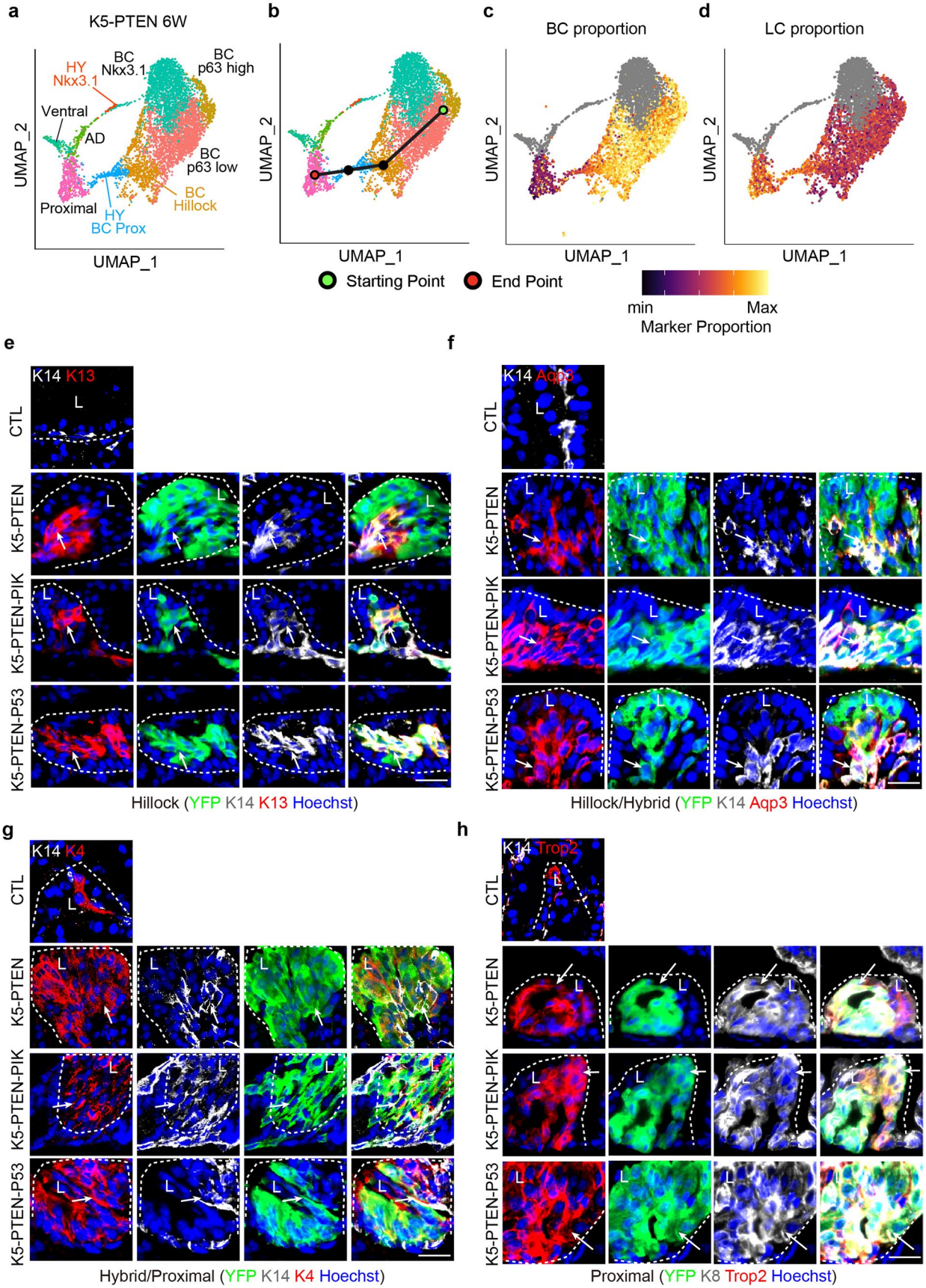

Extended Data Fig. 4 | See next page for caption.

https://doi.org/10.1038/s43018-025-00994-3

Extended Data Fig. 4 | Cellular trajectory and in situ characterization of Hillock, Hybrid and proximal-like LCs. (a) Cell populations of K5-PTEN 6w, which are used for trajectory inference: UMAP dimensionality reduction plots with different colors representing unsupervised clustering. **(b)** UMAP plot for the K5-PTEN 6w dataset showing the trajectory from BC to proximal LCs. **(c-d)** UMAP plot colored by the adjusted proportion of **(c)** BC-specific marker genes and **(d)** LC-specific marker genes. (**e-h**) Representative immunostaining of AP/DLP of CTL, K5CreER/Pten$^{fl/fl}$/RosaYFP mice 6 weeks after TAM administration, K5CreER/Pten$^{fl/fl}$/Pik3ca^{H1047R}/RosaYFP mice 3 weeks after TAM administration and K5CreER/Pten$^{fl/fl}$/P53$^{fl/fl}$/RosaYFP mice 4 weeks after TAM administration using (**e**) anti-K13, (**f**) anti-Aqp3, (**g**) anti-K4, (**h**) anti-Trop2 and anti-GFP (green), anti-K14 (grey) and anti-K8 (grey) antibodies. Arrows indicate Hillock cells, Hybrid cells and Proximal LCs as indicated markers. n = 3 mice. Dash lines marked the expanded LCs. L: prostate lumen. Scale bar, 20 μm.

https://doi.org/10.1038/s43018-025-00994-3

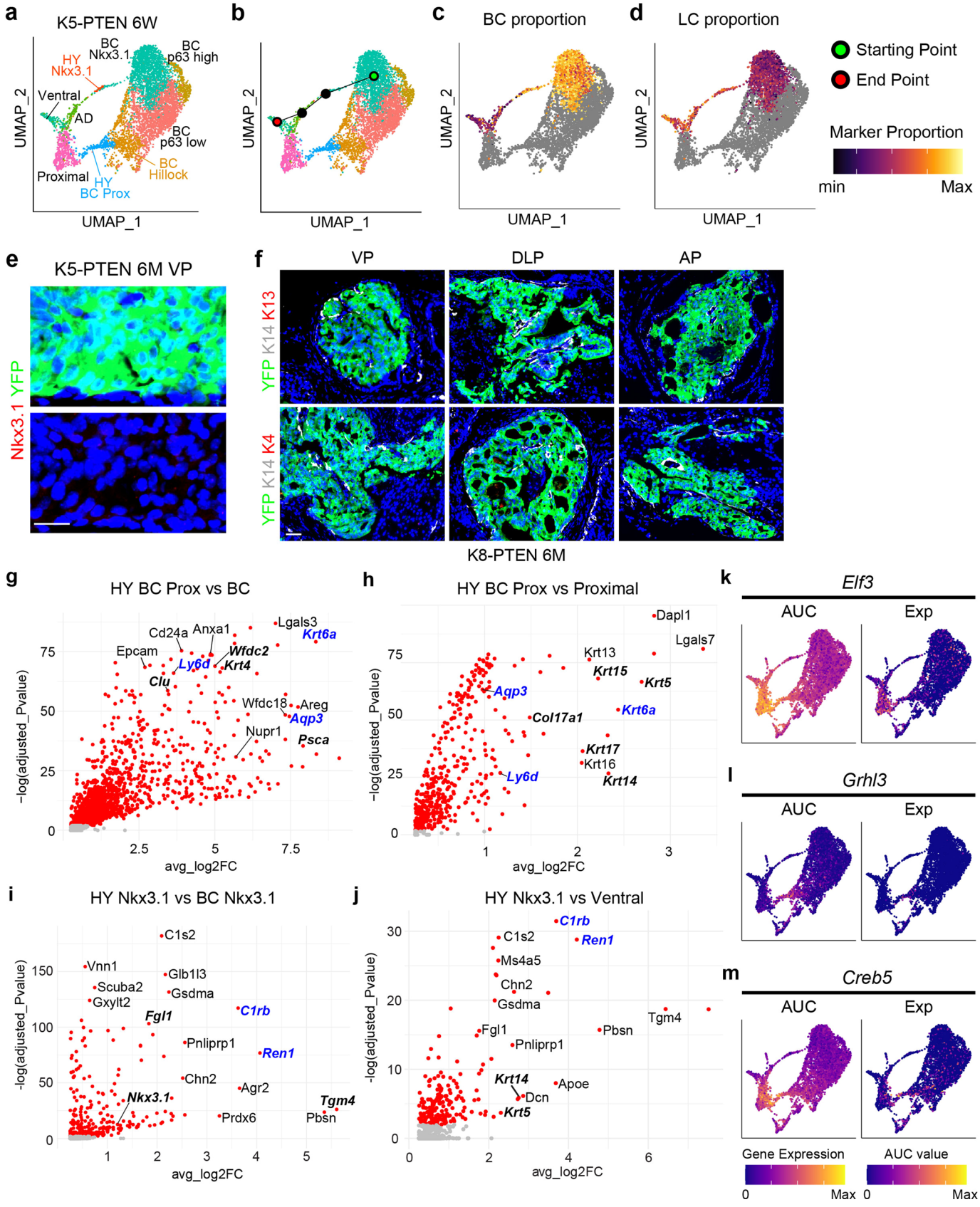

Extended Data Fig. 5 | See next page for caption.

https://doi.org/10.1038/s43018-025-00994-3

Extended Data Fig. 5 | scRNA-seq characterize hybrid basal–luminal cell states and lineage trajectory in K5-PTEN 6w prostate epithelial cells. (**a**) Cell populations of K5-PTEN 6w, which are used for trajectory inference: UMAP dimensionality reduction plots with different colors representing unsupervised clustering. **(b)** UMAP plot for the K5-PTEN 6w dataset showing the trajectory from BC to ventral LCs. **(c-d)** UMAP plot colored by the adjusted proportion of **(c)** BC-specific marker genes and **(d)** LC-specific marker genes. (**e**) Representative images of immunostaining of the VP of K5CreER/Pten$^{fl/fl}$/RosaYFP mice 6 months after TAM administration using anti-GFP (green), anti-Nkx3.1 (red). Scale bar, 50 µm. n = 3 mice. (**f**) Representative images of immunostaining of the VP, DLP and AP of K8CreER/Pten$^{fl/fl}$/RosaYFP mice 6 months after TAM administration using anti-GFP (green), anti-K13 (red), anti-K4 (red) and anti-K14 (grey) antibodies. Scale bar, 50 µm. n = 3 mice. **(g)** Genes significantly upregulated on HY BC Prox compared to BC p63 low and BC p63 high in K5-PTEN 6w scRNA dataset. **(h)** Genes significantly upregulated in HY BC Prox compared to proximal luminal cells. **(i)** Genes significantly upregulated on HY Nkx3.1 compared to the BC Nkx3.1. **(j)** Genes significantly upregulated in HY Nkx3.1 compared to the ventral prostate. **(k-m)** UMAP plots colored by (Left) SCENIC AUCs for regulon activation and (Right) normalized gene expression of the TF for **(k)** *Elf3*, **(l)** *Grhl3* and **(m)** *Creb5*. For **g** to **j**, red dots are significantly differentially expressed genes (FDR-adjusted *P* value < 0.01) and blue-labeled genes are uniquely expressed on hybrid population. P values were calculated using the Wilcoxon rank-sum test and adjusted using the Benjamini–Hochberg FDR method.

https://doi.org/10.1038/s43018-025-00994-3

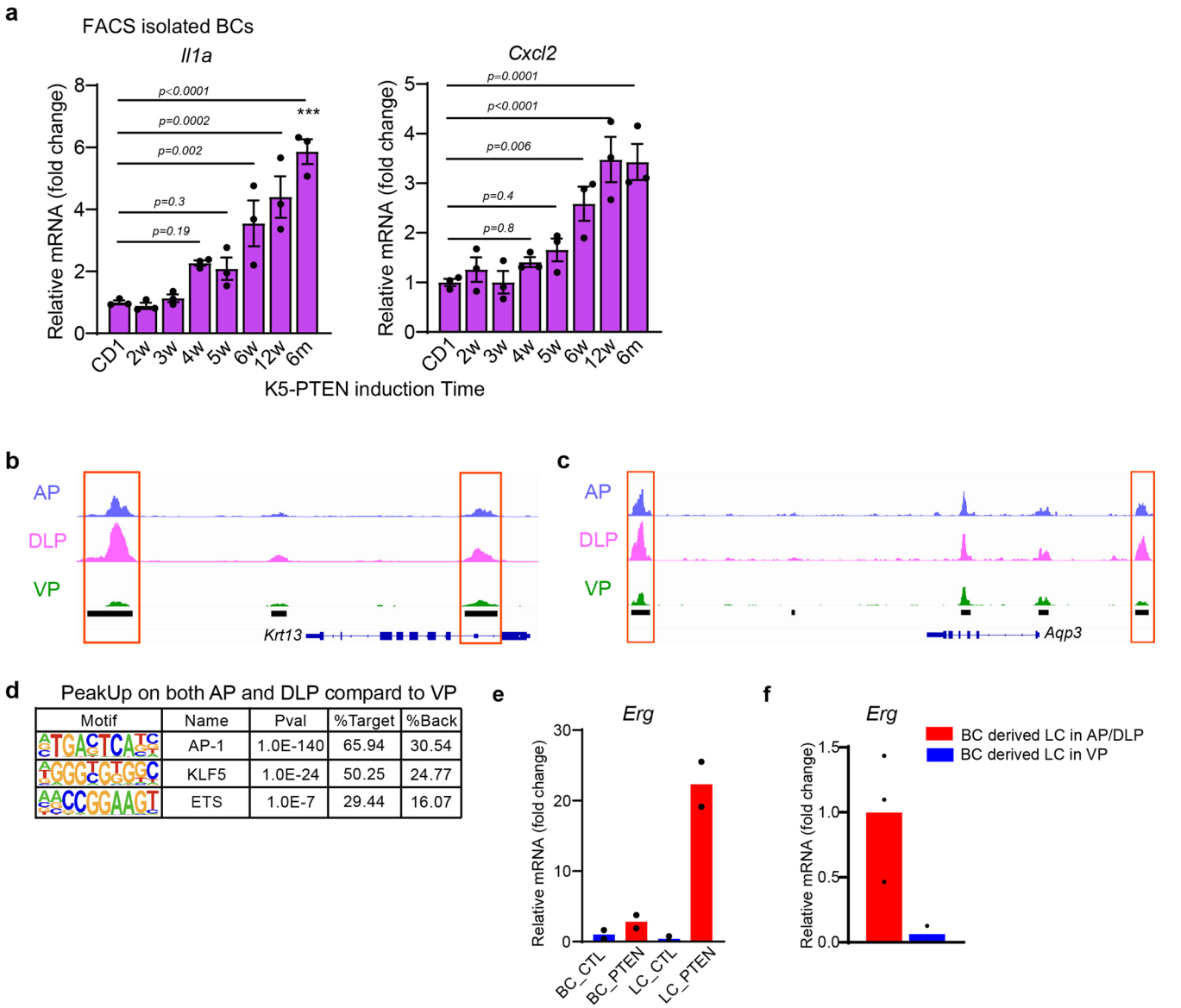

Motif	Name	Pval	%Target	%Back
	AP-1	1.0E-140	65.94	30.54
	KLF5	1.0E-24	50.25	24.77
	ETS	1.0E-7	29.44	16.07

Extended Data Fig. 6 | Temporal analysis of the activation of innate immunity and ATAC-seq and bulk RNA-seq on different lobes after Pten deletion in BC. (**a**) Relative mRNA expression levels of *Il1a* and *Cxcl2* were determined by quantitative RT–PCR in FACS-isolated BCs of AP/DLP from CD1 mice and YFP+ BCs from of K5CreER/Pten$^{fl/fl}$/RosaYFP mice at indicated time after TAM injection. mean ± s.e.m. n = 3 mice. p values are derived from one-way ANOVA with Dunnett test. ATAC-seq peaks of (**b**) *Krt13* and (**c**) *Aqp3* genes from FACS-isolated BCs of VP, DLP and AP of K5CreER/Pten$^{fl/fl}$/RosaYFP mice 6 weeks after TAM administration. Scale for visualization: 0-52 (*Krt13*) and 0-30 (*Aqp3*). Peaks which are upregulated at least 2-fold on AP and DLP compared to VP are highlighted with orange box. (**d**) TF motif enrichment analysis of peaks upregulated in BCs of AP/DLP compared to BCs of VP in K5-PTEN 6w. P values were calculated using a binomial test. (**e**) Relative *Erg* expression from bulk RNA-seq in FACS-isolated CTL BC, CTL LC from CTL mice and YFP+ BCs (BC_PTEN) and YFP+ LCs arising from *Pten* deleted BCs (LC_PTEN) from K5CreER/Pten$^{fl/fl}$/RosaYFP mice 5 weeks after TAM injection. n = 2. (**f**) Relative *Erg* expression from bulk RNA-seq of FACS-isolated LCs from AP/DLP versus VP in K5CreER/Pten$^{fl/fl}$/RosaYFP mice 6 months following TAM administration. (n = 3 for AP/DLP, n = 2 for VP).

https://doi.org/10.1038/s43018-025-00994-3

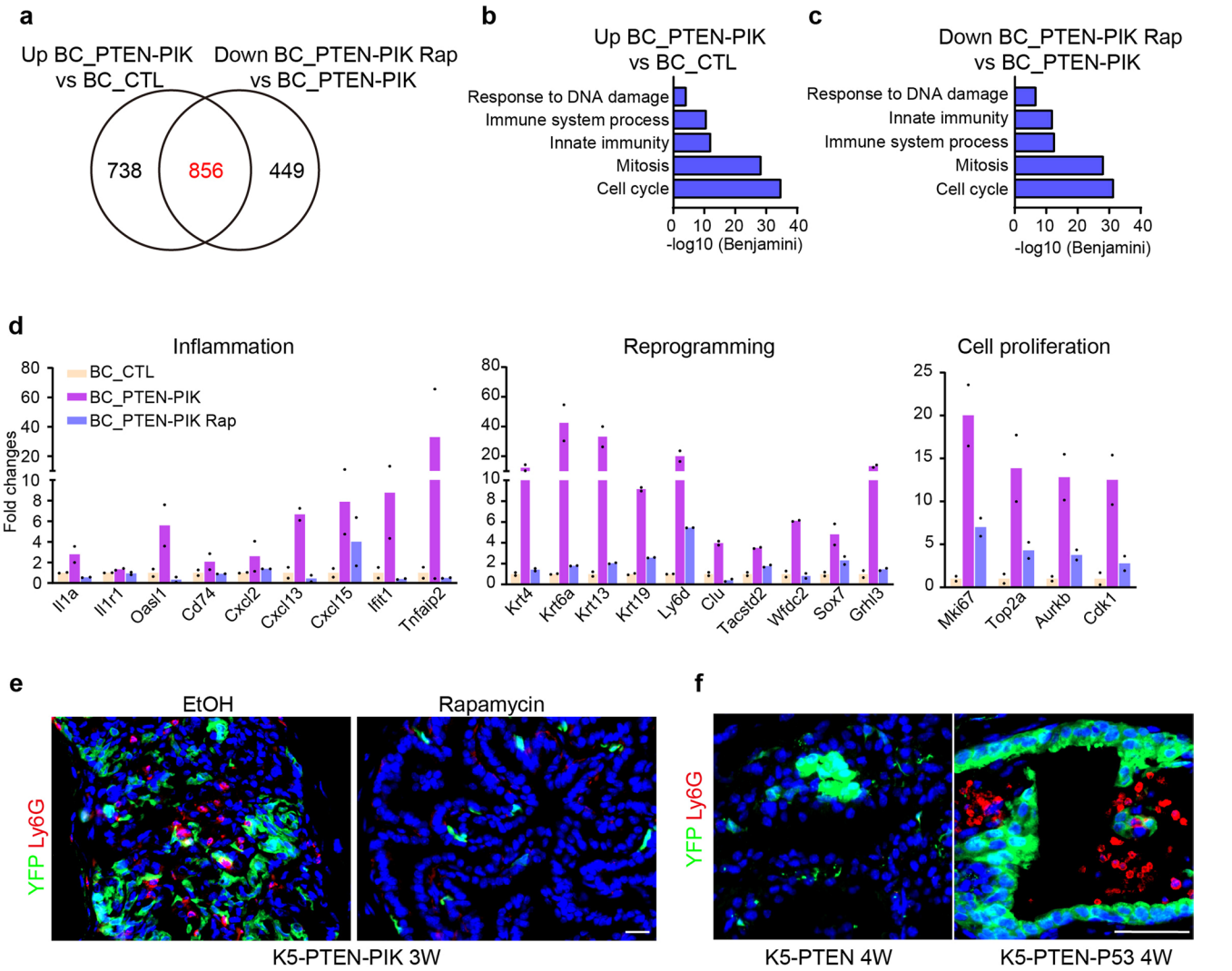

Extended Data Fig. 7 | Activation of innate immunity is a mTOR dependent. (**a**) Venn diagram illustrating the number of 2-fold upregulated genes in FACS-isolated LIN- YFP+ BCs of K5CreER/Pten$^{fl/fl}$/Pik3ca^{H1047R}/RosaYFP mice 3 weeks after TAM injection (vehicle treated, BC_PTEN-PIK) compared to FACS-isolated LIN- BCs of CD1 mice (vehicle treated, BC_CTL) and the number of 2-fold downregulated genes in FACS-isolated LIN- YFP+ BCs of K5CreER/Pten$^{fl/fl}$/Pik3ca^{H1047R}/RosaYFP mice 3 weeks after TAM injection treated with Rapamycin (BC_PTEN-PIK Rap) compared to BC_PTEN-PIK. (**b**) GO analysis of genes upregulated more than 2-fold in FACS-isolated BC_PTEN-PIK compared to FACS-isolated BC_CTL. (**c**) GO analysis of genes downregulated more than 2-fold in FACS-isolated BC_PTEN-PIK Rap compared to FACS-isolated BC_PTEN-PIK. (**d**) Expression of genes on bulk RNA-seq in FACS-isolated BC_CTL, BC_PTEN-PIK and BC_PTEN-PIK Rap. n = 2 samples. (**e**) Representative immunostaining of myeloid cells within AP from K5CreER/Pten$^{fl/fl}$/Pik3ca^{H1047R}/RosaYFP mice treated with EtOH or Rapamycin 3 weeks after TAM injection using anti-GFP (green), anti-Ly6G (red) antibodies. Scale bar, 20 µm. (**f**) Representative immunostaining of myeloid cells within the DLP from K5CreER/Pten$^{fl/fl}$/RosaYFP mice and K5CreER/Pten$^{fl/fl}$/P53$^{fl/fl}$/RosaYFP mice 4 weeks after TAM injection using anti-GFP (green), anti-Ly6G (red) antibodies. Scale bar, 50 µm. For **b** and **c**, P values were derived from two-tailed modified Fisher's Exact Test and adjusted using the Benjamini–Hochberg method.

https://doi.org/10.1038/s43018-025-00994-3

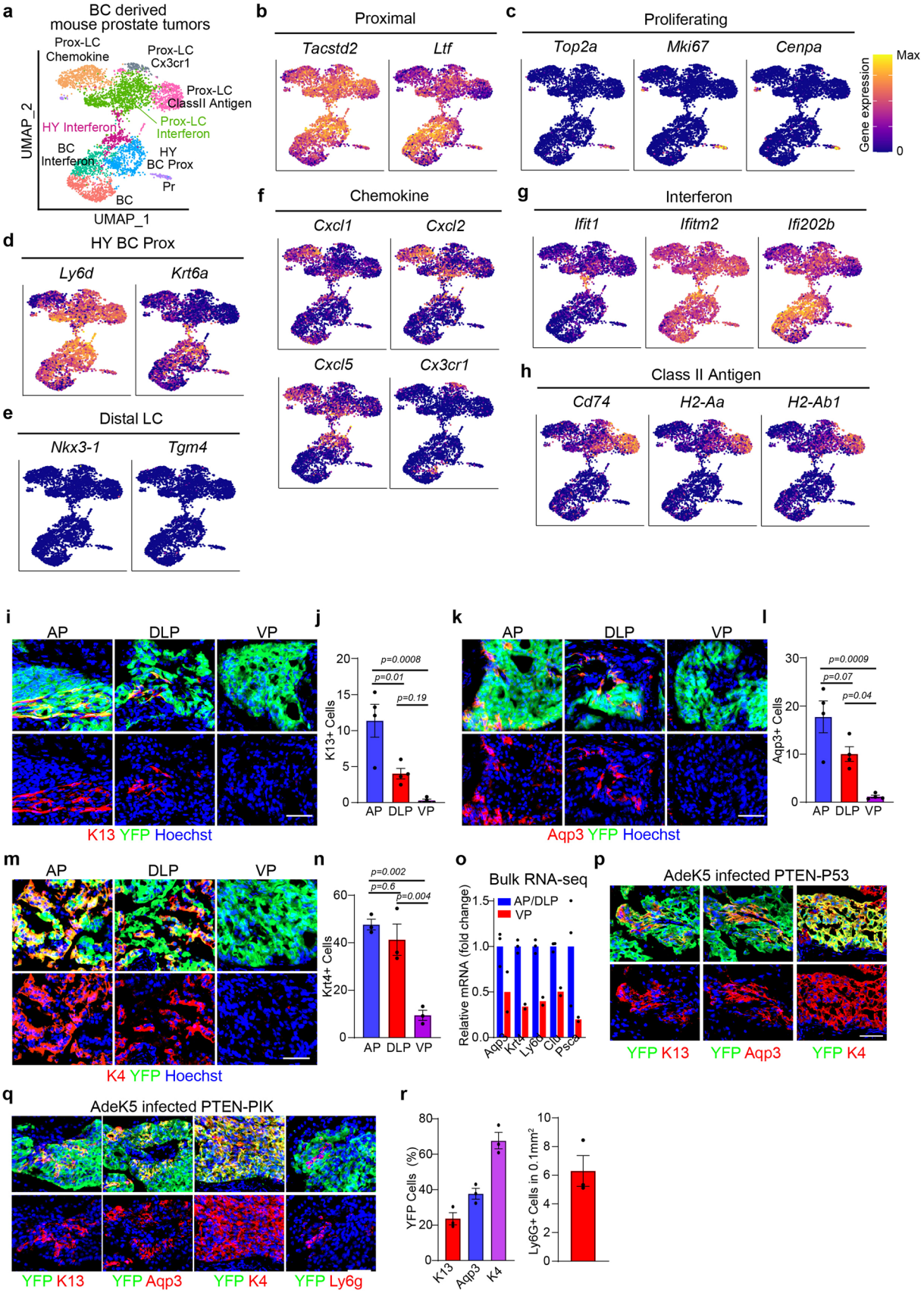

Extended Data Fig. 8 | See next page for caption.

https://doi.org/10.1038/s43018-025-00994-3

Extended Data Fig. 8 | Regional reprogramming and activation of innate immunity in BC-derived mouse prostate tumors. (a) UMAP dimensionality reduction plots with different colors representing unsupervised clustering of scRNA-seq of FACS-isolated LIN- YFP+ epithelial cells from K5CreER/Pten$^{fl/fl}$/RosaYFP mice 10 months after TAM administration: **(b-h)** UMAP plots colored by normalized gene expression for (**b**) Proximal marker genes, (**c**) Proliferative marker genes, (**d**) HY BC Prox marker genes, **(e)** Distal LC marker genes, **(f)** Chemokine marker genes, (**g**) Interferons marker genes, (**h**) MHC Class II antigens marker genes. (**i**–**n**) Representative immunostaining and quantification of (**i**, **j**) K13, (**k**, **l**) Aqp3 and (**m**, **n**) K4 in VP, DLP and AP of K5CreER/Pten$^{fl/fl}$/RosaYFP mice 6 months following TAM administration. Scale bar, 50 µm. n = 4 mice for K13 and Aqp3, n = 3 mice for K4. (**o**) Relative mRNA expression from bulk RNA-seq of the indicated genes in FACS-isolated YFP+ LCs from AP/DLP and VP in K5CreER/Pten$^{fl/fl}$/RosaYFP mice 6 months following TAM administration. (n = 3 for AP/DLP, n = 2 for VP). Representative immunostainings of AdeK5Cre infected AP of (**p**) Pten$^{fl/fl}$/P53/RosaYFP mice and (**q**) Pten$^{fl/fl}$/Pik3ca^{H1047R}/RosaYFP mice 2 months after virus injection using the indicated antibodies. Scale bar, 50 µm. (**r**) Quantification of the % of K13 + , Aqp3+ and K4+ in total YFP+ and Ly6G+ cells in AdeK5Cre injected AP of Pten$^{fl/fl}$/Pik3ca^{H1047R}/RosaYFP mice. n = 3 infections. Graphs are mean ± s.e.m. p values are derived from one-way ANOVA with Tukey's test.

https://doi.org/10.1038/s43018-025-00994-3

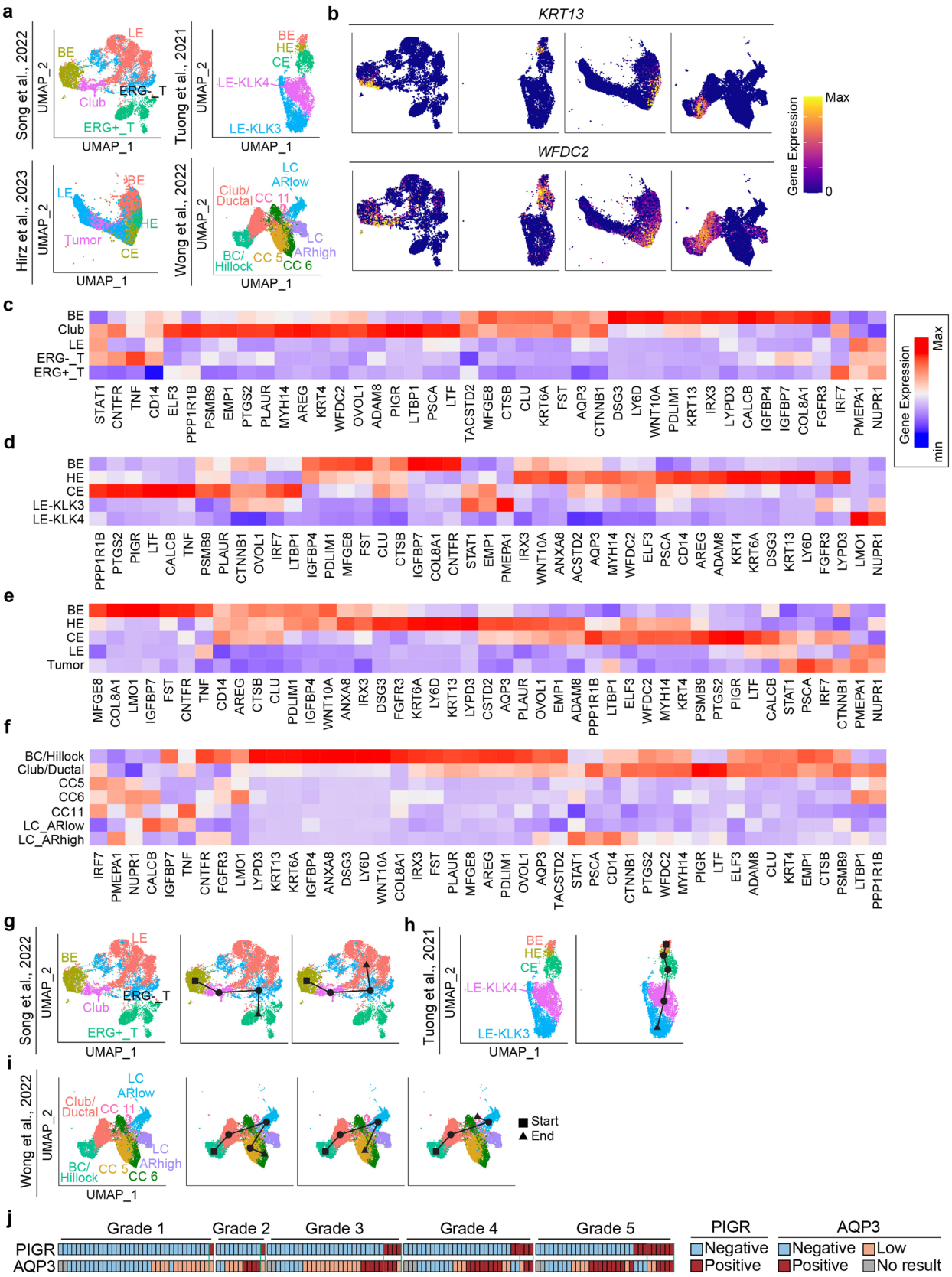

Extended Data Fig. 9 | See next page for caption.

https://doi.org/10.1038/s43018-025-00994-3

Extended Data Fig. 9 | Regional reprogramming in human prostate tumors. (**a**) Cell populations on ERG-driven human prostate cancer cells, human prostate cancer atlas, treatment-naïve prostate adenocarcinoma and invasive cribriform carcinoma and intraductal carcinoma data. **(b)** UMAP dimensionality reduction plots for *KRT13* and *WFDC2* with color scaling representing the level of gene expression. **(c-f)** Heatmap of reprogramming marker genes defined on K5-PTEN 6 W scRNA-seq data on **(c)** ERG-driven human prostate cancer cells, **(d)** human prostate cancer atlas, **(e)** treatment-naïve prostate adenocarcinoma and **(f)** invasive cribriform carcinoma and intraductal carcinoma data. **(g-i)** Slingshot pseudotime trajectory analysis illustrating the lineage trajectory on (**g**) ERG-driven human prostate cancer cells, (**h**) human prostate cancer atlas and (**i**) invasive cribriform carcinoma and intraductal carcinoma data. (**j**) Summary of IHC staining results for PIGR and AQP3 in prostate tumor samples from 136 patients, categorized by GG groups of prostate cancer. Green boxes indicate co-staining of PIGR and AQP3.

https://doi.org/10.1038/s43018-025-00994-3

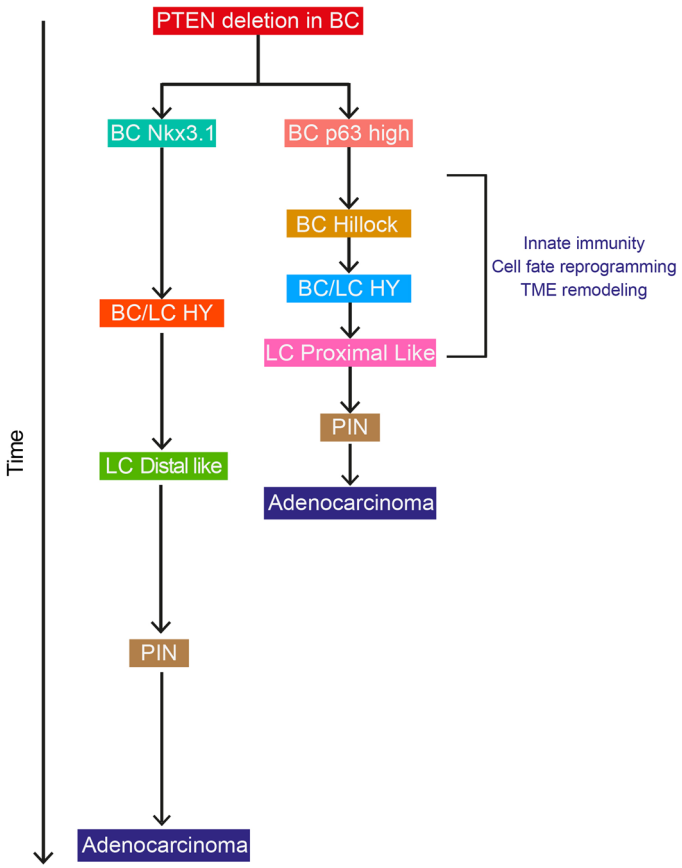

Extended Data Fig. 10 | Model of the early step of prostate tumor initiation. Cell plasticity, lineage infidelity and tumor progression following *Pten* deletion occurs in a region-specific manner during the early stage of prostate cancer initiation and are mediated by the activation of innate immunity in prostate basal stem cells.

nature portfolio

Corresponding author(s): Cédric Blanpain

Last updated by author(s): May 4, 2025

Reporting Summary

Nature Portfolio wishes to improve the reproducibility of the work that we publish. This form provides structure for consistency and transparency in reporting. For further information on Nature Portfolio policies, see our Editorial Policies and the Editorial Policy Checklist.

Statistics

For all statistical analyses, confirm that the following items are present in the figure legend, table legend, main text, or Methods section.

n/a	Confirmed
☐	☒ The exact sample size (*n*) for each experimental group/condition, given as a discrete number and unit of measurement
☐	☒ A statement on whether measurements were taken from distinct samples or whether the same sample was measured repeatedly
☐	☒ The statistical test(s) used AND whether they are one- or two-sided *Only common tests should be described solely by name; describe more complex techniques in the Methods section.*
☒	☐ A description of all covariates tested
☐	☒ A description of any assumptions or corrections, such as tests of normality and adjustment for multiple comparisons
☐	☒ A full description of the statistical parameters including central tendency (e.g. means) or other basic estimates (e.g. regression coefficient) AND variation (e.g. standard deviation) or associated estimates of uncertainty (e.g. confidence intervals)
☐	☒ For null hypothesis testing, the test statistic (e.g. *F*, *t*, *r*) with confidence intervals, effect sizes, degrees of freedom and *P* value noted *Give P values as exact values whenever suitable.*
☒	☐ For Bayesian analysis, information on the choice of priors and Markov chain Monte Carlo settings
☒	☐ For hierarchical and complex designs, identification of the appropriate level for tests and full reporting of outcomes
☒	☐ Estimates of effect sizes (e.g. Cohen's *d*, Pearson's *r*), indicating how they were calculated

Our web collection on statistics for biologists contains articles on many of the points above.

Software and code

Policy information about availability of computer code

Data collection	FACS ARIA III LSRFortessa Confocal (LSM 780) Axiovision realease 4.8 ZEISS Axioscan 7 Zen Blue 3.9 (ZEISS) Illumina Novaseq 6000 The codes used for data process, downstream analysis and plotting for this manuscript is available at https://github.com/yurasong/PTEN_codes.
Data analysis	For RNA sequencing, raw RNA-seq data quality was assessed using FastQC, and adaptor trimming was performed with TrimmomaticPE (v0.39). Reads were aligned to the mouse reference genome (GRCm38.87) using STAR (v2.7.5a), with annotations from Ensembl. Duplicate reads were removed using Picard (v2.1.1) MarkDuplicate module. Gene-level counts were generated with HTSeq (v0.11.1) and normalized to 20 million aligned reads per sample. Average gene expression was calculated per cell population using at least two biological replicates, and fold changes were computed between subpopulations. Differentially expressed genes were defined as those with ≥2-fold increase (upregulated) or ≤0.5-fold decrease (downregulated); genes with <10 counts in any sample were excluded. Gene Ontology (GO) enrichment of upregulated genes was assessed using DAVID (v2023q4), with significant categories defined by a Benjamini-adjusted p-value <0.01. For ATAC-seq, adaptor trimming was performed using TrimmomaticPE (v0.39) with parameters including HEADCROP:10, CROP:70, and SLIDINGWINDOW:4:15. Paired-end ATAC-seq reads were aligned to the mouse genome (GRCm38) using Bowtie2 (v2.2.6) with –very-sensitive, –no-discordant, and –no-mixed options. Reads mapping to mitochondrial DNA, random or unmapped contigs, or with MAPQ <20 were

removed using SAMtools. Duplicates were removed with Picard (v2.1.1) MarkDuplicate. Peaks were called on individual samples using MACS2 (v2.1.0.20151222) with -f BAMPE, --nomodel, --shift 0, and -q 0.01. Peaks across subpopulations were merged, and read counts per peak were quantified using HTSeq-count with normalization to one million reads. Peaks were linked to genes using GREAT (v4.0.4) with association parameters of 5 kb upstream, 1 kb downstream, and 100 kb distal. Peaks not associated with genes were excluded from further analysis. Differential peaks were defined by a ≥2-fold change over control and presence in the expanded condition. De novo motif analysis was performed with HOMER findMotifsGenome.pl tool, scanning ±250 bp from peak centers for 6–12 bp motifs. Background peaks were defined as non-differential peaks using BEDTools (v2.27.0) intersect.

For single-cell transcriptomics, sequencing reads were aligned to the mm10-2020-A reference genome (10X Genomics) and demultiplexed using CellRanger (v6.0.0). Quality control and analysis were performed in Seurat (v4.2.0), retaining cells with 2500 to 7500 genes and <15% mitochondrial UMIs. Data were normalized using LogNormalize with a scale factor of 10000. Dimensionality reduction (PCA, UMAP) and clustering used the top 2000 variable genes and the first 30 PCs. Non-epithelial clusters were excluded before re-clustering. Final annotation was based on marker genes reported in prostatic epithelium. Cluster marker genes were detected using the Wilcoxon rank-sum test and FDR correction; criteria included ≥25% expression, $\log_2$ fold change ≥0.25, and adjusted p-value <0.01. Hybrid and Hillock-specific genes were identified with FindMarkers() (logfc ≥0.25, min.pct ≥0.25). BC/LC markers (from wild-type) required log2 fold change >0.5, adjusted p-value <0.01, and ≥35% expression, with correction for sequencing depth. Gene regulatory networks were inferred using pySCENIC (v0.11.2), repeated 10 times per dataset, with differentially activated regulons defined by FDR-adjusted p <0.01. Lineage trajectories were inferred using Slingshot (v2.0.0), excluding proliferative/metabolic clusters, and confirmed across PCA and UMAP embeddings.

Processed human prostate cancer datasets were downloaded from: GitHub repository of the author (https://github.com/franklinhuanglab/scRNA-seq-Analysis-of-Prostate-Cancer-Samples, Song et al., Nat Commun, 2022), the Prostate Cell Atlas (https://www.prostatecellatlas.org, Tuong et al., Cell reports, 2021), and the GEO database linked to the publications (GSE181294, Hirz et al., Nat Commun, 2023; GSE185344, Wong et al., Nat Commun, 2022). Mouse-to-human orthologs for reprogramming genes were mapped using Ensembl BioMart, aligning the Grcm38.87 (mouse) and GRCh38 (human) reference genomes. Geneset enrichment analysis of reprogramming features on four human public datasets was performed using the AddModuleScore() embedded in Seurat R package, with default parameters. Module scores and marker gene expression were visualized with ggplot2 (v. 3.5.1) and viridis R package (version 0.6.5).

For Flow cytometry: FACS ARIA III (for FACS sorting), LSRFortessa (for FACS analysis) and FACSDiva software (v9.1) (for FACS data analysis).

Images were acquired at RT using a ZEISS Axioscan 7, a LSM780 confocal microscope fitted on an Axiovert M200 inverted microscope equipped with a C-Apochromat (40X, A.=1.2) water immersion objective and using a Zeiss Axio Imager M2 fluorescence microscope with a Zeiss Axiocam MR3 camera using Axiovision release 4.8 software. Brightness, contrast, picture size and analyses were performed using ZEN software and Adobe Photoshop CS6.

Statistical analyses based on biological replicates or independent experiments were performed using GraphPad Prism v.8.00, R (v.4.2.0) and Excel, with the methods and exact P values indicated in each figure and legend.

For manuscripts utilizing custom algorithms or software that are central to the research but not yet described in published literature, software must be made available to editors and reviewers. We strongly encourage code deposition in a community repository (e.g. GitHub). See the Nature Portfolio guidelines for submitting code & software for further information.

Data

Policy information about availability of data

All manuscripts must include a data availability statement. This statement should provide the following information, where applicable:

- Accession codes, unique identifiers, or web links for publicly available datasets
- A description of any restrictions on data availability
- For clinical datasets or third party data, please ensure that the statement adheres to our policy

All raw sequencing datasets that support the findings of this study have been deposited in the Gene Expression Omnibus (GEO) under accession number GSE270187 (scRNA-seq), GSE270189 (bulkRNA-seq, rapamycin treated), GSE270190 (bulkRNA-seq, cell fate upon PTEN deletion in BC), GSE286018 (bulkRNA-seq of P65/Pten knock BCs), GSE286019 (bulkRNA-seq of basal-derived and luminal-derived luminal tumors), GSE270191 (ATAC-seq of pooled BC/LC of WT and PTEN-deleted cells) and GSE288787 (ATAC-seq of BCs from different lobes upon PTEN deletion).

Previously published human prostate cancer datasets re-analysed in this study were available from GitHub repository of the author (https://github.com/franklinhuanglab/scRNA-seq-Analysis-of-Prostate-Cancer-Samples, Song et al., Nat Commun, 2022), the Prostate Cell Atlas (https://www.prostatecellatlas.org, Tuong et al., Cell reports, 2021) and GSE181294 (Hirz et al., Nat Commun, 2023), GSE185344 (Wong et al., Nat Commun, 2022).

The data that support the findings of this study are available from the corresponding author upon request. Source data are provided with this paper.

Data supporting the findings of this study are available within the article. All materials are readily available from the authors or from standard commercial sources. There are no restrictions on availability of the materials used in the study.

Research involving human participants, their data, or biological material

Policy information about studies with human participants or human data. See also policy information about sex, gender (identity/presentation), and sexual orientation and race, ethnicity and racism.

Reporting on sex and gender	N/A
Reporting on race, ethnicity, or other socially relevant groupings	N/A

Population characteristics	N/A
Recruitment	N/A
Ethics oversight	N/A

Note that full information on the approval of the study protocol must also be provided in the manuscript.

Field-specific reporting

Please select the one below that is the best fit for your research. If you are not sure, read the appropriate sections before making your selection.

☒ Life sciences ☐ Behavioural & social sciences ☐ Ecological, evolutionary & environmental sciences

For a reference copy of the document with all sections, see nature.com/documents/nr-reporting-summary-flat.pdf

Life sciences study design

All studies must disclose on these points even when the disclosure is negative.

Sample size	Samples size for each experiment is indicated in the figures or corresponding figure legends. The sample size was chosen based on previous experience in the lab (Jiang et al. Nature Comm 2024, Van Keymeulen et al Nature 2015 and Centonze et al Nature 2020). No statistical methods were used to predetermine sample size. All experiments were repeated at least three times with similar results, except for bulk RNAseq for which some experiments was repeated twice, and single-cell RNAseq, for which experiment was repeated one time, but each sequence we sorted and pooled the cells from at least three mice.
Data exclusions	Mice with low induction efficiency were excluded from the analysis and no other data were excluded.
Replication	All the experiments were performed in at least 3 biologically independent replicates (mice) or independent experiments. All replicates reported in the manuscript and on which statistics are based are these replicates. No technical replicates were used to calculate statistics. All attempts at replication of the results were successful.
Randomization	Only males are used in this study. The mice in this study were used according to their correct genotype. For the drug treatment, the mice are randomly divided into different treatment groups (littermate controls) at the same age and genotype.
Blinding	Data collection and analysis were not performed blind to the conditions of the experiments, as identification of the correct mouse genotype was necessary.

Reporting for specific materials, systems and methods

We require information from authors about some types of materials, experimental systems and methods used in many studies. Here, indicate whether each material, system or method listed is relevant to your study. If you are not sure if a list item applies to your research, read the appropriate section before selecting a response.

Materials & experimental systems

n/a	Involved in the study
☐	☒ Antibodies
☒	☐ Eukaryotic cell lines
☒	☐ Palaeontology and archaeology
☐	☒ Animals and other organisms
☒	☐ Clinical data
☒	☐ Dual use research of concern
☒	☐ Plants

Methods

n/a	Involved in the study
☒	☐ ChIP-seq
☐	☒ Flow cytometry
☒	☐ MRI-based neuroimaging

Antibodies

Antibodies used	For FACS, PE-conjugated anti-CD45 (1:100, clone 30-F11, BioLegend, 103106), PE-conjugated anti-CD31 (1:100, clone MEC 13.3, BioLegend, 102508), PE-conjugated anti-CD140a (1:100, clone APA5, Thermo, 12-1401-81), APC conjugated anti-CD49f (1:100, clone GoH3, eBiosciences, 17-0495), APC-Cy7-conjugated anti-EpCAM (1:100, clone G8.8, BioLegend, 118218). For IF staining, anti-K8 (rat, 1:500, Troma-I, Developmental Studies Hybridoma Bank, University of Iowa), anti-GFP (Goat, 1:500, abcam, cat. no. ab6673), anti-GFP (rabbit, 1:500, Invitrogen, cat. no. A11122), Rabbit or chicken anti-K14 (1:1000, Thermo, Custom Product), anti-Ly6G (Rat, 1:200, Biolegend, cat. no.127602). anti-Krt4 (Rabbit, 1:200, Proteintec, cat. no.16572-1-AP), anti-Krt13 (Rabbit, 1:200, Abcam, cat. no. ab92551), Anti-Aqp3 (Rabbit, 1:200, Abcam, cat. no. ab125219), anti-Col1a1 antibody (1:200, Cell Signaling Technology, cat. no.72026S), anti-CD45 antibody (Rat, 1:200, Biolegend, cat. no. 103106) and anti-Trop2 (Goat, 1:200, RD, cat. no. AF1122). The following secondary antibodies, Cy5-anti-chicken (1:400, JacksonImmunoResearch, 703-175-155), Cy5-anti-

Rabbit (1:400, JacksonImmunoResearch, 711-175-152), AlexaFluor 488-conjugated anti-goat (1:400; Invitrogen, cat. no. A-11055), AlexaFluor 488-conjugated anti-rabbit (1:400; Invitrogen, cat. no. A-21206), Rhodamine Red RRX-anti-rat (1:400, JacksonImmunoResearch, 712-296-153), Rhodamine Red RRX-anti-rabbit (1:400, JacksonImmunoResearch, 711-295-152), Rhodamine Red RRX-anti-goat (1:400, JacksonImmunoResearch, 705-295-003).

For WB, anti-phospho-p65 (Ser536, Rabbit, 1:1000, Cell Signaling, cat#3033), anti-p65 (Rabbit, 1:1000, Cell Signaling, cat#8242), anti-phospho-Stat1 (Ser727, Rabbit, 1:1000, Cell Signaling, cat#8826), anti-Stat1 (Rabbit, 1:1000, Cell Signaling, cat#9172), anti-phospho-Akt (Ser473, Rabbit, 1:1000, Cell Signaling, cat#4060), anti-Akt (Rabbit, 1:1000, Cell Signaling, cat#9272) and anti–β-actin (1:2000, Abcam, Cat#ab8227). Anti-rabbit IgG conjugated with horseradish peroxidase (HRP) (1:5000; Sigma Aldrich, Gena9340)

For immunohistochemistry on human, anti-PIGR (Rabbit, 1:100, Sigma, cat. no. HPA012012), anti-STAT1 (Rabbit, 1:400, Cell Signaling, cat. no. #14994S), Anti-AQP3 (Rabbit, 1:1000, Sigma, cat. No. HPA014924), EnVision+System-HRP labelled Polymer anti-rabbit Ig antibody (Agilent, cat. No. K400311-2).

Validation

Antibodies are available commercially. We used protocols and dilution recommandations of the manufacturer on validated species. Antibodies used in this study were previously described in Jiang et al. Nature Comm 2024, Van Keymeulen et al, Nature 2015 and Centonze et al, Nature 2020.

Animals and other research organisms

Policy information about studies involving animals; ARRIVE guidelines recommended for reporting animal research, and Sex and Gender in Research

Laboratory animals

All the animals used were grown in mixed background. The generation of K5CreER and K8-CreERT2 was previously described (Van Keymeulen et al, Nature 2011). Rosa26-YFP and Ptenfl/fl mice were obtained from the Jackson laboratory. Pik3caH1047R knock-in mice, in which wild-type exon 20 is replaced by H1047R mutant exon 20 upon Cre recombination. P53fl/fl mice were obtained from the National Cancer Institute at Frederick (Jonkers, J. et al 2021). P65fl/fl mice were imported from Dr. Manolis Pasparakis lab (Luedde, T. et al 2008). Male mice with a mixed genetic background were used in this study. All the experiments strictly complied with the protocols approved by ethical committee. Mice were induced and analyzed at adult age (over 8-weeks old), as indicated in the figure legends and methods.

Wild animals

No wild animals were used in this study.

Reporting on sex

Males have been used in this study.

Field-collected samples

No field collected sample were used in this study.

Ethics oversight

Mice colonies were housed in a certified animal facility in compliance with European guidelines. The room temperature was maintained between 20 and 24°C, with relative humidity kept at 55±10%. Food, water and two types of nesting material were provided in each cage. A semi-natural light 12-hour light/dark cycle was implemented. All animal experiments were approved by the ethical committee (Commission d'Ethique et du Bien Être Animal, CEBEA) of the Faculty of Medicine, Université Libre de Bruxelles under protocols #673N, #854N, #914N. CEBEA follows the European Convention for the Protection of Vertebrate Animals used for Experimental and other Scientific Purposes. As prostate tumors grow intra-abdominally, humane endpoints based on general health and a 20% body weight loss limit, approved by CEBEA, were not exceeded in this study. Male mice were used at adult age (over 8 weeks) for the prostate analysis.

Note that full information on the approval of the study protocol must also be provided in the manuscript.

Plants

Seed stocks

N/A

Novel plant genotypes

N/A

Authentication

N/A

Flow Cytometry

Plots

Confirm that:

☒ The axis labels state the marker and fluorochrome used (e.g. CD4-FITC).

☒ The axis scales are clearly visible. Include numbers along axes only for bottom left plot of group (a 'group' is an analysis of identical markers).

☒ All plots are contour plots with outliers or pseudocolor plots.

☒ A numerical value for number of cells or percentage (with statistics) is provided.

Methodology

Sample preparation	Prostate tissue including ventral, dorso-lateral and anterior prostate were isolated from indicated mouse lines at indicated time points after TAM injection. Tissues were minced in a 6-cm culture plate and digested in 5mg/ml collagenase type II (Life Technologies, cat. no. 17101-015) with 10 µM Y-27632 dihydrochloride (Abmole Bioscience, cat. no. M1817) for 1.5-2 h at 37°C on a shaking platform. Glandular structures were then washed with Advanced DMEM/F12 and centrifuged at 150g for 5 mins at 4°C. Structures were further digested in Trypsin for 10-20 min at 37°C and Trypsin activity was quenched using 2% FBS in PBS. Cells were passed through a 40µm cell strainer and incubated with fluorochrome-conjugated primary antibodies for 30 mins on ice with shaking every 10 min. Detailed antibody information was provided in supplementary tables. Cells were washed with 2% FBS/PBS and resuspended in DAPI or Hoechst before analysis. Data analysis and cell sorting were performed on a FACSAria sorter using the FACS DiVa software (BD Biosciences). Dead cells (DAPI+) and Lin+ (CD45+, CD31+ and CD140a+) cells were excluded before analysis. Due to technical challenges in obtaining enough BC-derived LCs from adult wild-type mice, we compared LCs isolated from adult CD1 mice with LCs arising from Pten-deleted BCs. The following populations were analyzed and sorted BCs: DAPI- LIN- YFP+ CD49fhigh EpCAM+ and LCs: DAPI- LIN- YFP+ CD49flow EpCAM+.
Instrument	FACSAria and LSRFortessa (BD Bioscience)
Software	FACSDiva and FACSAria Software (BD Bioscience)
Cell population abundance	The proportion of YFP+ PTEN deleted cells in Lin- population varied from 5% to 20%. This proportion varies depending on the different genetic mouse lines and induction deficiency.
Gating strategy	Living cells were selected by forward and side scatter, doublets discriminating and DAPI dye exclusion. CD45+, CD31+ and CD140a+ cells were excluded (Lin+) before analysis. For CD1 mice cell sorting, we sorted BC: DAPI- LIN- CD49fhigh Epcam+ , we sorted LC: DAPI-, LIN- CD49flow Epcam+. For above genetically lineage tracing mice, we analyzed and sorted BC: DAPI- LIN- YFP+ CD49fhigh Epcam+ and LC: DAPI- LIN- YFP+ CD49flow Epcam+.

☒ Tick this box to confirm that a figure exemplifying the gating strategy is provided in the Supplementary Information.